The Royal Institution of Great Britain
Davy-Faraday Research Laboratory

University College London
Department of Physics & Astronomy

University of London

Development and Application of Embedded Cluster Methodologies for Defects in Ionic Materials

Thesis submitted for the degree of Doctor of Philosophy

by

Petr Valentinovich Sushko

2000

Abstract

The main objectives of the present Thesis were to develop a method and computer code for calculating the properties of point defects in insulators, and to study defects and the mechanisms of defect processes in the bulk and at surfaces of ionic crystals.

We develop an embedded cluster method and a computer code, which allows us to treat a defect in a crystal quantum mechanically in the effective potential of the rest of the polarisable crystal. This method has several advantages with respect to existing methods: i) it can be applied to bulk and surface defects; ii) it allows application of several quantum-mechanical methods, including the Hartree-Fock method and different configuration interaction techniques, and methods based on the Density Functional Theory; iii) it allows one to calculate the spectroscopic properties of point defects, such as optical absorption, vibrational spectra and hyperfine interactions, taking into account the defect interaction with the rest of the crystal; iv) the atomic structure of the defect can be optimised self-consistently using an effective procedure. The new method and the computer code have been tested on a number of well-established systems.

The method has been applied to study the electronic structure and properties of several defects, and to model the mechanisms of various surface processes. i) We have calculated the position of the top of the (001) MgO surface valence band with respect to the vacuum level and the energy levels of neutral and charged oxygen vacancies with respect to the top of the valence band and the vacuum level. ii) The study of the electronic structure of excitons at low coordinated oxygen sites of the MgO surface has demonstrated a significant dependence of the excitation energies on oxygen coordination. iii) A variety of geometric configurations of the $[FeCl_n(CN)_{6-n}]^{3-}$ and $[FeCl_n(CN)_{6-n}]^{4-}$ impurities in the bulk of NaCl were studied and the most stable configurations identified. iv) It was demonstrated that the accurate account of lattice polarisation is crucial for quantitative agreement of the optical absorption and luminescence energies with the experimentally observed properties of the Ce^{3+} centres in $LiBaF_3$. v) Modelling of the interaction of a silicon tip with the NaCl (001) surface has demonstrated that the tip-surface interaction can lead to transfer of surface ions to the tip and allowed us to establish the charge state of the transferred Cl ions. vi) The analysis of the mechanism of laser-induced desorption of positive Mg ions from the (001) MgO surface allowed us to elucidate the atomistic stages of the desorption process. The results of this Thesis have demonstrated the applicability of the method developed to a wide range of defect properties in ionic materials.

Contents

List of Figures

List of Tables

Acknowledgements

It is a genuine pleasure to thank the following:

My supervisors Dr. A. L. Shluger and Prof. C. R. A. Catlow for their invaluable help, support, encouragement, and patience.

This work has been financially supported by Eastman Kodak. I would like to thank R. C. Baetzold, R. S. Eachus, and R. Curtis for their hospitality at the Eastman Kodak Research Labs as well as for many fruitful and stimulating discussions.

During last three years I have gained a lot from the discussions, arguments and critics of my colleagues and friends F. Corà, J. L. Gavartin, L. N. Kantorovich, M. Marsman, M. Nygren, A. A. Sokol.

My special thanks to M. Alfredsson, F. Corà, A. S. Foster, L. N. Kantorovich, M. Knott, and A. A. Sokol who have read parts of this Thesis and whose comments were very appreciated.

My colleagues and friends at the Royal Institution, University College London, and St.Petersburg University who have always been ready to answer my queries without loosing their temper. In particular I would like to thank I. A. Abarenkov, R. Bell, A. J. Fisher, J. D. Gale, J. H. Harding, A. H. Harker, A. I. Livshits, O. Pribyl, B. Slater, A. M. Stoneham, I. I. Tupitsyn, and many others from whom I have learned and benefited.

My wife and son for their understanding and tolerance.

> There is something fascinating about science. One gets such wholesale returns of conjecture out of such a trifling investment of fact.
>
> Mark Twain. *Life on the Mississippi.*

> To err is human but to really foul things up requires a computer.
>
> Anonymous.

Introduction

It has long been recognised that the understanding of crystal properties requires the study and atomistic modelling of crystal defects and defect processes. Characterisation of neutral and charged defect species in the bulk and at surfaces of solids requires a quantitative description of the defect local atomic structure, their optical and vibrational properties and their ability to trap electrons, holes and bond other species. Modelling of defect processes involves the description of diffusion of defect species in the bulk or at surfaces, adsorption and dissociation of molecules at surfaces or desorption of the surface material. To our opinion, in spite of a great deal of previous research, there is still no reliable computational method which would allow one to achieve these goals. Therefore, the main objectives of the present Thesis are to develop a method and computer code for calculations of properties of point defects in insulators, and to test its applicability and accuracy on a number of defects and defect processes in the bulk and at surfaces of ionic crystals.

Methods available. There are two major groups of methods available for defect calculations. The first group is based on a periodic model, in which the defect is periodically repeated. The second group of methods treats a single defect embedded in the crystal and accounts for the presence of the rest of the crystal.

A number of computer codes are implementing both *periodic* and *embedded cluster* approaches. Computer codes for periodic calculations at the DFT level using plane-waves (CASTEP, CETEP, VASP) or DFT and HF levels using localised basis sets (CRYSTAL98) are long available. The two most widely used codes designed for embedded cluster calculations are the EMBED code implementing a "perturbed-cluster" approach and the ICECAP code combining quantum mechanical treatment of a cluster with a classical treatment of its environment. Computer codes like Gaussian98, GAMESS, etc., which were developed for calculations of molecules, may be also used for embedded cluster calculations. In this case, however, the host lattice is unpolarisable.

Why not simply use these methods? This question is discussed in detail below. Briefly, most of the existing methods have severe limitations either in terms of their efficiency or in terms of their applicability to different defect properties. In particular, most of them cannot sufficiently accurately treat the lattice polarisation by point defects which is necessary to study electronic levels and excited states in real crystals. Although we are still far from creating a universal technique, useful progress can be made for certain types of crystals and defect states, such as point defects in insulators or semiconductors.

Aims of this Thesis. The aim of the present work is to develop a methodology which would enable us to *predict* models of defects and mechanisms of defect processes in insulators. We are aiming to develop a method and a computer code for embedded cluster calculations of point defects in the bulk and at surfaces of ionic crystals. The main features we want to achieve include:

- Flexibility with respect to quantum mechanical methods.
- Effectiveness with respect to geometry optimisation and calculation speed.
- Calculation of charged defects.
- Calculation of spectroscopic defect properties.
- Calculation of both bulk and surface defects.

We will need to validate the method and to find the range of its applicability. For this purpose we are aiming to apply the method to several systems and obtain new results. The range of problems and particular systems considered are outlined in the next paragraph.

Plan of the Thesis. This Thesis falls into two parts. The first part, which includes Chapters 1 and 2, is concerned with different embedded cluster approaches to studies of defects in ionic compounds. In Chapter 1 we describe which properties of defects are important for their characterisation, which models may be used to study these properties, and discuss several levels of complexity of embedded cluster calculations. At the end of Chapter 1 we outline the Group Function approach for weakly interacting molecules as developed by McWeeny and its application for the embedded cluster studies of point defects in ionic crystals. At the beginning of Chapter 2 we describe which mathematical simplification of the Group Function formalism may be done and how they correspond to physical approximation. In the rest of this Chapter we describe the details of the method and its computer implementation and tests which were performed for their validation. The applications of the method and the computer code to studies of defects and processes involving defects are described in Chapters 3, 4, and 5. Three types of problems were considered. In Chapter 3 we apply the method to a traditional area of solid state modelling: study of point defects in the bulk of ionic crystals. We consider the structure and properties of iron the cyanide complexes in NaCl and Ce^{3+} impurity defects in $LiBaF_3$ crystal. In Chapter 4 the method is applied to study the electronic properties of low-coordinated sites at the MgO (001) surface and neutral and charged oxygen vacancies associated with these sites. In Chapter 5 we demonstrate that our method can be used to model the mechanisms of processes at interfaces and photo-induced reactions. In particular, we consider: i) the interaction of an Atomic Force Microscope tip with the NaCl (001) surface, and ii) the mechanism of photo-induced desorption of positive ions from the defective MgO (001) surface. The Summary contains final remarks regarding the method and the code and a summary of our results.

1 Embedded Cluster approach to ionic solids

The tremendous increase of interest in the chemistry and physics of solids and their surfaces is connected with recent progress in advanced technologies, such as micro- and opto-electronics, selective catalysts and sensors, to mention a few. It has become clear that numerous important phenomena are caused by deviations from the infinite periodic structure of ideal solids due to doping and structural defects, formation of dislocations, metal-semiconductor or metal-insulator interfaces, amorphisation and formation of alloys. Complex systems can exhibit properties such as size quantisation and electronic Coulomb blockade which are of importance for nano-technology and micro-electronics. This Thesis is concerned with properties of defects in the bulk and at surfaces of ionic crystals. In section 1.1 of this Chapter we describe typical problems which are of interest to the physics of insulators and the existing theoretical models and methods that aim to deal with these problems. In section 1.2 we concentrate on a particular type of methodology known as *embedded molecular cluster methods* and outline its ideas and the evolution of approximations used over the last decades. We also outline the factors, which stimulated the development of the methodology described in the following Chapters. In section 1.3 the ideas of a more rigorous approach to the embedding problem based on the group function theory are discussed, which is followed by a description of the approximations which lead to a simpler but consistent model of a point defect in an ionic crystal.

1.1 General Introduction

1.1.1 Properties of point defects: Typical problems

Traditionally interesting problems concerning the physics of insulators are associated with point defects incorporated in the bulk of crystals. However, recent advances in experimental techniques, have made it possible to detect and study defects at surfaces and other low-coordinated sites. A range of problems include defect characterisation via an understanding of their properties and their role in processes involving interactions with photons, lattice vibrations, electrons and holes, magnetic field etc. Common examples include formation of localised excitons, other (self)-trapped quasi-particles in solids and quenching of optical luminescence via non-radiative processes. Surface defects can be characterised by their specific reactivity, i.e. ability to interact with atoms and molecules with the formation of new molecules, which involves bond-breaking and bond-making. Most of these processes can be understood and characterised in terms of those properties of defects which are outlined below.

Local atomic structure. The defect structure varies from relatively simple, as in the case of cation and anion vacancies or interstitials in alkali halides, to more complex as in the case of the F centre associated with a substitutional molecular ion, e.g. OH^-. In the latter case, a population of possible relative arrangements of the pair of defects depends on the relative and absolute concentrations of defects and temperature, which, it turn, significantly affects other properties of the crystal.

Electronic properties. The electronic structure of an atom or ion incorporated into crystalline lattice may be significantly influenced by the crystal field. The latter splits the energy levels which were degenerate in the case of free species, affecting optical absorption spectra. The ability of the defect to trap or donate electrons to other defects is of both fundamental and technological interest. For example, shallow electron trapping centres in AgCl are of particular importance for the photo-processing industry [74]. The positions of energy levels of defect states with respect to the valence and conduction bands determine the contribution of these states to the processes of electronic and hole conductivity and recombination.

Optical properties. Understanding of optical absorption and luminescence associated with point defects is important not only for their characterisation but also in search for new scintillation materials and for applications in optical devices. These properties are usually greatly affected by the local defect environment and, therefore, the structure of the absorption spectra of a particular defect can be used to generate a model of its local atomic and electronic structures.

Vibrational properties. Vibrational spectra associated with defects, along with the absorption spectra, may be used to characterise the local defect structure. Local vibrational modes are important for understanding of the mechanisms of non-radiative de-excitation of optically excited defects [122]. For example, quenching of the Yb^{2+} luminescence, also known as E-V transfer, due to the stretching modes of neighbouring CN^- ions has been observed in reference [52].

Over a the few decades, a large number of physical models and methods aiming to deal with these properties have been developed. Each has its advantages and disadvantages.

1.1.2 Models and methods

There are two main types of models which are used to describe point defects theoretically: the periodic model and the model of a single defect in crystal.

Periodic model. This approach stems from the band theory used to study the electronic structure of ideal crystals. An extended unit cell of a crystal with a defect is periodically translated producing essentially a new ideal crystal. Consequently, theoretical methods developed for periodic systems can be used to study such a crystal. In the case of charged defects, the effect of the Coulomb interaction of defects in different cells has to be compensated [129], [135], [110], [180]. Excited states can be studied using the periodic model only in certain cases. The quality of periodic simulations also suffers if the defect generates large distortions of the lattice which are not taken into account outside the unit cell. In some cases, when the dipole moment in each super-cell is large, the artificial Coulomb interaction between the super-cells is large even if they are electrically neutral.

Computer codes, which may be used to calculate point defects in periodic models, have been originally developed for the calculation of band structures of ideal crystals. The widely used codes are: VASP [123], [124], CASTEP [156], CETEP [32], and CRYSTAL [164], [54], [55]. The first three perform DFT calculations using plane-waves basis sets, while CRYSTAL performs both HF and DFT calculations using localised Gaussian-type basis set. Computer codes implementing the periodic model within the semi-empirical INDO [107] and tight-binding [212] levels are also available.

A single defect in a crystal. The obvious advantage of this model is that it can deal with an isolated defect and, consequently, defects charged with respect to the crystal lattice may be considered. On the other hand, the crystal symmetry is broken by the defect and only local symmetry can be used. A proper account of the interaction of the defect with the infinite but not periodic host crystal creates the major difficulty. Two major groups of methods, which are based on this model, divide the infinite crystal into a finite cluster, which includes the defect site, and the infinite environment. These methods are briefly described below.

Formal embedding methods. These methods aim to calculate an embedding potential without prior knowledge of the crystal electronic structure. In other word, the theoretical grounds of these methods are the same for ionic crystals and metals. The formal embedding methods may be divided into two approaches:

- **A perturbed cluster approach.** In this approach the Green function of the crystal with a defect is calculated iteratively. The calculation starts from the Green function of the ideal crystal and then the change due to the presence of the defect is computed. There are several versions of this approach known as i) *the matrix embedding potential*; ii) *the real-space embedding potential*; iii) *the Green functions matching technique.* In the first two methods the embedding potential is calculated in matrix form (in the space of basis set functions) and in the real space respectively [69]. In the third method the embedding potential is defined on a surface separating the cluster and the environment [101]. This potential is calculated so as to match the Green functions of the environment and of the cluster on the surface separating these regions. The embedding potentials obtained using these methods are energy dependent which makes their practical calculation a rather complicated task. These methods are formally correct if the perturbation is rigorously confined within the cluster region and, therefore, particularly useful for neutral defects and for systems with short screening length such as metals. If the defect potential extends outside the cluster, the embedding potential, which is still formally correct, becomes very difficult to calculate because the dimension of algebraic equations becomes very large or infinite. The EMBED code, implementing the perturbed cluster approach [162], [163] is the most widely used and, perhaps, the most developed program for these calculations.

- ii) **A corrective potential approach** aims to find an energy independent, and therefore, more easy to calculate embedding potential. However, even in the case of a highly localised defect, there will be an error inherent in the calculation of the correction.

Embedded molecular cluster method. In this group of methods the cluster is considered as an isolated molecule in the external field of the environment and electrons are confined within the molecule. This approach assumes that the electronic structure of the ions outside the cluster is not strongly modified by the presence of the defect. Calculation of the electronic structure of the cluster may be performed using any of the computer programs developed for molecular calculations, e.g. Gaussian98 [77], MOLCAS [5], GAMESS [179], [89] and others. The distortion and polarisation of the environment and their effect on the wave function of the cluster can then be modelled at different levels of accuracy. Since this approach has at present a far greater degree of versatility and applicability, it was employed in the work reported in this thesis. A description of the existing schemes and discussion of their advantages and disadvantages is the subject of this Chapter.

1.1.3 Definitions

The concept of the cluster and the environment was introduced above. In this section we will be more specific in defining these terms. The cluster is treated as a molecule usually using a quantum mechanical method originally developed for the calculation of molecules. For this reason it is often called a *molecular cluster* or *quantum mechanical (QM) cluster*. We will also refer to it as a "region of interest" for we need as accurate as possible description of processes which occur in the part of the crystal containing the defect while we account, approximately, for the presence and influence of the rest of the crystal.

Aims of the embedding. A commonly used approximation in cluster calculations is to ignore the interaction of the QM cluster with the rest of the crystal. This approximation can be particularly crude for ionic materials or materials with small screening constants in which the long range interaction and dielectric response of the environment can be significant or for metals (due to diffuse valence orbitals). To account for these and other interactions of the QM cluster with the environment, the former should be embedded into a potential representing the remaining crystal, which is called an *embedding potential*. The main objective of the embedded cluster approach is to find this potential, i.e. to include in a balanced and accurate way the effects of the surrounding solid on the electronic structure of the cluster which is considered to be responsible for the local properties under study.

Quantum Cluster. A QM cluster will be defined as a collection of one or more atoms, ions, or molecules which are treated quantum mechanically. The size of the QM cluster should be chosen so that the region of substantial redistribution of the electron density due to the perturbation by a defect is entirely within the cluster. In other words, an embedded cluster approach cannot be properly used to study electronic properties which have a spatial extent greater than that of the cluster. A more accurate definition of the QM cluster is difficult. The details of the cluster structure and conditions imposed on its boundaries are left to the discretion of a person studying the problem.

Environment. The rest of the crystal outside the region of interest is assumed to be free of any defects. Its electronic and geometric structures are assumed to be only slightly distorted. In particular, there is no bond breaking or bond making (in the case of ion-covalent crystals) and no other processes connected with charge density redistribution either in the ground or excited state. It is also assumed that there is no charge transfer from the QM cluster to the environment or vice versa. (Other, more sophisticated schemes where this assumption is not required have been mentioned above [101] and [162].)

Self-consistent calculation. Even neutral defects, e.g an anion-cation divacancy in an ionic crystal, can cause a substantial electronic and ionic polarisation of the environment. The potential at the defect site due to the polarised host lattice differs from that of the ideal crystal and, therefore, affects the electron density in the QM cluster, which, in turn, causes re-polarisation of the host lattice. We will call a calculation self-consistent in the mutual re-polarisation of the QM cluster and the environment is taken into account.

1.1.4 Requirements for cluster models

Finally we would like to outline some of the general requirements which a cluster model should meet. Since there is no general embedded cluster theory applicable to all types of chemical bonding, most such criteria are based on author's experience. In particular, the criteria formulated in [131] can be summarised as follows.

1. The cluster should give correctly the stoichiometry of the crystal being modelled.
2. Atoms equivalent to one another in the crystal should remain equivalent in the cluster irrespective of whether they are "inside" or at the boundary of the cluster.
3. The cluster modelling the bulk of a solid should be uncharged, reflecting the fact that the crystal is electrically neutral.[1]

---

[1] This condition is similar to the condition 1. Essentially it means that if the cluster is charged, it is not stoichiometric. Consequently, there is a question as to the number of electrons which should be attributed

4. The cluster should reflect correctly the electron density distribution in the crystal.
5. The energy levels of the cluster should reflect correctly the band structure of the crystal.
6. It is highly desirable that the quantum chemical methods applicable to the calculation of molecules should be applicable to the calculation of cluster without any significant modification and, in particular, without additional fitting parameters.
7. The model should be suitable for the largest possible number of types of crystal structures.
8. It should be suitable for modelling active centres at the surfaces
9. As the size of the cluster increases, the results should converge sufficiently rapidly to a limit which reflects the characteristics of the solid being studied.

As we will try to demonstrate in the next section, a number of different embedded cluster schemes have been developed which meet some of these conditions. However, in practical calculations, some of these schemes imply crude approximations; others are difficult to apply.

1.2 Examples of embedding

1.2.1 Isolated QM cluster

The basis of the *ab initio* solid state quantum chemistry of local properties of solids started to emerge in the sixties. By then, the calculations on solid $KNiF_3$ by Sugano and Shulman [201] promoted the central ideas of the cluster approximation. Having in mind the local character of some magnetic and spectroscopic properties of transition metal ions in crystals, they proposed to restrict the LCAO method to a small cluster of atoms formed by the transition element and its nearest neighbours. Within this unit they solved approximate forms of the Hartree-Fock-Roothaan equations. On the basis of the flatness of the electrostatic potential created by a point charge lattice within the cluster volume, they justified the complete neglect of the interactions between the cluster and the lattice. This isolated-cluster model, although approximate, pointed to the possibility of applying regular molecular quantum mechanical methods to the study of local properties of solids and very rapidly showed the necessity of solving the boundary problems associated with the finite size of the cluster.

It was demonstrated that the application of quantum chemistry methods to solid state problems is rather straightforward in the case of the isolated cluster approximation. However, it was left beyond doubt that this approximation can be very crude. In general, to provide an adequate description of even local properties of defects one has to account for presence of the infinite host lattice.

---

to the cluster. However, in the case of highly ionic crystal this question may be easy resolved. (PS)

1.2.2 QM cluster in the Madelung field

Many attempts have been made and are being made to improve the free cluster model by including corrections for the external long-range potential into the calculation. The fixed external potential V_{ext} can be defined [94] as a superposition of contributions $V_i(\mathbf{r})$ centred at the host crystal atom sites $\mathbf{R}_i$ of the cluster environment[2]:

$$V_{ext}(\mathbf{r}) = \sum_i^{env} V_i(\mathbf{r} - \mathbf{R}_i),$$

where each $V_i(\mathbf{r})$ is given by a multipole expansion:

$$V_i(\mathbf{r}) = \sum_{LM} \left(\frac{Q_{iLM}}{r^{L+1}} \right) Y_{LM}(\mathbf{r}).$$

In this expression Q_{iLM} are multipole moments and $Y_{LM}(\mathbf{r})$ are spherical harmonics. It is, however, very common to restrict the multipole expansion by monopole terms only or, at most, to monopoles and dipoles. Embedding schemes differ by the way the multipoles Q_{iLM} are determined and one-electron integrals $\langle \mu(\mathbf{r}, \mathbf{R}_\mu) | \, V_{ext}(\mathbf{r}) \, | \nu(\mathbf{r}, \mathbf{R}_\nu) \rangle$ are evaluated, where μ and ν are basis functions centred at $\mathbf{R}_\mu$ and $\mathbf{R}_\nu$ respectively. One of the procedures (see [86]) is based on the calculation of the difference between the potential due to an infinite periodic crystal, obtained using the CRYSTAL code for example, and that due to the cluster. The difference is least-square fitted to the classical electrostatic potential of a finite number of point charges q_i, located, e.g., at host lattice ion positions outside the QM cluster

$$V_{ext}(\mathbf{r}) = V_{crystal}(\mathbf{r}) - V_{cluster}(\mathbf{r}) = \sum_i \frac{q_i}{|\mathbf{r} - \mathbf{R}_i|}$$

The best fit is obtained by varying the values of the charges, keeping their positions fixed. Another example of the procedure, where results of the CRYSTAL slab calculation were used to fit the Madelung potential at the (001) LiF surface can be found in [28] and [168]. Other "potential-derived" multipoles representing long-range electrostatic potential of the cluster environment as applied to studies of polar and covalent crystals and large organic molecules have been used in [10], [19], [21], [31], [39], [176], [194]. In another scheme, suggested by Teunissen *et al.* [207], the charge density of the crystal and cluster is partitioned according to a generalised Mulliken scheme which allows expression of the electrostatic potentials in terms of the atomic multipole contributions

$$V_{ext}(\mathbf{r}) = \sum_i^{crystal} \sum_{LM} \frac{Q_{iLM}}{r^{L+1}} Y_{LM}(\mathbf{r} - \mathbf{R}_i) - \sum_j^{cluster} \sum_{LM} \frac{Q_{jLM}}{r^{L+1}} Y_{LM}(\mathbf{r} - \mathbf{R}_j)$$

---

[2] For the sake of brevity we will use notation of summation even if it is over infinite number of lattice sites, although Ewald summation should be used instead.

i.e., no fitting is involved. In the scheme by Lewandowski and Wilson [130] the Madelung potential at the QM cluster site is represented by Gaussian distributions of the charges centred at each ion of the environment. Parameters of the Gaussian distribution were fitted so that forces due to the environment at the QM atoms cancel those calculated for the free QM cluster.

Simpler schemes start from the Madelung potential for the bulk crystal using charges estimated from population analyses or from chemical considerations. For example, formal ion charges may be used for NaCl, while half ionic charges may be chosen for ion-covalent solids like SiO_2. There are two ways to include point charges into the Fock operator: as an Ewald sum [64], consisting from a direct space term and reciprocal space term, and as a finite number of point charges. The latter approach is based on an observation made by Evjen [63] for crystals with simple cubic structures that the net Coulomb potential converges very quickly if the summation is done by electrically neutral subgroups. A recent paper [219] extends this observation to a general case. The charge value and/or positions of some of these charges may be adjusted to reproduce the exact Madelung potential. The Ewald summation needs evaluation of special one-electron integrals while the representation of the potential using point charges is straightforward and requires only a trivial modification of the existing programs. In practical calculations of ionic systems the Madelung potential is often represented by a finite set of ionic charges [7], [13], [100], [140], [174]. It is worthwhile emphasising that the representation of the Madelung potential by a finite set of point charges is not a clearly defined procedure and depends on the choice of an investigator. It is well known [211] that the potential inside the finite sample depends on the surface of the sample. However, if the finite sample was built by extensions of a crystal unit cell with zero dipole moment, the electrostatic potential inside that sample calculated using direct summation differs from that obtained using the Ewald summation only by a constant [116].

If processes involving the change of the cluster charge state are considered, the model of an unpolarisable environment becomes unsatisfactory. It was realised that corrections to the ionisation potentials of surface defects due to the lattice response could be of the order of an electron-volt or more. Appreciable lattice relaxation was also expected for systems with large dipole moments like non-isovalent impurities compensated by nearby host crystal ion vacancies. In fact, calculated formation energies of point defects in the bulk of MgO [87] and of the excitation energies for S^{2-} and Se^{2-} doped MgO [152] show quite conclusively that *the lattice response needs to be consistently incorporated in calculations* of the defect electronic structure.

1.2.3 QM cluster in the polarisable environment

Perhaps the easiest and the most straightforward way to account for the lattice dielectric response and include its effect in the electronic structure of the QM cluster is to combine a quantum-mechanical treatment of the cluster with a classical treatment of the polarisable environment. This approach was implemented in the ICECAP code and is known as the ICECAP methodology [90]. The same approach was developed independently and reported in reference [189] and used in semi-empirical study of $[\mathrm{Li}]^0$ centre in MgO. The relevant key features of the ICECAP methodology can be summarised as follows. i) The cluster environment is treated using the Mott-Littleton approach [142] and its ions are described using the shell model [47]. ii) The environment is polarised so as to accommodate changes of the charge density of the QM cluster due to the presence of a defect. iii) A self-consistency procedure is employed so that the charge density of the cluster is be consistent with the polarisation of the environment. Below we briefly describe the shell model, the self-consistency procedure and other models of a polarisable crystal lattice related to that implemented in the ICECAP code.

Shell model. The shell model, which is widely used to represent polarisability in solids, was proposed by Dick and Overhauser [47]. The main feature of the model is that the short range inter-ionic interactions change as a consequence of the polarisation of the ions. In practice, each ion i is described by two point charges q_{ic} and q_{is} which are the charges of the *core* and *shell* respectively. The core and shell interact via a harmonic potential $\frac{1}{2}k_i r_{ic,is}^2$, where $r_{ic,is}$ is the distance between them. Cores and shells of *different* ions interact electrostatically and shells interact via short-range interatomic potentials which are used to parametrise all non-electrostatic interactions. The overall interaction energy, e, is given by:

$$e = \frac{1}{2}\sum_i \left(k_i r_{ic,is}^2 + \sum_{j\neq i} \left(V_{ij}^{lr} + V_{ij}^{sr} \right) \right), \tag{1}$$

where V_{ij}^{lr} and V_{ij}^{sr} are the long range and short range inter-ionic potentials (see also a footnote on page 20).

$$V_{ij}^{lr} = \frac{Q_{ic}Q_{jc}}{r_{ic,jc}} + \frac{Q_{ic}Q_{js}}{r_{ic,js}} + \frac{Q_{is}Q_{jc}}{r_{is,jc}} + \frac{Q_{is}Q_{js}}{r_{is,js}} \tag{2}$$

$$V_{ij}^{sr} = A_{ij}\exp(-r_{is,js}/\rho_{ij}) - \frac{C_{ij}}{r_{is,js}^6} \tag{3}$$

where r's are the distances between cores and shells of ions i and j, and A_{ij}, ρ_{ij}, C_{ij} are parameters of the short range, in this case the Buckingham, potential. Other types of interatomic and many-body potentials are also often used. The derivation of the parameters of the interatomic potentials is beyond the scope of the present work. The derivation of the shell model parameters and its application to problems of solid state physics and chemistry have been described in details in many papers and reviews (see e.g. [27], [23]).

ICECAP self-consistent procedure. The method implemented in the ICECAP code allowed for the relaxation of the classical environment in the field of charge density of the cluster and included the effect of the the lattice response on the cluster wave function.

The following scheme was used [91]:

1. Estimate charge distribution in the embedded QM cluster (e.g. ionic charges)
2. Compute distortion and polarisation of the cluster environment
3. i) Perform quantum mechanical calculation of the embedded cluster in the field of the environment. ii) Compute charge density in the cluster. iii) If the charge density has not converged, return to 2.
4. i) Relax atomic positions in the QM cluster. ii) If total energy minimum is not reached, return to 2.

Thus there are three nested self-consistency loops. The innermost loop is performed by a quantum mechanical method, e.g. HF method. The next one is in step 2 above: this is referred to as the multipole consistency loop, as it ensures that the electrostatic multipole moments of the QM cluster are the same as those which determine polarisation of the cluster environment. The outer-most loop of the program adjusts the positions of the atoms in the embedded cluster to minimise the total energy of the system. To remain within the "spirit" of the shell model, the charge density of the cluster at the step 2 is represented by dipole moments associated with each cluster atom. A similar model has been discussed in reference [189].

Other models of a cluster in polarisable lattice. There are several works which suggested other approaches to the problems of a QM cluster in the polarisable host lattice. A computational approach capable of modelling chemical reactions at solid-liquid interfaces was proposed in reference [197]. The main idea is to combine the embedded cluster molecular orbital or density functional methods for describing interactions at the surface of a solid with the dielectric continuum. Positions and magnitudes of point charges representing the electrostatic potential due to the dielectric continuum are recalculated at each cycle so that to compensate the electrostatic field due to the cluster. Similar schemes have been developed earlier for studies of zeolite-substrate interactions calculations [86] and for calculations of molecules in solutions [70], [121]. Approaches very similar to the ICECAP methodology were recently implemented in studies by Pascual and Seijo [154] and Donnerberg *et al.* [53]. A simpler version of this scheme was used by Eichler *et al.* [59] for the study of SiO_2 polymorphs and zeolites. In this scheme a quantum mechanical calculation of the cluster electronic structure was carried out without accounting for the Madelung potential due to the rest of the crystal. We were not able to use these methods and computer codes because they did not meet the criteria summarised in the Introduction. In particular, a limited range of *ab initio* methods was available and inefficient procedures for the energy minimisation were implemented.

1.2.4 Description of the quantum effects of surrounding lattice

So far we in our discussion the lattice surrounding of the QM cluster was described by classical ions. It has been shown that the results of embedded cluster calculations strongly depend on the cluster termination. For example, the effect of the cluster surroundings on the calculated ionisation potentials of F centres at the (001) MgO surface and on interaction of oxygen molecules with these centres is discussed in reference [67]. The results presented there suggest that the inclusion of the effective core pseudo-potentials of the surrounding cations reduces the ionisation potential of the surface F^+ centre (F_s^+) by almost 50% (from 7.0 eV to 3.7 eV), reduces the dissociation limit $O_2/F_s \rightarrow O_2^- + F_s^+$by more than 25% (from 8.49 eV to 6.27 eV), and increases the adsorption energy of O_2 molecule on the surface F centre (F_s) by 0.9 eV. Other examples of MgO studies in which an anion terminated cluster have been used can be found in [7] and [165]. It has been noted that termination schemes can cause artificial polarisation of ions at the cluster boundary, in particular anions, resulting in incorrect behaviour of the electrostatic potential [66]. In the case of cation terminated QM clusters the effect of artificial polarisation of the boundary ions is small and does not affect results of the calculations drastically. This may be explained by i) much smaller polarisability of cations as compared to the polarisability of anions and ii) by the fact that cations of the first coordination sphere already provide good confinement of the anion's charge density [75], [76].

It is now a well established feature of any embedded cluster calculation that the finite size of the ions of the cluster-environment interface, in general both cations and anions, should be taken into account. This is equivalent to adding a localising potential to the cluster Hamiltonian or Fock operators. Three methods which enable us to account for the finite size effect have been and are used in practical calculations. The simplest is to terminate the quantum cluster by cations which are described using a large core effective core pseudo potential developed, for example, by Hay and Wadt in [216], [92]. This approach works well for compounds containing light cations like Na or Mg but requires additional corrections in the case of heavier cations (see examples of "perfect lattice" tests in Chapter 2). However, a more systematic approach requires a significantly deeper analysis.

Adams-Gilbert approach. The localising potential based on the Adams-Gilbert equation was suggested by Kunz and Klein in [126] and developed by Kunz and Vail in [127]. In this approach the Fock equation for the crystal:

$$\widehat{F}\varphi_i(\mathbf{r}) = \epsilon_i\varphi_i(\mathbf{r}), \quad i = 1, 2, ..., N \tag{4}$$

is to be reduced to that for a finite cluster A within the crystal. The manifold of occupied states k could be unitarily transformed so that N_A electrons of the cluster A occupy states $k(A)$ localised in the cluster vicinity. The rest $N_B = N - N_A$ crystal electrons occupy states $k(B)$ which are orthogonal to the states $k(A)$. Thus, the Fock equation for the cluster becomes

$$(\widehat{F}_A + \widehat{V}_A)\psi_k = \epsilon_k \psi_k, \quad k = 1, 2, ..., N_A, \tag{5}$$

where $\widehat{F}_A$ is that part of the crystal Fock operator, which is associated with A, and potential $\widehat{V}_A$ is the residue, which depends on the states $k(B)$: $\widehat{F} = \widehat{F}_A + \widehat{V}_A$. Part of the potential $\widehat{V}_A$ may be associated with the Madelung potential of the cluster environment and the rest with a short-range potential arising from the quantum mechanical nature of the electrons: $\widehat{V}_A = \widehat{V}_A^M + \widehat{V}_A^S$. We shall use the fact that if $\rho_A = \sum |k\rangle \langle k|$ is a projection operator onto the manifold of occupied states $k(A)$ and $\widehat{W}$ is an arbitrary one-particle operator, then

$$\rho_A \widehat{W} \rho_A |k\rangle = \begin{cases} \rho_A \widehat{W} |k\rangle & \text{if } |k\rangle \text{ is occupied} \\ 0 & \text{if } |k\rangle \text{ is unoccupied} \end{cases}$$

Therefore, modification of the cluster equation (5)

$$(\widehat{F}_A + \widehat{V}_A^M + \widehat{V}_A^S + \rho_A \widehat{W} \rho_A) |k\rangle = \pi_k |k\rangle, \quad k = 1, 2, ..., N_A$$

will leave the total energy and the charge density unchanged. Kunz and Klein [126] have chosen $\widehat{W} = -\rho_A \widehat{V}_A^S \rho_A$ and argued that in the limit of self consistency it would cancel the $\widehat{V}_A^S$ term, yielding

$$(\widehat{F}_A + \widehat{V}_A^M) |k\rangle = \pi_k |k\rangle$$

The term $\widehat{W} = -\rho_A \widehat{V}_A^S \rho_A$ was called the Kunz-Klein localising potential (KKLP). Practical calculations of the KKLP may be carried out using the following procedure:

1. Electron density of the cluster environment is written as a sum over lattice ion sites $j(B)$

$$\rho_B = \sum_{j(B)} \rho_j, \quad \rho_j = \sum_{k'(j)} \psi_{k'}(\mathbf{r}) \psi^*_{k'}(\mathbf{r}),$$

   where $k'(j)$ labels orbitals on site j.

2. The $\widehat{V}_A^S$ is calculated using an iterative procedure [127].

3. The value of $\widehat{V}_A^S$ obtained is fitted to a set of Gaussian type functions to make its application in the quantum mechanical calculations straightforward.

The KKLP has been implemented in the ICECAP program. It has been tested on a number of cases, but has not received wide applications due to limitations of the ICECAP code itself.

***Ab initio* model potential (AIMP).** Another approach based on an *ab initio* model potential for the ions of the cluster environment has been developed by Barandiaran and Seijo in [13] and [14] and later by Pascual and Seijo [154]. The potential is a practical implementation of the group function theory developed by McWeeny [137] (in the context of intermolecular interactions) and Huzinaga *et al.* [99], [97] (in the context of frozen core molecular calculations). The potential, associated with each atom outside the QM cluster has long range (electrostatic) and short range components $\widehat{V} = \widehat{V}^{lr} + \widehat{V}^{sr}$. The long range potential of the ith ion is, in general, represented by the Coulomb potential due to two point charges corresponding to core (q_{ic}) and shell (q_{is}) of the shell model (1.2.3)

$$\widehat{V}_i^{lr}(\mathbf{r}) = \widehat{V}_{ic}^{lr}(\mathbf{r}) + \widehat{V}_{is}^{lr}(\mathbf{r}) = \frac{q_{ic}}{|\mathbf{r}-\mathbf{r}_{ic}|} + \frac{q_{is}}{|\mathbf{r}-\mathbf{r}_{is}|}.$$

The corresponding short range potential is localised at the shell site and has the form:

$$\begin{aligned} \widehat{V}_i^{sr}(\mathbf{r}) &= \sum_p \frac{A_p^i \exp(-\alpha_p^i(\mathbf{r}-\mathbf{r}_{is})^2)}{|\mathbf{r}-\mathbf{r}_{is}|} \\ &+ \sum_l \sum_{m=-l}^{+l} \sum_{q,r} |\chi_{lm}^q(\mathbf{r}); i\rangle\, A_{l;qr}^i\, \langle \chi_{lm}^r(\mathbf{r}); i| \qquad (6) \\ &+ \sum_{t=1}^{N_{occ}} B_t^i \left|\varphi_t^i(\mathbf{r})\right\rangle \left\langle \varphi_t^i(\mathbf{r})\right|. \end{aligned}$$

The first term in (6) is the short range Coulomb potential of the environment ion i due to non-point nature of its charge density. Its parameters A_p^i and α_p^i are calculated by a least-square fitting to the true Coulomb potential $(q_{ic} + q_{is} - Z_i)/r + \widehat{J}_i(r)$, where $\widehat{J}_i$ is the one-electron Coulomb operator associated with the many electron wave function Φ_i of the ion i. The second term is the exchange model operator of the ion i: functions $|\chi_{lm}^q; i\rangle$ define a set of primitive Gaussian type functions for each ion i and are used in the expansion of its occupied orbitals φ_t^i; the parameters $A_{l;qr}^i$ are elements of the matrix $\mathbf{A}^i = (\mathbf{S}^i)^{-1}\mathbf{K}^i(\mathbf{S}^i)^{-1}$, where $\mathbf{S}^i$ and $\mathbf{K}^i$ are the overlap matrix and matrix of the exchange operator $\widehat{K_i}$ in the basis of the $|\chi_{lm}^q; i\rangle$ functions respectively. Finally, the third term is the projection operator of the ion i which appears due to the restricted variational treatment [99], [97] and prevents the collapse of the cluster wave function onto the environmental ion i. Coefficients $B_t^i = 2\varepsilon_t^i$, where ε_t^i are the one electron energies of the functions φ_t^i and N_{occ} is the number of occupied orbitals associated with the ion i. It is important to stress that all three terms in (6) are calculated directly from the set $\{\varphi_t^i\}$ once the latter is known.

Practical calculation of the AIMP involves a set of embedded ion calculations, one per crystal component, which are iteratively repeated up to convergence in the orbitals. The procedure has been illustrated for the example of CaF_2 [154]. i) The Ca^{2+} ion is embedded into a perfect lattice and its one-electron orbitals are calculated; the same is done for the F^- ion. ii) The orbitals obtained in the first step are used to generate short range potentials $\widehat{V}_{Ca^{2+}}^{sr}$ and $\widehat{V}_{F^-}^{sr}$. iii) The potentials $\widehat{V}_{Ca^{2+}}^{sr}$ and $\widehat{V}_{F^-}^{sr}$ are used to calculate new orbitals for the Ca^{2+} and F^- ions as in i). The calculations are repeated until the convergence is achieved. The calculated potentials are then stored in a database and may be used for calculations of any point defects in the CaF_2 lattice.

1.2.5 Towards ion-covalent (polar) crystals

In crystals with covalent bonds the valence electrons cannot be assigned to specific atoms, but rather belong to bonds. To have a meaningful cluster model, one has to cut the bonds which extend outside the cluster. The "dangling bonds" created result in artificial states appearing in the forbidden gap of the crystals. Saturation of these bonds may be achieved using i) mono-valent (hydrogen) atoms, ii) modified hydrogen atoms or pseudoatoms and iii) special pseudopotentials. These cluster models will be discussed in this section for the example of SiO_2 and $AlPO_4$ crystals.

Mono-valent atoms. The easiest and chemically best defined procedure for terminating such a cluster is to saturate the dangling bonds with monovalent, usually hydrogen, atoms. The electronegativity of the hydrogen atom is intermediate between that of oxygen and silicon and it can be used to saturate both Si- and O-terminated bonds [175], [177]. It was, however, noted that the embedding potential is better if hydrogen is used to saturate oxygen terminated bonds, i.e. it is considered as one quarter of a silicon ion. Recently, this approach was used, for instance, in cluster studies of the properties of defects in SiO_2 [148], [149], [150]. Fluorine atoms can also serve as saturating atoms as was shown in [41] and [42] in the context of zeolite models. Saturation of dangling bonds with H or F atoms has the following problems: i) because of the electronegativity mismatch, the Si-H and H-O bonds will be polarised with respect to the Si-O bond; ii) in the case of organic molecules the interaction of two hydrogen atoms may result in formation of spurious H-bonds; iii) problems arise when attempts are made to embed a H-saturated cluster into an array of point charges to reproduce the Madelung potential [119].

Pseudoatoms. Another possibility is to saturate a dangling bond by a pseudo-atom. This should be again a mono-electron atom but somehow modified with respect to hydrogen. This is useful when the pseudo-atom is used to represent a "quarter" of P^+ or Al^- ions in an $AlPO_4$ crystal; the nuclear charge of the pseudo-atom should be modified to $\frac{5}{4}$ and $\frac{3}{4}$ respectively. Another way to modify the hydrogen atom is to "correct" its electronegativity. This can be easily achieved by variation of the exponential factor of its single Slater- or Gaussian-type basis function [166]. Pseudoatoms terminating QM clusters are an essential feature of the developing area of Quantum Mechanics / Molecular Mechanics (QM/MM) studies of large organic molecules. The terminology "link atom" is also often used in these studies to indicate that the pseudo atom is used to link the QM cluster to the classical representation of the remaining molecule. Different models of link atoms were described in reviews [175], [177].

Pseudopotentials. Less intuitive but more systematic approaches to the terminating atoms employ a specially defined potential centred at the pseudo-atom. In the method of the orbitally stoichiometric cluster [132], a complete set of valence orbitals for the border atoms is defined. Then, orbitals which form bonds with other atoms inside the QM cluster are included into the model basis set and corresponding electrons - into the quantum chemical calculation. Electrons, which are associated with the remaining orbitals are replaced by an angle dependent pseudo-potential. A similar approach has been used in studies of large molecular systems at the semi-empirical level [208]. Another approach was suggested by Abarenkov [2]. He has shown that for any one-electron function φ and its energy ε, it is possible to find a non-local correction W to the Hamiltonian operator H of the hydrogen atom so that the function φ will be the ground state function of the operator $H + W$. The correction term W is called the *separable embedding potential.* Using this potential one can construct a mono-valent atom which will have a predefined ground state function and energy. In particular, this ground state function can be chosen as a hybrid orbital originating from a polar bond. This approach is currently being implemented for calculations of molecules [1]

Reviews [175] and [177] provide numerous examples of the application of embedded cluster approach to crystals with ion-covalent and covalent bonds.

1.3 Embedding approach based on group functions theory

So far we have described different approaches to the embedding problem where the interaction of the cluster with its environment was described using semi-intuitive approaches. Most of the methods described above aim at "improvement" of an intuitive cluster model, rather than at its development from the first principles. However, there has been a number of more rigorous theoretical approaches to the problem of embedding as applied to solid state problems and large molecules. For example, an exact treatment of the electronic structure of embedded molecules is discussed by Adams in [3]. A related question of the derivation of the proper effective equations for embedded molecules, fragments and clusters was raised by Huzinaga *et al.* [98], Seijo and Barandiarán [183] and Mehler [139]. In the next section we outline the main ideas of the Group Function (GF) Theory developed by McWeeny [138] which provides a basis for rigorous calculations of the cluster wave function in the field of the rest of the crystal. Then, in section 1.3.2, we discuss how the GF formalism can be simplified to obtain a less computationally demanding method for embedded cluster calculations.

1.3.1 Group function theory

General wave function. Two non-interacting systems A and B of N_A and N_B electrons can be described by wave-functions Φ^A and Φ^B respectively. These functions are called *group functions* (GF). We shall assume that the interaction between the groups A and B

is weak in the sense that they retain their individuality at least to a good approximation. To describe a system of $N_A + N_B$ electrons, one can use a function

$$\Phi(\mathbf{x}_1, \mathbf{x}_2, ...) = M\hat{A}\left[\Phi^A(\mathbf{x}_1, ..., \mathbf{x}_{N_A})\Phi^B(\mathbf{x}_{N_A+1}, ..., \mathbf{x}_{N_A+N_B})\right], \tag{7}$$

where $\hat{A}$ is the antisymmetrisation operator. Functions of this type are known as generalised products. More generally, each of the system A, B,.. can be in one of their states a, b,.. Therefore corresponding group functions should have two indexes, one for the subsystem and one for its electronic state, Φ_a^A, Φ_b^B,.. Consequently, the wave function of the system of $N_A + N_B + ...$ electrons is

$$\Phi_k = M_k\hat{A}\left[\Phi_a^A\Phi_b^B...\right] \quad (k = Aa, Bb, ...), \tag{8}$$

where k is the generalised index used to describe the electronic states of all subsystems. A refinement of the wave function of the system of $N_A + N_B + ...$ can be achieved by mixing different Φ_k which corresponds to the Configuration Interaction (CI) expansion:

$$\Psi = \sum_k C_k\Phi_k. \tag{9}$$

Strong orthogonality. Generalised products Φ_k can be handled in the same way as products of one-electron functions (spin-orbitals) if the *strong-orthogonality* condition is imposed on the group functions Φ_r^R:

$$\int \Phi_r^R(\mathbf{x}_1, \mathbf{x}_i, \mathbf{x}_j, ...)^*\Phi_s^S(\mathbf{x}_1, \mathbf{x}_k, \mathbf{x}_l, ...)d\mathbf{x}_1 \equiv 0 \quad (for\, R \neq S). \tag{10}$$

This condition is much stronger than the usual orthogonality condition:

$$\int \Phi_{r_2}^R(\mathbf{x}_1, \mathbf{x}_2, .., \mathbf{x}_{N_R})^*\Phi_{r_1}^R(\mathbf{x}_1, \mathbf{x}_2, .., \mathbf{x}_{N_R})d\mathbf{x}_1 d\mathbf{x}_2 ... d\mathbf{x}_{N_R} = \delta_{r_1 r_2}, \tag{11}$$

which is normally assumed for wave functions of different states allowed within each group. The strong orthogonality condition (10) is satisfied, if many-electron functions Φ_r^R and Φ_s^S are built from, for example, different sets of orthogonal spin-orbitals. Thus the CI expansion (9) disregards the possibility of "electron transfer" between the different groups. This approximation is, however, not a significant one. Indeed, if the effect of the electron transfer between two groups is large, the individuality of the two groups is lost and the group-function description would be physically inappropriate.

Variational principle. The total energy of the system composed from the subsystems A, B,.. being in their electronic states a, b,... is then expressed by

$$E = \sum_R H^R(rr) + \sum_{R<S}\left[J^{RS}(rr, ss) - K^{RS}(rr, ss)\right], \tag{12}$$

where $H^R(r_1r_2)$ is the usual matrix element of a Hamiltonian for N_R electrons of the group R alone, taken between the states $\Phi^R_{r_1}$ and $\Phi^R_{r_2}$. Integrals $J^{RS}(r_1r_2, s_1s_2)$ and $K^{RS}(r_1r_2, s_1s_2)$ are generalisations of the usual two-electron Coulomb and exchange integrals:

$$J^{RS}(r_1r_2, s_1s_2) = \int g(1,2)\rho_R(r_1r_2|\mathbf{x}_1)\rho_S(s_1s_2|\mathbf{x}_2)d\mathbf{x}_1d\mathbf{x}_2, \tag{13}$$

$$K^{RS}(r_1r_2, s_1s_2) = \int g(1,2)\rho_R(r_1r_2|\mathbf{x}_2;\mathbf{x}_1)\rho_S(s_1s_2|\mathbf{x}_1;\mathbf{x}_2)d\mathbf{x}_1d\mathbf{x}_2, \tag{14}$$

where function $g(i,j) = \frac{1}{r_{ij}}$ is inverse distance between two electrons and $\rho_R(r_1r_2|\mathbf{x})$ and $\rho_R(r_1r_2|\mathbf{x}_1;\mathbf{x}_2)$ are one- and two-electron transition density matrix for the states described by $\Phi^R_{r_1}$ and $\Phi^R_{r_2}$. We require that E is stationary with respect to first order variations of all Φ^R_r. Since each variation makes its own first order change to E let us consider only one $\Phi^R_r \to \Phi^R_r + \delta\Phi^R_r$. Then, the energy of the group R in the field of other groups is:

$$E^R_{eff} = H^R(rr) + \sum_{S(\neq R)} \left[J^{RS}(rr,ss) - K^{RS}(rr,ss)\right], \tag{15}$$

where the first term corresponds to the "self-energy" of the group R and terms in brackets represent interaction of the group R with all other groups. The wave function Φ_k of the system of $N = N_A + N_B + ...$ electrons may be optimised by considering only one group at a time, replacing an N-electron calculation by a succession of smaller calculations on systems of N_A, N_B,.. electrons. The interaction terms in (15) can be expressed as matrix elements of *one*-electron operators describing the potential due to an electron outside the group R. We introduce the following operators for any group S acting on any one-electron function $\varphi(\mathbf{x})$:

$$\left.\begin{array}{rl} J^S(1)\varphi(\mathbf{x}_1) = & \left[\int g(1,2)\rho_S(ss|\mathbf{x}_2;\mathbf{x}_2)d\mathbf{x}_2\right]\varphi(\mathbf{x}_1) \\ K^S(1)\varphi(\mathbf{x}_1) = & \int g(1,2)\rho_S(ss|\mathbf{x}_1;\mathbf{x}_2)\varphi(\mathbf{x}_2)d\mathbf{x}_2 \end{array}\right\}. \tag{16}$$

These operators are the "Coulomb" and "Exchange" operators in the effective field due to the electrons of the group S. The interaction terms in (15) can now be expressed in the form of the expectation values of the interaction with electrons of the group S:

$$\left.\begin{array}{r} J^{RS}(rr,ss) = \left\langle \Phi^R_r \middle| \sum_{i=1}^{N_R} J^S(i) \middle| \Phi^R_r \right\rangle \\ K^{RS}(rr,ss) = \left\langle \Phi^R_r \middle| \sum_{i=1}^{N_R} K^S(i) \middle| \Phi^R_r \right\rangle \end{array}\right\}. \tag{17}$$

The electrons of the group R thus behave as if they were alone but each is in the field described by the one-electron Hamiltonian

$$h^R_{eff} = h^R + \sum_{S(\neq R)} (J^S - K^S) \tag{18}$$

instead of h^R. The effective energy of the group R can then be written as

$$E^R_{eff} = \left\langle \Phi^R_r \right| H^R_{eff} \left| \Phi^R_r \right\rangle, \tag{19}$$

where

$$H^R_{eff} = \sum_i^{N_R} h^R_{eff}(i) + \frac{1}{2} \sum_{i \neq j}^{N_R} g(i,j). \tag{20}$$

The stationary value condition for E^R_{eff} becomes:

$$E^R_{eff} = \frac{\left\langle \Phi^R_r \right| H^R_{eff} \left| \Phi^R_r \right\rangle}{\langle \Phi^R_r | \Phi^R_r \rangle} = \text{stationary value} \tag{21}$$

In this expression all groups other than R have been formally eliminated but their presence has been absorbed into the effective one-electron Hamiltonian (18). Consequently, calculation of the wave function of the system of $N = N_A + N_B + \ldots$ electrons has been reduced to a set of calculations of a smaller system of N_R electrons, where index R runs through all groups $A, B, ..$ This result has far reaching consequences and might be directly applicable to ionic and ion-covalent crystals. In these crystals the electron density is mostly localised on ions or bonds. One may then associate group functions with each ion or bond and reduce the problem of the quantum mechanical calculation of a crystal to the problem of a much smaller calculations of ions and bonds.

1.3.2 Atomistic representation of the Environment

Model of central molecule. One of the first HF schemes applied to studies of localised properties of point defects in ionic solids was proposed by Petrashen *et al.* in 1973 [160]. The idea of the scheme was similar to that of the group function theory but formulated independently of McWeeny.

These authors considered optical properties of F-centres in alkali halides. In this case, the defect is electrically neutral and the perturbation introduced by the defect decreases relatively fast with the distance from it. Consequently, the electronic structure of the ions of the host crystal remains essentially unchanged and one can, therefore, say that properties of the system associated with the defect are determined by a molecule which: i) contains the defect itself and ions of the host crystal close to it and ii) is in the potential of the remaining crystal. The size of this molecule, which was called the Central Molecule (CM), is determined by the perturbation due to the defect. The wave function of the crystal with the defect Ψ was written in the form (7):

$$\Psi(\mathbf{X}|\mathbf{R}) = \Psi(\mathbf{X}', \mathbf{X}'', \mathbf{R}) = \hat{A}[\psi(\mathbf{X}', \mathbf{R})\varphi(\mathbf{X}'', \mathbf{R})], \tag{22}$$

where $\mathbf{X}'$, $\mathbf{X}''$, $\mathbf{R}$ are coordinates of electrons of the CM, coordinates of electrons of the rest of the host crystal and coordinates of all nuclei respectively, and $\psi(\mathbf{X}', \mathbf{R})$ and $\varphi(\mathbf{X}'', \mathbf{R})$

are the single determinant wave functions of the CM and the rest of the crystal. In the adiabatic approximation the electronic problem can be separated from the motion of the nuclei. Then, the operator of the electron energy of the system can be written as

$$\hat{H}_{el}(\mathbf{X}', \mathbf{X}'', \mathbf{R}) = \hat{H}_1(\mathbf{X}', \mathbf{R}) + \hat{H}_2(\mathbf{X}'', \mathbf{R}) + \hat{H}_3(\mathbf{X}', \mathbf{X}'', \mathbf{R}),$$

where each of the Hamiltonians includes terms that depend on the corresponding coordinates only and equations for the functions $\psi(\mathbf{X}', \mathbf{R})$ and $\varphi(\mathbf{X}'', \mathbf{R})$ become:

$$[\hat{H}_1(\mathbf{X}', \mathbf{R}) + \hat{V}_1(\mathbf{X}', \mathbf{R})]\psi(\mathbf{X}', \mathbf{R}) = W_1(\mathbf{R})\psi(\mathbf{X}', \mathbf{R}), \tag{23}$$

$$[\hat{H}_2(\mathbf{X}'', \mathbf{R}) + \hat{V}_2(\mathbf{X}'', \mathbf{R})]\varphi(\mathbf{X}'', \mathbf{R}) = W_2(\mathbf{R})\varphi(\mathbf{X}'', \mathbf{R}). \tag{24}$$

In the expressions above W_1 and W_2 are adiabatic potentials of the CM and its environment respectively, and yet undefined operators $\hat{V}_1$ and $\hat{V}_2$ account for potential due to one system acting on the other. It is clear that the operators in brackets correspond to H^R_{eff} of equation (20). Although the condition of the strong orthogonality (10) has not been explicitly specified, it was assumed that functions $\psi(\mathbf{X}', \mathbf{R})$ and $\varphi(\mathbf{X}'', \mathbf{R})$ are localised in different regions of space and effects of their overlap may be neglected. This assumption allowed Petrashen *et al.* to write an expression for operator $\hat{V}_1$ as a sum of operators which represent a potential energy of an electron from the CM in the potential of the rest of the crystal and $\hat{V}_2$ has the same meaning but for electrons of the environment:

$$\hat{V}_1(\mathbf{X}', \mathbf{R}) = \int \varphi^*(\mathbf{X}'', \mathbf{R})\hat{H}_3(\mathbf{X}', \mathbf{X}'', \mathbf{R})\varphi(\mathbf{R}'', \mathbf{R})d\mathbf{X}''$$
$$\hat{V}_2(\mathbf{X}'', \mathbf{R}) = \int \psi^*(\mathbf{X}', \mathbf{R})\hat{H}_3(\mathbf{X}', \mathbf{X}'', \mathbf{R})\psi(\mathbf{X}', \mathbf{R})d\mathbf{X}'$$

Finally, the expression for the adiabatic potential of the whole "defect in crystal" system becomes:

$$W(\mathbf{R}) = W_1(\mathbf{R}) + W_2^0(\mathbf{R})$$

where $W_2^0 = \int \varphi^* \hat{H}_2 \varphi dx''$. Again, as in (1.3.1) we arrived at an expression for the adiabatic potential of the "crystal with defect" system where the wave-function of the environment is formally eliminated.[3]

Further simplifications of the model have been based on the relation of Mollwo-Ivey for absorption energy ΔE of F-centres in alkali halides

$$\Delta E a^n = c$$

where a is a crystal lattice constant and n and c are constants. This relation suggests that the absorption energy hardly depends on the nature of the host lattice ions and justifies the representation of the host lattice using locations of the ions and their charges only,

---

[3] The wave-function of the environment does not disappear of course. It is still present in potential $\hat{V}_1$.

which constitutes the model of the unpolarisable lattice (see (1.2.2)). The polarisation of the lattice was also introduced for the CM ions using correction terms

$$W_1' = \frac{1}{2}\sum_{ij} q_i q_j \left\{ \frac{1}{|\mathbf{R}_i - \mathbf{R}_j|} - \frac{1}{\left|\mathbf{R}_i' - \mathbf{R}_j'\right|} \right\}$$

$$W_1'' = \frac{1}{2}\sum_{ij} \left\{ W_{rep}\left|\mathbf{R}_i - \mathbf{R}_j\right| - W_{rep}\left|\mathbf{R}_i' - \mathbf{R}_j'\right| \right\}$$

$$W_1''' = -\frac{1}{2}\sum_{i} \alpha_i \mathbf{E}_i^2,$$

for the long range and short range interactions of ions and deformations of their electronic clouds respectively. In the expressions above α_i is polarisability of the ion i and $\mathbf{E}_i$ is the value of electrostatic field at the ion site. Results of these calculations could be found in [158] and [159].

Expression of the total energy via multipole moments of ions of the environment. In this section we rewrite the expression for the total energy of the crystal with the defect in an alternative form using a multipole representation of the electron density. This form allows us to make further mathematical simplifications in a way which has a clear physical interpretation.

The approach proposed by Kantorovich in [108] and [109] is based on the GF method (see above) and earlier ideas by Tolpygo [210] of the two-step variation of the total energy. The idea of the method is to express the total energy of the system E in terms of multipole moments Q_{lm}^i induced on the ions of the cluster environment. The expression for the total energy then allows a simple and straightforward interpretation. Most of the mathematical details of this method are omitted and only its main ideas and final results are outlined.

The wave functions of ions in the crystal Φ_i are expanded over the functions of free ions Φ_i^μ with coefficients c_i^μ : $\Phi_i = c_{i0}\Phi_i^0 + \sum c_{i\mu}\Phi_i^\mu$. Then, the multipole moments on each ion induced with respect to the free ion density are:

$$Q_{lm}^i = -N_i \sum_{\mu} \left(c_{i\mu} \langle i0|\, lm \,|i\mu\rangle + C.C. \right), \tag{25}$$

where

$$\langle i0|\, lm \,|i\mu\rangle = \sqrt{\frac{4\pi}{2l+1}} \int S_{lm}(\mathbf{r}) r^l \rho_i(\mathbf{r};\mathbf{r}|\mu 0) d\mathbf{r}, \tag{26}$$

where $\rho_i(\mathbf{r};\mathbf{r}|\mu 0)$ is a transition density matrix between the states Φ_i^0 and Φ_i^μ for a free ion i. At the first step, variation of E with respect to coefficients $c_{i\mu}$ is undertaken subject to the condition that the induced multipole moments Q_{lm}^i remain constant on each ion.

Thus, the functional to vary is no longer E but

$$\overline{E} = E + \sum_{ilm} \lambda_{lm}^{i} \left(Q_{lm}^{i} + \left(N_i \sum c_{i\mu} \left\langle i0 \right| lm \left| i\mu \right\rangle + C.C. \right) \right) \tag{27}$$

where λ_{lm}^{i} are Lagrangian multipliers. As a result of the variational procedure we obtain expressions for the coefficients $c_{i\mu}$ which include multipliers λ_{lm}^{i}:

$$c_{i\mu} = c_{i\mu}(\lambda_{lm}^{i}). \tag{28}$$

These solutions for $c_{i\mu}$ are then substituted into equation (25) to obtain multipliers λ_{lm}^{i} as functions of the multipole moments Q_{lm}^{i}. Consequently, coefficients $c_{i\mu}$ can be expressed as functions of Q_{lm}^{i} using (28). Thus, the total energy E is expressed in terms of Q_{lm}^{i} which completes the first step of the variational procedure.

The total energy of the crystal with the defect is a sum of three contributions:

$$E = E_{clus} + E_{env} + U_{clus-env}.$$

The energy of the QM cluster remains unaffected by the previous discussion, i.e $E_{clus} = \left\langle \Phi^{clus} \right| H_{clus} \left| \Phi^{clus} \right\rangle$, but in the two other terms, multipole moments of the ions of the environment appear:

$$E_{env} = \frac{1}{2} \sum_{ij} J_{ij}^{0} + \frac{1}{2} \sum_{ij} \mathbf{Q}_i^{+} \mathbf{D}_{ij} \mathbf{Q}_j - \sum_{ij} \mathbf{Q}_i^{+} \mathbf{G}_{ij} + \frac{1}{2} \sum_{ij} \omega_{ij} + \frac{1}{3} \sum_{ijk} \omega_{ijk} \tag{29}$$

$$U_{clus-env} = - \int \rho(\mathbf{r}) V(\mathbf{r}) d\mathbf{r} - \sum_{i} \mathbf{Q}_i^{+} \mathbf{G}_i + U_{c-e}^{exc}. \tag{30}$$

In expression (29), the first three terms describe the electrostatic interaction of the ions of the environment: J_{ij}^{0} - is the interaction of the unperturbed densities ρ_i^0 and ρ_j^0 of ions i and j, $\mathbf{Q}_i^{+} \mathbf{D}_{ij} \mathbf{Q}_j$ - the interaction of induced multipole moments, $\mathbf{Q}_i^{+} \mathbf{G}_{ij}$ - the interaction of induced multipoles with the charge density distributions ρ_j^0 of the unperturbed ions j and the last two terms, ω_{ij} and ω_{ijk}, account for the two- and three-body short range interactions. The terms in (30) have a similar meaning: $V(\mathbf{r})$ - is the electrostatic potential at the cluster site due to densities ρ_i^0 of all ions of the environment and $\rho(\mathbf{r})$ is the density of the cluster, $\mathbf{Q}_i^{+} \mathbf{G}_i$ is the interaction of induced multipoles of ion i with the cluster and U_{c-e}^{exc} is the exchange interaction of the cluster and environment. Note that, owing to the strong orthogonality condition (10), short range many-body interactions of order higher than three do not appear in (29). The variation of the total energy E with respect to the multipoles $\mathbf{Q}$ should be undertaken to find its minimum.

Expressions (29) and (30) provide a theory that is simple but still, within the group function approach, a rigorous form of the energy of the environment and cluster-environment interaction. This form is particularly suitable for making further approximations and replacing terms in (29) and (30) by their classical counterparts.

1.4 Summary

The brief analysis given above demonstrates that existing schemes of embedded cluster calculations are not free of disadvantages, some of which can be summarised as follows: i) the electrostatic potential due to the environment at the QM cluster site is neglected; ii) the quantum mechanical calculation of the forces on the QM cluster atoms is unavailable; iii) the charge density of the QM cluster is fitted by a distribution of monopoles and dipoles; iv) the effect of the polarised environment on the electron density of the QM cluster is neglected; v) only a limited number of *ab initio* methods is available for defect calculations; vi) no effective schemes are available for the calculation of excited states with proper account of lattice polarisation.

Therefore there is a need for a new embedded cluster code, which would be based on a high quality package for the *ab initio* calculations and provide consistent treatment of localised charged defect states taking into account the polarisation of the environment. The requirements for this code are summarised at the beginning of the next Chapter. In the remaining part of the next Chapter the theoretical background, details of the practical implementation, and tests of the new code for embedded calculations are given.

2 GUESS: methodology and tests

The aim of the present Chapter is to describe a methodology which would enable us to *predict* models of defects and mechanisms of defect processes in insulators. The method was implemented in a computer code named GUESS (Gaussian Used for Embedded System Studies) which is also described in this Chapter. The main features we wanted to achieve include:

- flexibility with respect to the QM methodologies to allow us to use several *ab initio* methods including those which account for electron correlation;
- effectiveness with respect to geometry optimisation and calculation speed to enable calculation of large QM clusters and complex defects and processes;
- calculation of charged defects and processes associated with charge transfer and change of defect charge state;
- calculation of spectroscopic defect properties with account of lattice polarisation;
- calculation of both bulk and surface defects including low-coordinated and charged features at surfaces;

Using these criteria at the first stage of the method development we decided to employ the Gaussian98 code, which has the following advantages: i) it is a well developed and tested package; ii) it includes several quantum-mechanical methods including Hartree-Fock and Density Functional approaches, perturbation theory, coupled-clusters, and other methods for high quality *ab initio* calculations; iii) it is well documented and open to further development. It also has the prototype features, which are only present in a rudimentary form in most other codes. These include point charge arrays, Natural Population Analysis, and availability to implement several DFT functionals. We believe that the experience acquired with this code will allow us to apply successfully the same approach to other quantum-chemical packages.

To treat lattice polarisation, in this work we employ the shell model. This model has been used for calculations of properties of ionic crystals and defects for many years and is well parametrised. However, we should note that our approach can be generalised to other techniques, such as the model of polarisable ions.

In this Chapter we describe our model and program for embedded cluster calculations. The shell model description of the cluster environment will be derived from the expression for the total energy of the environment (see equation (29) of Chapter 1) in section 2.1. Section 2.2 deals with details of the practical realisation of the shell model for the purposes of the embedded cluster scheme and the description of the implementation of the computer code. The tests of the computer code are described in section 2.3. The embedding scheme will be applied to a number of well established systems to provide a general test of the model in section 2.4.

2.1 Quantum cluster in the polarisable environment

In Chapter 1, we outlined the main ideas of the group function theory and its application to calculation of the total energy of a system of weakly interacting sub-systems. In this section we apply the GF approach particularly to a system of an ionic crystal with a point defect. The total energy for this system was re-written in sub-section 1.3.2 in an alternative form (29) which makes use of multipole moments of the ions of the environment. This forms enables us to make further, physically transparent, approximations regarding the electronic structure of the environment.

We assume that among all multipoles $\mathbf{Q}_i$ associated with an ion i of the environment only the monopole q_i and dipole $\mathbf{d}_i$ significantly contribute to the total energy and all higher multipoles can be neglected. Consequently, one has to decide how to represent the charges q_i and dipoles $\mathbf{d}_i$ in practical calculations. Two widely applied models may be used i) a model of polarisable ions and ii) the shell model. The former model deals with the monopoles and point dipoles located at the centres of ions. The shell model has been briefly described above in section 1.2.3. In this work we favour the shell model the advantages of which were summarised on page 36.

The two- and three body short range interactions which appear in equation (29) can be well reproduced by classical many-body potentials. In the case of cubic systems, three body terms may often be neglected and the remaining two-body interaction is usually parametrised using Buckingham or Morse potentials. The change of the internal energy of an ion due to its polarisation (diagonal part of the second term in equation (29)) is described by $\frac{1}{2}\mathbf{d}_i(\alpha^{-1})_{ii}\mathbf{d}_i$, where α^{-1} is an inverse polarisability tensor. The dipole moment of a shell model ion is represented by a vector pointing from the ion's core to its shell in a coordinate system associated with the core. Consequently, the dipole moment is $\mathbf{d}_i = q_{i,shell}(\mathbf{r}_{i,shell} - \mathbf{r}_{i,core})$. If the polarisability of a crystal is isotropic, then the corresponding term reduces to $\frac{1}{2\alpha_i}\mathbf{d}_i^2 = \frac{q_{i,shell}^2}{2\alpha_i}(\mathbf{r}_{i,shell} - \mathbf{r}_{i,core})^2$. The coefficient $\frac{q_{i,shell}^2}{\alpha_i}$ defines the force constant k_i of the spring which connects the $q_{i,core}$ and $q_{i,shell}$. It can be shown that first, third, and non-diagonal parts of the second terms of expression (29) may be written in the form of Coulomb interaction of cores and shells of different ions (see equation (2)). The overall interaction energy of the ions of the environment reduces, therefore, to expression (1) on page 22. It is important to stress that this result was not postulated but obtained from general GF formulation.

The expression for the cluster-environment interaction energy (equation (30) on page 34) can also be simplified. If the multipole expansion $\mathbf{Q}_i$ is restricted to the monopole and dipole contribution, the first two terms of equation (30) can be incorporated into $\int \rho_{clus}(\mathbf{r})V_{ext}(\mathbf{r})d\mathbf{r}$, where $\rho_{clus}(\mathbf{r})$ is the charge density of the QM cluster and $V_{ext}(\mathbf{r})$ is the electrostatic potential produced by the distribution of the pairs of point charges (shell model ions) representing the ions of the environment. The third term of (30) may be parametrised using either classical potentials or quantum mechanical operators of general type:

$$U = \sum_{ij} |\psi_j\rangle \, U_{ij}(\mathbf{r}) \, \langle\varphi_j| \, ,$$

where U_{ij}, ψ_i and φ_j are known functions, or a combination of both.

Results of this section will be used below in the formulation of the expression for the total energy of a QM cluster in the field of a polarisable environment.

2.2 The embedded cluster calculation: practical realisation

2.2.1 Model for the embedded cluster calculations

The model for the embedded cluster calculations will be described in this sub-section. Its relation to the Mott-Littleton model [142] of a crystal with a point defect is shown in Fig. 1. Firstly, we outline features, which are similar for both models, and then emphasise the differences. In both models, ions of polarisable region I are represented using the shell model [47] (see also Chapter 1). If the defect site is charged with respect to the host lattice, polarisation correction to the energy of region II and energy of its interaction with region I are also taken into account. Ions in finite region IIa are represented using the shell model, while infinite region IIb is treated in the continuum approximation. The two models differ in i) the treatment of the defect site and ii) the calculation of the Madelung potential in region I. Following the very idea of an embedded cluster approach, the defect site and a few nearest host crystal ions are included in the QM cluster. Calculation of the Madelung potential in the Mott-Littleton model is carried out using summation over the infinite crystal. In the present model, this summation is replaced by the calculation of the electrostatic potential from a large finite region.[4] This finite region, which from now on we refer to as a nano-cluster, incorporates region I (Fig. 1(b)). The purpose of the external part of the nano-cluster (outside region I) is to ensure the correct electrostatic potential and its derivatives inside region I. Atoms in that region are represented by rigid point charges fixed at the ideal crystal sites. Relative sizes of region I and the nano-cluster are defined so that the electrostatic potential in region I calculated via summation over all centres of the nano-cluster was equal (up the a constant) to the Madelung potential calculated using the Ewald summation over the infinite lattice. It is convenient, although not necessary, to keep the spherical region I at the centre of the nano-cluster. The generation of the nano-cluster and the calculation of the electrostatic potential inside the nano-cluster are discussed below.

Calculation of the Madelung potential. In practice, calculation of the Madelung potential due to the infinite crystal is cumbersome and in some cases unnecessary. Usually, the Madelung potential is calculated using Ewald summation [64]. Calculation of the matrix elements of the Ewald sum over the basis functions of the QM cluster has, however,

---

[4] As we discuss below, the finite nano-cluster representation of the crystal provides a Madelung potential which is not less accurate but more straightforward to calculate.

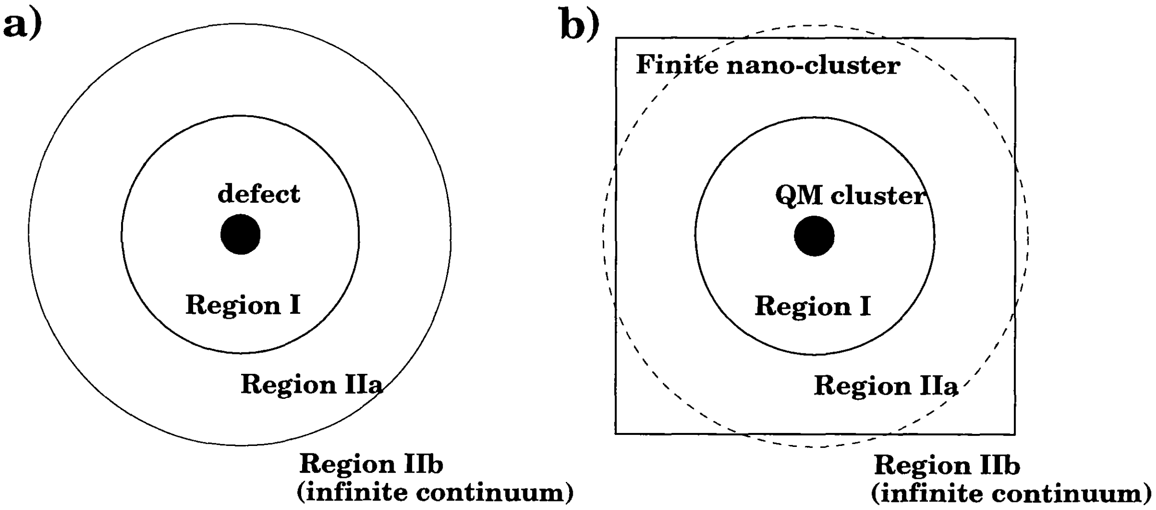

Figure 1: Crystal with a point defect: relation of the conventional two-region model (a) to the model for embedded cluster calculations (b).

two obvious disadvantages: i) it is time consuming and ii) the computer code for these calculations, if available, needs to be incorporated in existing packages for an *ab initio* calculations. Another, simpler, approach is to represent the Madelung potential inside the region of interest via a finite distribution of point charges, which can be calculated using, for example, methods outlined in section 1.2.2. In the present model, the Madelung potential is calculated as a sum of contributions from all centres of a nano-cluster. The nano-cluster is constructed by translation of a building-block, which usually coincides with one of possible choices of a crystal unit cell. If this building-block possesses no dipole moment, then the electrostatic potential inside the nano-cluster converges (up to a constant) to the potential inside the infinite crystal as the size of the nano-cluster increases. The magnitude of this constant was derived analytically (see [116] and references therein). For cubic crystals the analytical expression for the constant shift has a very simple form. In the case of the $LiBaF_3$ nano-cluster which is discussed below in this Chapter, the electrostatic potential inside the finite nano-cluster agrees up to a constant with the result of the Ewald summation in a region which is two unit cells away from the surface of the nano-cluster. The magnitude of the constant shift of the potential in this case is close to 4.0 V. In the case of rock-salt crystals, the electrostatic potential in region I becomes very close to the potential calculated using Ewald summation even for a nano-cluster of a relatively modest size. For example, in the case of a cubic nano-cluster of the size of $20\times20\times20$ ions the deviation of the electrostatic potential in the inner cubic $12\times12\times12$ region from the exact Madelung potential was less than $6\cdot10^{-4}$ V at the boundary of the inner region and less than $1\cdot10^{-4}$ V at its centre. Similarly, the electrostatic field at ions calculated for an inner region of the nano-cluster and for an infinite crystal differs by 10^{-4} V/Å.

2.2.2 Calculation of the total energy and forces

Calculation of the total energy of the QM cluster embedded in the classical environment is carried out in a similar way to that described in references [186], [185] and [214]. In the case of the neutral defect one can neglect polarisation of the host lattice beyond region I or, in other words, neglect the contribution from the polarisation of region II to the system's total energy, which then becomes:

$$E = \langle \Phi | H_0 + V_{NC} | \Phi \rangle + E_{NC} + U_{QM-I},$$

where H_0 is the Hamiltonian of a free QM cluster and Φ is the wave-function of the cluster in the external potential V_{NC}; V_{NC} is the electrostatic potential due to point charges Q_i^{Mad} of the cores and shells of the nano-cluster; E_{NC} is the interaction energy of the classical atoms of the nano-cluster polarised in the presence of the defect; U_{QM-I} is the short range interaction of the atoms of the QM cluster with their classical neighbours in region I. These terms can be expanded as follows:

$$V_{NC} = \sum_i^{NC} \sum_j^{QM} \frac{Q_i^{Mad}}{|R_i - r_j|} + \sum_i^{NC} \sum_j^{QM} \frac{Q_i^{Mad} Z_j}{|R_i - R_j|},$$

$$E_{NC} = \frac{1}{2} \sum_{ij}^{NC} \frac{Q_i^{Cl} Q_j^{Cl}}{|R_i - R_j|} + \frac{1}{2} \sum_{ij}^{NC} W_{ij} + \frac{1}{2} \sum_i^{I} k_i \rho_i,$$

$$U_{QM-I} = \sum_i^{I} \sum_j^{QM} W_{ij},$$

where r_i refers to the coordinates of electrons in the QM cluster, R_i - the coordinates of the nuclei in the QM cluster and cores and shells in the nano-cluster, Z_i - the charge of the nuclei in the QM cluster, Q_i^{Cl} - the charge of the classical centre (core or shell), W_{ij} - the short range interaction of ions i and j; k_i and ρ_i are the spring constant and the core-shell separation for polarisable ion i in the region I. Note that there are two sets of charges for classical ions. Set $\left\{Q^{Mad}\right\}$ is used to calculated Madelung potential in the region I while $\left\{Q^{Cl}\right\}$ is a part of a larger set of parameters used in the classical simulation of crystal properties. The difference between $\left\{Q^{Mad}\right\}$ and $\left\{Q^{Cl}\right\}$ and methods of calculation of the $\left\{Q^{Mad}\right\}$ are described in more details in section 2.2.4. The term U_{QM-I} is due to quantum mechanical (non-Coulomb) interactions of host lattice ions inside and outside the QM cluster. These interactions are parametrised using classical short-range interatomic potentials.

If the defect is charged, polarisation of the host lattice cannot be neglected. The polarisation energy of region II and the correction term due to the interaction of the polarised infinite region II with region I are calculated using the Mott-Littleton approach [142]. The interaction of the polarised region II with atoms of the QM cluster is also calculated classically using $U_{II-QM} = \sum_i^{QM} \varphi_i Q_i^{qm}$, where φ_i is the electrostatic potential due to the defect induced polarisation of region II calculated at the position of the nucleus of the ith QM ion and Q_i^{qm} are point charges fitted to reproduce the electrostatic potential due to the density of the QM cluster in the classical environment.

The vector of total force acting on centre i, either an atom in the QM cluster or a core or shell in the classical environment, is calculated as the negative derivative of the system's total energy with respect to the coordinates of the centre: $\mathbf{F}_i = -\overrightarrow{\nabla}_i E$. For the sake of brevity we do not write out the expanded expression for the force $\mathbf{F}_i$.

2.2.3 Organisation of the total energy minimisation of the system

First, we describe the energy minimisation procedure for a defect in the bulk of an infinite 3D crystal and finite nano-cluster, then highlight the advantages of the present scheme and, finally, outline the main features of its computer code implementation.

The energy minimisation scheme. It is easier to start with the case of the neutral defect in the bulk crystal; the extension of the scheme to the case of the charged defect and the case of low-coordinated systems will be given at the end of this section. The block-scheme of the energy minimisation procedure for the neutral defect in the bulk crystal is shown in Fig 2(a). The minimisation starts with the calculation of the system total energy E_0 and of total forces $\{\mathbf{F}\}_0$ acting on each centre for the initial configuration $\{\mathbf{R}\}_0$ of the system. The initial direction of relaxation $\{\mathbf{h}\}_0$ is chosen along the vector of forces $\{\mathbf{F}\}_0$. Each minimisation cycle consists of four steps, which are described on an example of step $i+1$:

1. Choose the length t_{i+1} of the displacement along the direction of relaxation $\{\mathbf{h}\}_{i+1}$ and calculate the new geometric configuration $\{\mathbf{R}\}_{i+1}$ according to $\{\mathbf{R}\}_{i+1} = \{\mathbf{R}\}_i + t_{i+1}\{\mathbf{h}\}_{i+1}$.

2. Calculate the total energy E_{i+1}. If E_{i+1} is lower than E_i - adopt the new geometry $\{\mathbf{R}\}_{i+1}$, otherwise repeat the step 1. with smaller t_{i+1}.

3. Calculate the vector of the total forces $\{\mathbf{F}\}_{i+1}$ for the adopted configuration $\{\mathbf{R}\}_{i+1}$.

4. Check whether the calculation is converged; if not, calculate the new direction of the relaxation $\{\mathbf{h}\}_{i+2}$ according to the standard BFGS method [44] and return to step 1.

The calculation is completed when typical convergence criteria are satisfied: the change in the total energy of the system is less than 10^{-5} eV; the displacement of any centre is

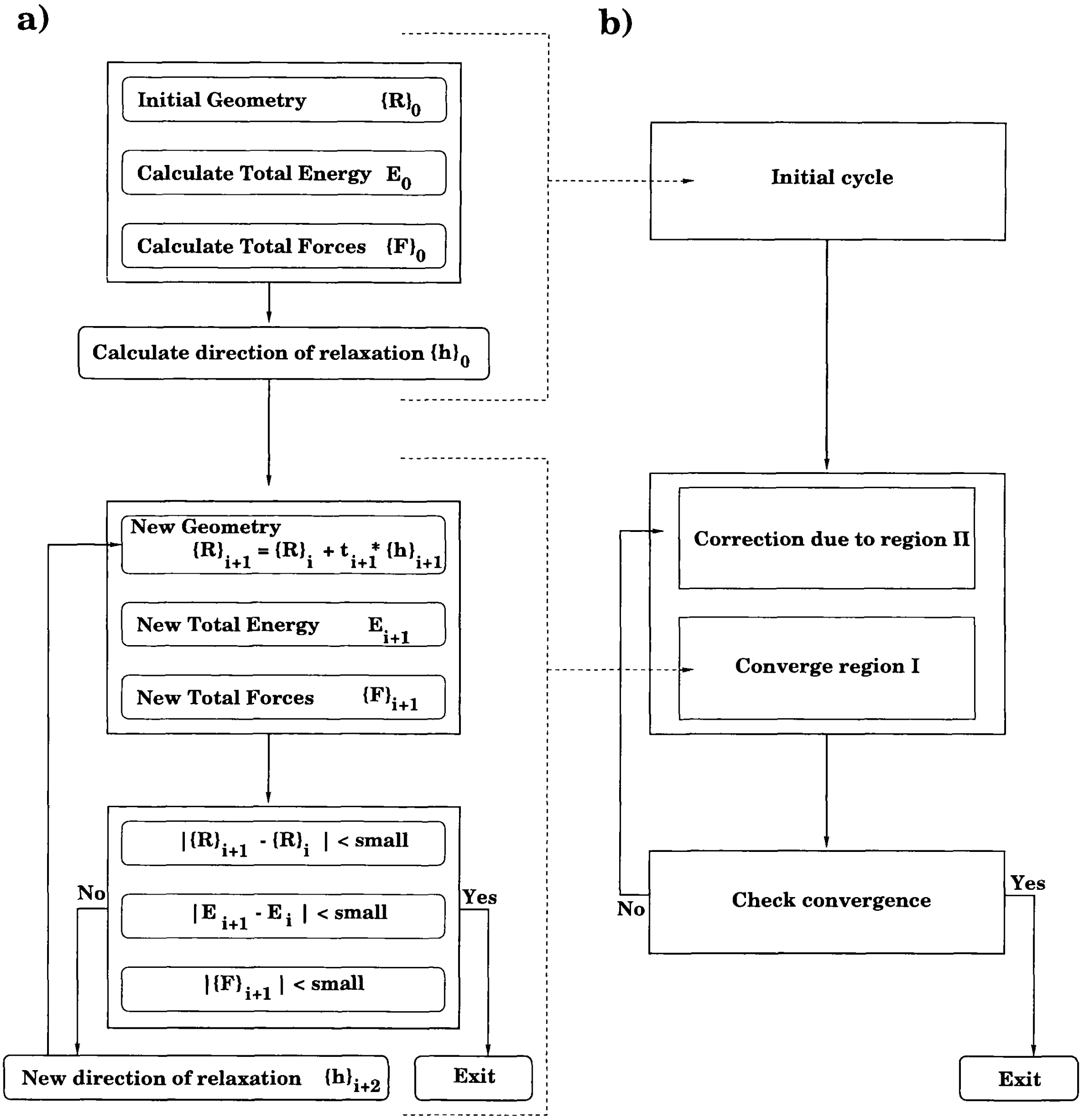

Figure 2: Organisation of the energy minimisation procedure.
a) model of the finite nano-cluster; b) model of the infinite crystal.

smaller than $3{\cdot}10^{-4}$ Å, and the total force acting on any centre is smaller than $3{\cdot}10^{-2}$ eV/Å.

In the case of charged defects, polarisation of the infinite host lattice should be taken into account. To do so, after the calculation of the total energy (step 2) the charge density of the QM cluster is represented by a finite set of point charges Q^{qm} (see previous paragraph), which then is used in the standard Mott-Littleton scheme to calculate the defect induced polarisation energy of the infinite region, the correction to the interaction of the regions I and II, the correction to the electrostatic potential and forces at all centres in region I due to the infinite region II. The corresponding block-scheme is shown in Fig. 2(b). These corrections are calculated at the initial geometry and then recalculated each time after the convergence criteria for region I are satisfied.

In the current realisation of the embedded cluster calculation scheme, the presence of the infinite crystal can be taken into account only in the case of the 3D infinite crystal. In the case of the surface or other systems with broken 3D translational symmetry the crystal is modelled by a finite nano-cluster and corrections due to infinite region II are unavailable.

Advantages of the present scheme. In previous programs for embedded cluster calculations the total forces acting on atoms in the QM cluster were not calculated. Therefore, the search for the optimal configuration of the QM cluster was done "by hand", i.e. the classical environment was relaxed for each particular configuration of atoms in the QM cluster using the following "self-consistent" procedure. After the electronic structure of the QM cluster is calculated, the cores and shells of the classical environment were allowed to adjust their positions in response to the charge distribution within the QM cluster. Then the electronic structure of the QM cluster was recalculated to accommodate the changes of the embedding potential and this cycle was repeated until the change of the total energy became smaller than a specified threshold. Naturally, as only a finite number of configurations could be "probed" in this way, high quality geometry optimisation for large clusters was a very cumbersome and sometimes impossible task.

In the present scheme the forces are calculated on both QM and classical ions. This allow us to minimise the total energy of the system simultaneously with respect to electronic and nuclear coordinates of atoms of quantum mechanical and classical sub-systems and avoid the time-consuming "self-consistency" procedure.

Computer implementation. The energy minimisation is performed using an interface program which combines computer codes for *ab initio* calculations of molecules and classical calculations of crystals. In the present studies, the electronic structure of the embedded QM cluster - terms $E_{QM} = \langle\Phi|\, H_0 + V_{NC}\,|\Phi\rangle$ and $-\vec{\nabla} E_{QM}$ (see section 2.2.2) - have been calculated using the Gaussian98 package [77] and corrections to the total energy and forces due to the polarised region II - using the GULP package [79]. These packages "interact" via an interface program, which performs all other necessary computations (see section 2.2.3).

2.2.4 Reference charges

As already mentioned in section 2.2.3, the complete scheme of embedded cluster calculations implies two sets of charges to reproduce the ionic character of the classical ions. The set $\left\{Q^{Cl}\right\}$ is a part of a larger set of parameters for the shell model calculations of the crystal. These charges are fitted together with parameters of classical short range potentials, e.g. Buckingham or Morse, and spring constants for the shell model ions to reproduce known properties of ideal crystals. Usually these charges have formal values corresponding to the number of valence electrons, e.g. +1 for Ag and -1 for Cl ions respectively in AgCl or +2 for Mg and -2 for O ions in MgO. In general, embedding of the QM cluster in the electrostatic field of formal charges will lead to an overestimated Madelung potential. The error is negligible for highly ionic crystals like NaCl, but might be significant for less ionic and polar crystals like AgCl and SiO_2. To avoid this problem the QM cluster is embedded into an electrostatic potential of charges $\left\{Q^{Mad}\right\}$ which are, in general, different from $\left\{Q^{Cl}\right\}$.

One can think about several possible ways to determine $\left\{Q^{Mad}\right\}$. We describe two approaches used in the present study. In both cases, atoms of the QM cluster and classical environment are kept at their ideal crystal lattice sites. Then the following iterative procedure is applied:

1. The charge density of a QM cluster embedded into an initial $\left\{Q^{Mad}\right\}_0$ is calculated.
2. The charge density is analysed; an ionic charge is assigned to each atom in the QM cluster and the charge of each sub-lattice of the crystal is determined as the average of the charges of all corresponding ions.
3. New set $\left\{Q^{Mad}\right\}_i$ is built from the charges obtained at the step 2. The next iteration starts with the step 1.

The calculation is completed when the charges $\left\{Q^{Mad}\right\}_i$ and $\left\{Q^{Mad}\right\}_{i+1}$ obtained in two consequent iterations are the same within the required accuracy. One can assign an ionic charge to each atom of the QM cluster either on the basis of population analysis, i.e. Mulliken, Bader or Natural population analysis, or by fitting the electrostatic potential due to QM cluster at the ions of the environment. The charges $\left\{Q^{Mad}\right\}_i$ obtained using the latter fitting procedure and the NPA population analysis are very close at least for the case of almost completely ionic crystals.

2.2.5 Quantum mechanical clusters

Structure of the QM clusters. As discussed earlier (see section 1.2.4), the results of embedded cluster calculations can be dramatically affected by the boundary conditions.

Following that discussion we build up a QM cluster so that every anion is fully coordinated by cations (unless low-coordinated anion sites are studied). Boundary cations are treated using effective core pseudo-potentials replacing all but valence electrons ("large core" pseudo-potentials) and a very contracted, usually minimal, basis set. Anions and non-boundary cations are usually treated as all-electron atoms. The QM clusters used in the present work will be described in more detail in the following Chapters.

Corrections to the QM cluster energy. Ionic compounds of metals when there are no valence nd or $(n+1)s$ electrons formally present, e.g. Ca^{2+} in CaO, cannot be properly described using large effective core pseudo-potentials (ECP). In these cases the electrons and nucleus of the other atom begin to penetrate the charge cloud of ns and np shells and the expression for the core-core interaction $V_{core-core} = \frac{Z_A^{eff} Z_B^{eff}}{R_{AB}}$ breaks down, a dramatic example of which is given in [92] for the CaO molecule where use of the ECP to replace all but $4s$ electrons led to a strictly attractive interaction of the atoms with the adiabatic potential exhibiting no minimum. Similar features of large core ECPs have been noticed in [88]. However, from the point of view of computational cost, it is very desirable to use as large an ECP as possible for boundary cations of the QM cluster. To achieve this one can make a correction to the interaction energy of two large core atoms of the form: $W = A \exp\left(-\frac{r}{\rho_0}\right)$, where r - is the distance between the two atoms and A and ρ_0 are parameters. This approach have been used previously in reference [187]. Current implementation of this correction allows a more general expression for the correction

$$W = A \exp\left(-\frac{r}{\rho_0}\right) - \frac{C}{r^6}.$$

The latter term could be important, as the van der Waals interaction inside the QM cluster is usually poorly reproduced unless very high quality *ab initio* calculations are performed. We demonstrate the use of this option later, for the example of the $LiBaF_3$ perfect lattice test.

Nano-cluster: example of $LiBaF_3$. To generate a nano-cluster one has to choose an electrically neutral unit cell and replicate it in all three dimensions, which is demonstrated for the example of the $LiBaF_3$ crystal. This crystal has a simple cubic structure (Fig. 3). One of the possible choices of the unit cell is with the Ba atom at the centre of the cube with fractional coordinates (0.0 0.0 0.0), eight Li atoms at the corners of the cube with coordinates equivalent to (0.5 0.5 0.5) and twelve F atoms at the middle points of the cube edges with coordinates symmetry equivalent to (0.5 0.5 0.0). Following the ideas of Evjen [63] we associate with each corner Li atom and edge F atom only $\frac{1}{8}$ and $\frac{1}{4}$ of their ionic charges respectively and define it as a cluster $Ba_1(\frac{1}{8}Li)_8(\frac{1}{4}F)_{12}$. Replication of the unit cell in the x direction forms a cluster where (Fig. 3), four Li atoms appear at the edges and carry $\frac{1}{4}$ of the Li ionic charge and one F atom is now at the surface and carries $\frac{1}{2}$ of

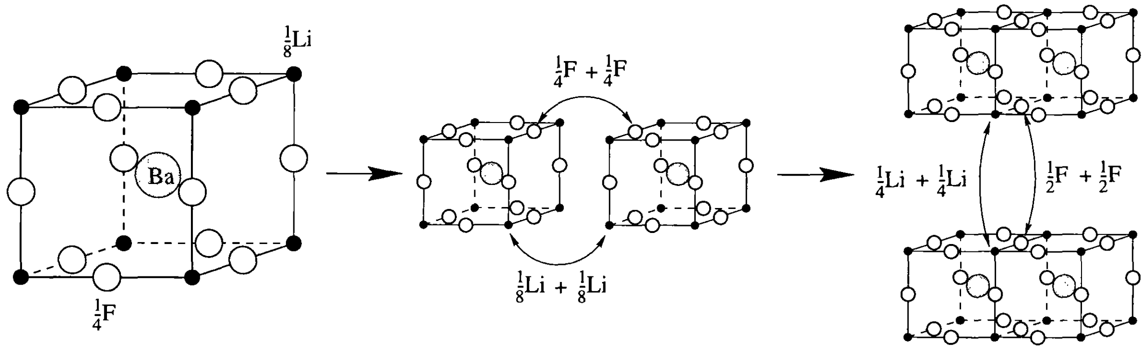

Figure 3: Generation of the nano-cluster from electrically neutral unit cell. Example of $LiBaF_3$ crystal.

its ionic charge. Further replication of the unit cell produces a nano-cluster where fully coordinated atoms in its bulk have total ionic charges and atoms at the surfaces, edges and corners have fractional charges.

2.2.6 *Ab initio* methods, calculation of defect properties

***Ab initio* methods.** Throughout this work we have used several *ab initio* methods implemented in the Gaussian98 package. Ground state properties were studied using both restricted (RHF) and unrestricted (UHF) Hartree-Fock (HF) [138], and Density Functional (DF) [153] methods. Most of the DF calculations have been done using hybrid three parametrical functional with gradient corrections (B3LYP) developed by Becke (see references [15] and [16]). Optical absorption energies have been calculated using a single excitation configuration interaction (CIS) method in which a wave function of the excited state is calculated as a linear combination of all single excitations from the reference RHF or UHF single determinant wave function of the ground state [72]. More advanced, post Hartree-Fock, methods have also been used to improve the quality of results. These methods included the Configurational Interaction technique with Single and Double excitations from the reference single determinant HF wave function (CISD) and Complete Active Space Self Consistent Field (CASSCF) method [184]. In the latter case the wave function is built as a linear combination of all possible excitations from the reference single determinant HF wave function within a given active space. We do not explain details of these methods for their complete description can be found in the references given above.

Calculation of ionisation potentials. To calculate "vertical" ionisation potentials we adopted the following scheme. First, the ground state of the system was completely relaxed, i.e. we found the geometrical configuration of the quantum mechanical and classical centres (both cores and shells) corresponding to the minimum of the total energy, E_{gr}. Then one electron was removed from the system and the total energy of the system was recalculated including electronic relaxation only in the QM cluster. This energy is referred to as $E_{IP(0)}$. Then, according to the Frank-Condon approximation, both shells of the classical environment and the electronic structure of the QM cluster are allowed to relax to the energy $E_{IP(I)}$. Ionisation potentials corresponding to a model of the QM cluster embedded in unpolarisable and polarisable lattices are calculated as $IP(0) = E_{IP(0)} - E_{gr}$ and $IP(I) = E_{IP(I)} - E_{gr}$ respectively. The difference between $IP(0)$ and $IP(I)$ is mainly due to high frequency polarisability of the crystal lattice and can be as large as 1.0 eV.

Calculation of vibrational frequencies. Vibrational frequencies and corresponding vectors are calculated using the harmonic approximation as eigenvalues and eigenvectors of the dynamical matrix $\mathbf{D}$:

$$D_{ij}^{\alpha\beta} = \frac{1}{\sqrt{m_i m_j}} \frac{\partial^2 E}{\partial x_{i\alpha} \partial x_{j\beta}}$$

where i and j refer to the atoms (i, j = 1, .., N) and α and β refer to their Cartesian coordinates (α, β = 1,2,3), m_i and m_j are the masses of the atoms and E is the total energy of the system. Consequently, $\mathbf{D}$ is a square matrix of size $3N \times 3N$, where N is the total number of atoms used in the calculation. The second derivative of the total energy E with respect to atomic coordinates is calculated numerically using the central differencing formula:

$$\frac{\partial^2 E}{\partial x_{i\alpha} \partial x_{j\beta}} = \frac{1}{4h^2} \left[E_{i\alpha,j\beta}^{++} + E_{i\alpha,j\beta}^{--} - E_{i\alpha,j\beta}^{+-} - E_{i\alpha,j\beta}^{-+} \right],$$

where $E_{i\alpha,j\beta}^{+-}$, for example, is defined as

$$E_{i\alpha,j\beta}^{+-} = E(x_{i\alpha} + h, x_{j\beta} - h)$$

and h is the finite size step for numerical differentiation. The matrix of second derivatives is symmetrical and requires $\frac{3}{2}N(3N+1)$ entries to be calculated. In addition, every calculation of the second derivative requires 4 calculations of the total energy. Obviously, the calculation of the dynamic matrix is very time consuming and, at present, is feasible only for a small number of atoms. Usually, only a few characteristic modes of the vibrational spectrum are important. In that case the dynamic matrix is calculated using the frozen environment approximation, i.e. for the few atoms which are likely to participate in those modes.

2.3 Tests of the computer code

In this subsection we describe the calculations undertaken to test the reliability of the computer code which implements the above embedded cluster scheme.

Calculation of the total force. In the case of a crystal represented by a finite nano-cluster only (with no polarisation contribution from the region II), an obvious condition is that the vector sum of forces acting on all centres of the nano-cluster should be strictly zero:

$$\mathbf{F} = \sum_{i}^{All} \mathbf{F}_i = 0.$$

If this condition does not hold, $\mathbf{F} \neq 0$, the nano-cluster will un-physically accelerate in the free space. Due to numerical errors the above condition is not perfectly satisfied. In the case of small clusters of the size of 20-30 atoms a typical value of $|\mathbf{F}|$ is about 10^{-8} eV/Å; in the case of large nano-clusters including up to 4000 atoms value of $|\mathbf{F}|$ does not exceed 10^{-5} eV/Å.

Analytical and Numerical forces. For a geometry optimisation procedure to be valid, total forces and the total energy of the system should be consistent. This consistency can be checked by comparing analytical $\mathbf{F}_i^{an}$ and numerical $\mathbf{F}_i^{num}$ forces acting at every centre i. Disagreement between $\mathbf{F}_i^{an}$ and $\mathbf{F}_i^{num}$ shall indicate that the code is incorrect. The component α of the force acting on a centre i is calculated analytically and numerically as:

$$F_{i\alpha}^{an}(x_{i\alpha}) = -\frac{\partial E(x_{i\alpha})}{\partial x_{i\alpha}}$$

and

$$F_{i\alpha}^{num}(x_{i\alpha}) = -\frac{E(x_{i\alpha} + h) - E(x_{i\alpha} - h)}{2h}$$

respectively, where h - is a finite step for the numerical differentiation. For the step h = 0.01 Bohr the difference between $F_{i\alpha}^{an}$ and $F_{i\alpha}^{num}$ is typically as small as 10^{-5} eV/Å for systems containing several thousands of atoms. For smaller systems this difference decreases by one or two orders of magnitude.

Diatomic molecule. A diatomic molecule is the simplest example of the system where geometry optimisation could be thoroughly tested. Five out of six degrees of freedom of this molecule can be fixed to prevent small drift and rotation of the molecule as a whole (see other paragraphs of this section). The last degree of freedom defines the interatomic distance. Obvious tests are to check that the equilibrium distance and the total energy of the molecule do not depend on i) the orientation of the molecule in space, ii) an atom which is kept fixed. This molecule can be considered as an entirely quantum mechanical or classical system only or as a combined QM-Classical system where one of the atoms is embedded into the potential of the other. These tests have been performed for NaCl and MgO molecules. Results of the tests have been found to be consistent within the required accuracy as discussed below.

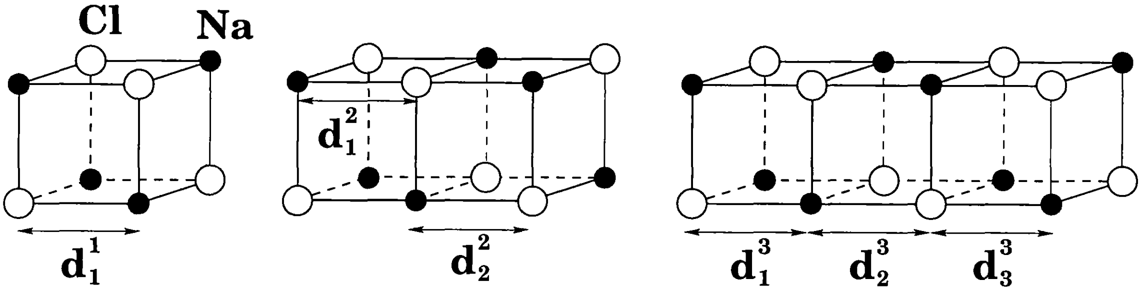

Figure 4: QM clusters used for the perfect lattice test: NaCl.

2.4 Tests of the model

2.4.1 Perfect lattice test: NaCl, $LiBaF_3$

The aim of this test is to check the consistency of the shell model and the *ab initio* description of the crystal. To perform the test, a QM cluster, representing a part of the ideal crystal, is embedded into the rest of the ideal crystal, represented via the shell model. The system's total energy is then minimised with respect to the coordinates of all ions. The test is considered as successful if the ideal lattice remains unperturbed as a result of embedding. The latter can be quantified in terms of i) magnitude of the displacements of the ions from their ideal lattice sites, ii) the change in the total energy of the system in the energy minimisation, and iii) the asymmetry of the adiabatic potential profile for small displacements of the boundary QM atoms in and out of the QM cluster. Two examples of the perfect lattice test are given below.

NaCl crystal. To simplify the analysis we consider only rectangular clusters of the size of 2×2×n ions where n was varied from 2 to 4 as shown in Fig. 4. The shell model parameters for NaCl were taken from reference [26] and slightly modified: i) the cation was taken as unpolarisable and ii) the spring constant for the anion was modified in order to obtain correct dielectric constant of the crystal. This new shell model results in the cation-anion separation equal to 2.778 Å, which is slightly smaller than that for the original shell model (2.789 Å) and about 2% smaller than the experimentally observed separation (2.815 Å). Elastic properties of the crystal and its polarisabilities were reproduced reasonably well. QM clusters have been embedded into a cubic nano-cluster 25×25×25 ions. Ions in region I, both quantum mechanical and classical (cores and shells), have been relaxed. The deviation of the interionic distances inside the QM cluster from those outside is taken as a measure of the mismatch.

The calculated distances between ions inside the embedded and free QM clusters and between ions at the interface of the QM cluster and the classical environment are summarised in Table 1. It is clear that in the case of the embedded cluster the cation-anion separations d_n^m show much smaller variations than those in the case of the free cluster. Also, the former are very close to the shell model anion-cation separation. The magnitude

Table 1: Comparison of interatomic distances in the case of free and embedded QM clusters (see Fig. 4)

Cluster	Relaxation energy, eV			Na^+-Cl^- separation,Å			
				inside QM cluster		at the interface	
	Total	per QM atom		embedded	free	Na^+_{QM}-Cl^-_{Cl}	Na^+_{Cl}-Cl^-_{QM}
Na_4Cl_4	0.222	0.028	d^1_1	2.795	2.711	2.808	2.872
Na_6Cl_6	0.302	0.025	d^2_1	2.789	2.685	2.799 - 2.822	2.863 - 2.871
			d^2_2	2.787	2.741		
Na_8Cl_8	0.386	0.024	d^3_1	2.783	2.735	2.799 - 2.820	2.868 - 2.875
			d^3_2	2.782	2.716		
			d^3_3	2.790	2.693		

of the mismatch at the interface is small for Na^+_{QM}-Cl^-_{Cl} pairs; in this case the cation-anion separation differs from the shell model lattice constant by 1% at most. The mismatch is about 3% for Na^+_{Cl}-Cl^-_{QM} pairs. This, relatively small mismatch can be made smaller by optimising parameters of short-range potentials for classical boundary cations. All in all, results of the perfect lattice test are satisfactory.

$LiBaF_3$ crystal. We also give an example of a perfect lattice test for another, more complex, system, $LiBaF_3$ which also has a cubic structure (see Fig. 3). The QM cluster used for the perfect lattice test is shown in Fig 5(a). The cluster was embedded in a large cubic nano-cluster. Each of the boundary Ba ions of the QM cluster has been represented by an effective core pseudo-potential (ECP) replacing 54 core electrons. The complication stems from the incorrect interaction of the larger core Ba ECP with other atoms of the quantum mechanical cluster (see previous discussion in 2.2.5). This incorrect interaction resulted in un-physically large, up to 1.5 Å, displacements of the Ba ions. Following the ideas outlined in section 2.2.5 a classical repulsion correction term $W = A \exp\left(-\frac{r}{\rho_0}\right)$ was added to the interaction between the Ba and nearest F ions. The parameter A was kept as optimised by Jackson *et al.* in [102] and the parameter ρ_0 was varied to minimise the forces acting on the Ba ions in the smaller QM cluster (Fig. 5(b)). The latter was embedded in the same nano-cluster with all atoms fixed at their lattice sites in the ideal crystal. The perfect lattice test was then repeated for the large QM cluster (Fig 5(a)) with the correction term included into the expression for the total energy and total forces. The displacements of the QM atoms from their ideal lattice sites were less than 0.02 Å (about 0.5% of the lattice constant) which demonstrates the importance of the correction term for atoms with a "large core". An alternative approach - the use of a smaller core or a full-electron calculation - is almost always not-feasible. The results of this test are described in more detail in section 3.2.4.

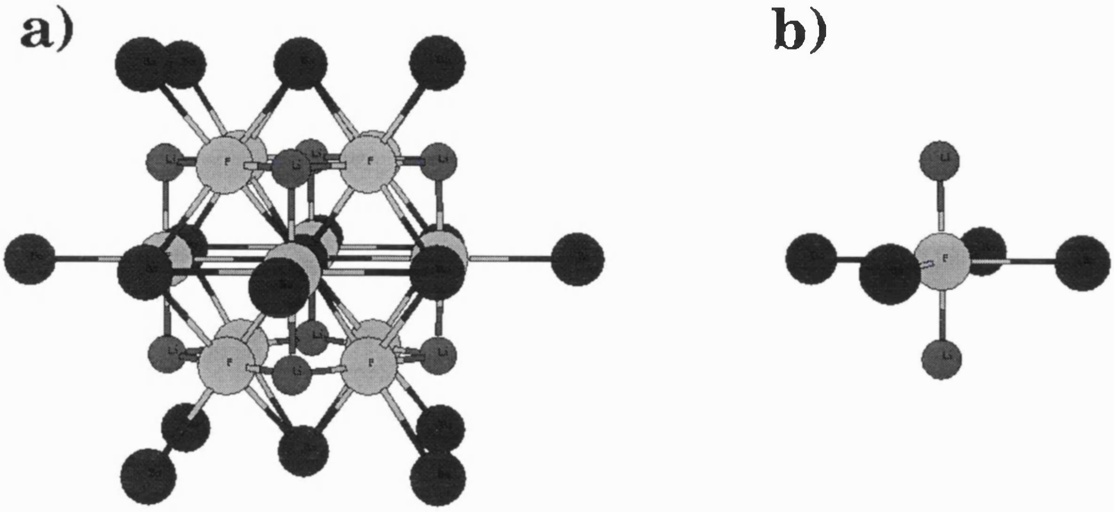

Figure 5: Clusters used for the perfect lattice test: $LiBaF_3$.
a) cluster used for the test; b) cluster used to fit the classical correction to the Ba-F interaction.

2.4.2 Schottky and Frenkel defects in NaCl

The Frenkel and Schottky defects in alkali halides have been studied both theoretically and experimentally for a long time (see, for example, [24] and references therein). At present, these defects hold a considerable interest as examples of well established systems, which may be used for testing new methods.

Details of calculations. The formation energy of the Schottky defect was calculated as a sum of the formation energies of non-interacting anion and cation vacancies less the lattice energy. The lattice energy, 8.0 eV, was taken from purely classical calculations. Similarly, the formation energy of the Frenkel defect was calculated as a sum of the formation energies of infinitely separated vacancy and interstitial defects. The calculations have been done with a spherical nano-cluster containing only 800 atoms. The quantum mechanically treated region included the stoichiometric Na_4Cl_4 cluster where all anions have been additionally coordinated with 12 bare, ECP represented, cations. The restricted HF method and 6-31G basis set were used in the *ab initio* part of the calculation. We stress that the charged vacancies and interstitials strongly polarise the host lattice. This polarisation is taken into account in these calculations.

Results of calculations. The results of the calculations and comparison with previous experimental data and theoretical calculations are summarised in Table 2. Positive and negative signs of the displacement correspond to motion towards and from the defect respectively.

It is seen that formation energy of the Schottky defect is in good agreement with both experimental studies and Mott-Littleton calculations. The same can be said about the cation Frenkel defect formation energy. However, formation energy of the anion Frenkel

Table 2: Schottky and Frenkel defects in the NaCl bulk: formation energies and displacements of ions in vicinity of defects.

Type of the defect	Cation displacement			Anion displacement		
	Å	%	direction	Å	%	direction
Na$^+$ vacancy	-0.110	-3.9	[110]	0.173	6.2	[100]
Cl$^-$ vacancy	0.270	9.7	[100]	-0.098	-3.5	[110]
Na$^+$ interstitial	0.419	15.0	[111]	0.118	4.2	[111]
Cl$^-$ interstitial	0.042	1.5	[111]	0.497	17.8	[111]

Formation energy, eV	This work	Mott-Littleton [24]$^{a)}$		Exp. [173]	Exp. [181]
Schottky	2.47	2.32	2.54	2.58	2.26
Frenkel (cation)	3.59	3.21	3.50	3.32	2.88
Frenkel (anion)	5.97	3.85	4.33	5.48	4.60

$^{a)}$ These energies were calculated using two different sets of interatomic potentials.

defect is somewhat larger than that predicted in previous studies. This is because the anion is much larger than the cation and the repulsive interaction of its electrons with the electrons of the host lattice ions cannot be accurately calculated within Hartree-Fock approach. It is expected that a proper account of the electron correlation, which should be significant in the case of the interstitial defect, would result in a lower formation energy.

As the system relaxes, ions of both the QM cluster and the classical host lattice are displaced from their ideal positions. The direction and magnitude of displacements are in agreement with those, calculated using shell model and are consistent with the calculated characteristics of similar defects in other alkali halides, e.g see calculations on KBr [193] using the ICECAP code.

A natural population analysis of the electron density redistribution suggests that all ionic charges remain essentially unchanged apart from the case of cation interstitial ion where ionic charges of anion decreased by 0.03e due to the charge density flow to the interstitial. In all other cases, the changes of the ionic charges were less than 0.01e which is in accord with the highly ionic character of NaCl.

We conclude that the embedded cluster calculations of both the Schottky and Frenkel defects produce results which are close to those obtained both experimentally and theoretically.

2.4.3 Oxygen vacancies in the bulk of MgO

Optical absorption of the oxygen vacancies, both the neutral F centre and the charged F$^+$ centre, have been extensively studied both experimentally and theoretically. Although, it has long been established that both these centres absorb 4.98 eV and 5.02 eV light respectively [29], [117], [172], [202], we are not aware of any *ab initio* calculations which could reproduce this experimental result. Vail [213], using a very simple embedding scheme and HF method, found absorption and emission energies for the F$^+$ centre to be in extremely good agreement with experiment (4.95 eV and 3.27 eV respectively). But when he im-

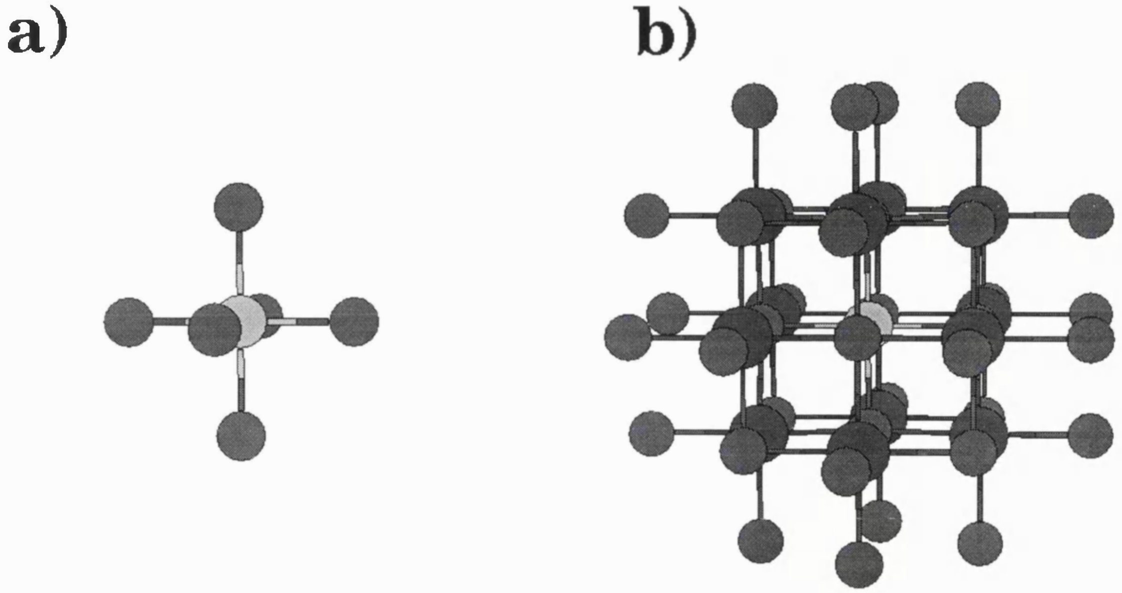

Figure 6: QM clusters used to study oxygen vacancy in bulk MgO.

proved the embedding potential, the agreement with experiment was completely destroyed. In the most recent calculation [196] an advanced MRCI technique has been used to obtain absorption energies of 6.00 eV and 5.75 eV for the bulk F and F^+ centre respectively. We are aiming to check i) how closely we can reproduce the optical absorption energies using available methods and ii) how the nature of the excited state depends on the size of the QM cluster and the flexibility of the basis set.

Details of the calculations. The wave function of the excited state of the F^+ centre is thought to be localised in a relatively small region of space which suggest that it should be well described in cluster model using a QM cluster of moderate size.

QM clusters of two sizes have been used: the small cluster includes the oxygen vacancy surrounded by six nearest cations only (Fig. 6(a)); the large cluster additionally includes twelve anions centred at [110] sites, eight cations at [111] sites and 24 cations at [012] sites (Fig. 6(b)). The QM clusters have been embedded into cubic 20×20×20 ions nano-cluster. The geometry of the system was relaxed at the HF level using a standard 6-31G basis set for all anions and six cations at [100] lattice sites in the case of large cluster; for all other cations an effective core pseudo-potential replacing 1s, 2s and 2p core electrons [216] and a single s-type basis function contracted from two primitive Gaussian s-type functions have been used. A standard 6-31G oxygen basis set was also centred in the oxygen vacancy. The excited states were calculated for the fixed geometry using the CIS method and basis sets as indicated in Tables 4 and 5 below.

Results of calculations. The formation energy of the neutral F centre and the displacements of the host lattice ions in the vicinity of the F, F^+ and F^{2+} centres are shown in the

Table 3: Oxygen vacancies in the bulk MgO: formation energies and displacements of the surrounding lattice ions.

Cluster	Defect	Formation energy, eV	Displacements,Å [a] Mg [100]	O [110]	Mg [111]	Mg 3s occ.[b] α-spin
Mg_6O_1	F	11.053	-0.033	-0.020	-0.001	0.248
$Mg_{38}O_{13}$	F	8.809	0.015	0.008	0.000	0.348
Mg_6O_1	F^+		0.089	-0.058	0.000	0.099
$Mg_{38}O_{13}$	F^+		0.107	-0.031	0.013	0.247
Mg_6O_1	F^{2+}		0.222	-0.101	-0.001	0.000
$Mg_{38}O_{13}$	F^{2+}		0.207	-0.073	0.019	0.174
Other authors						
[182], HF	F	8.651 (9.960)[c]	0.000	0.000		
[113], DFT	F	10.547				
[147], HF	F	8.593				
[182], HF	F^+		0.090	-0.050		
[182], HF	F^{2+}		0.178	-0.113		

[a] Negative values correspond to inwards displacement.

[b] Mg 3s occ. shows occupations of 3s orbitals (in α-spin) of the nearest cations calculated using NPA.

[c] The formation energy including polarisation and correlation corrections.

upper part of Table 3. The lower part of the table contains results of other calculations performed using computer codes and methods as indicated in the table. In general, all the calculations give similar displacements of the lattice ions near the vacancies. The differences between the energies of the neutral F centres can be attributed to the differences in the models, methods of the calculations, and basis sets. For example, the results of references [182] and [147] obtained using the same HF method agree rather well. However, polarisation and correlation corrections produce difference as large as 1.4 eV (corrected energy is given in brackets).

Optical absorption energies corresponding to singlet-singlet transitions of the F and F^+ centres are summarised in Tables 4 and 5 respectively. The oscillator strength of these transitions is also given in these tables. The transition energies for both centres behave similarly as the basis set increases. We discuss this behaviour for the case of the the small cluster first. As the basis set increases, the transition energies and the corresponding oscillator strength tends to decrease: the energies drop by 0.9 eV and 0.8 eV for the F and F^+ centres respectively (from 8.3 eV to 7.4 eV and from 7.3 eV to 6.5 eV) and the oscillator strengths change from 1.06 to 0.84 for the F centre and from 0.37 to 0.34 for the F^+ centre. We note that the slight decrease of the F centre transition oscillator strength indicates that the relative localisation of the ground and excited states tends to change. On the contrary, the almost constant oscillator strength for the F^+ centre transitions suggests that both ground and excited states remain localised in the same region of space. Further extension of the basis set (with one *s* and one *p* basis functions added to the Mg ions at the [100]

Table 4: Excitation energies of F centre in bulk MgO: CIS singlet-singlet transitions.

Site and Basis set									
vacancy and all O			Mg [100]		Mg [111]		Mg [012]	Energies	oscillator
s	p	d	s	p	s	p	s	eV	strengths
Small Cluster (Fig. 6(a))									
6,3,1	3,1		2					8.2753	1.0571
6,3,1,1,1	3,1,1,1		2					7.1048	0.9427
6,3,1,1,1	3,1,1,1	1	2					7.1048	0.9427
6,3,1,1,1	3,1,1,1		2	2				7.3861	0.8376
6,3,1,1,1	3,1,1,1		2,1	2,1				3.6005	0.0491
6,3,1,1,1	3,1,1,1		2,1,1	2,1,1				3.5711	0.0443
6,3,1,1,1	3,1,1,1		2,1,1,1	2,1,1,1				3.4865	0.0496
Large Cluster (Fig. 6(b))									
6,3,1	3,1		2		2		2	7.9701	0.7909
6,3,1,1,1	3,1,1,1		2		2		2	7.4280	0.7258
6,3,1,1,1	3,1,1,1		2,1	2,1	2		2	7.1361	0.7304
6,3,1,1,1	3,1,1,1		2,1	2,1	2,1	2,1	2	4.2737	0.0056

Table 5: Excitation energies of F$^+$ centre in bulk MgO: CIS singlet-singlet transitions.

Site and Basis set									
vacancy and all O			Mg [100]		Mg [111]		Mg [012]	Energies	oscillator
s	p	d	s	p	s	p	s	eV	strengths
Small Cluster (Fig. 6(a))									
6,3,1	3,1		2					7.3109	0.3702
6,3,1,1,1	3,1,1,1		2					6.4107	0.3578
6,3,1,1,1	3,1,1,1	1	2					6.4107	0.3379
6,3,1,1,1	3,1,1,1		2	2				6.4787	0.3379
6,3,1,1,1	3,1,1,1		2,1	2,1				5.1059	0.0320
6,3,1,1,1	3,1,1,1		2,1,1	2,1,1				5.0747	0.0317
6,3,1,1,1	3,1,1,1		2,1,1,1	2,1,1,1				4.9865	0.0336
6,3,1,1,1	3,1,1,1		2,1,1,1	2,1,1,1	0			5.9523	0.0396
6,3,1,1,1	3,1,1,1		2,1,1,1	2,1,1,1	0		0	6.4610	0.0001
Large Cluster (Fig. 6(b))									
6,3,1	3,1		2		2		2	7.5035	0.3428
6,3,1,1,1	3,1,1,1		2		2		2	6.6089	0.3500
6,3,1,1,1	3,1,1,1		2,1	2,1	2		2	6.3631	0.3472
6,3,1,1,1	3,1,1,1		2,1	2,1	2,1	2,1	2	5.6874	0.0114

lattice sites) leads to a dramatic decrease of the transition energies and is accompanied by a decrease of the oscillator strength to almost zero. This indicates that the excited state delocalises outside the QM cluster and, consequently, becomes meaningless. Plots of the density maps for the excited state support this view. The same observation has been made by Vail in reference [213]. In the case of the larger cluster, the behaviour of the transition energies and oscillator strengths is essentially the same. The delocalisation occurs after one s and two p functions have been added to the Mg ions at the [111] lattice sites. These observations suggest that the sudden decrease of the transition energies and oscillator strengths is due to the finite size of the QM cluster: if the extension of the basis set becomes larger than the extension of the QM cluster, the formal CIS solution localises outside the QM cluster.

Based on the results discussed above we can conclude that: i) the higher the localisation of the excited state the better it can be reproduced in the cluster model, ii) the energies and wave functions of excited states are very sensitive to the flexibility of the basis set, iii) the CIS method overestimates the excitation energies by as much as 1.5 eV for the F^+ centre and 2.0 eV for the neutral F centre. We should emphasise that the properties of the excited states strongly depend on the extension of the basis set and the size of the QM cluster: it may happen that calculated transition energy is close to the experimental result but the corresponding wave function of the excited state is delocalised outside the QM cluster and, therefore, is unrealistic.

2.5 Summary

In this Chapter we have formally derived the model for the QM cluster embedded into the polarisable shell model environment from the general expression for the total energy of two interacting sub-systems. Then, the detailed description of the practical realisation of the model was given followed by the description of its tests. Generally, the good performance of the computer code and the agreement of the properties of well known systems with the experimental results and previous calculations suggest that the present realisation of the model can be used to study properties of point defects in ionic crystals. The following Chapters of this Thesis deal with further applications of the model and of the computer code.

3 Properties of defects in the bulk of ionic crystals

A metal ion embedded into an ionic crystal lattice is an example of a typical substitutional defect for these crystals. If the charge of the substitutional ion differs from the charge of a substituted host lattice cation, it may be compensated, for example, by a cation vacancy or an electronic hole localised nearby. A variety of crystal lattices, substitutional ions and possible mechanisms of the charge compensation give rise to a large number of defect centres, which exhibit various properties. The diversity of these defect centres and, consequently, the variety of properties they exhibit substantially increases if substitution of a host lattice cation by a metal ion is accompanied by substitution of one or several nearest host lattice anions by molecular ions, e.g. OH^- or CN^-, or by vacancies with formation of F centres. Defects of this kind have been intensively studied for their fundamental as well as technological importance, (see, for instance, studies of alkaline-earth cations [25] and ions of transition metal elements [13], [169] in alkali halides). Metal cyanide and nitrosyl dopant complexes in silver halide crystals [57], [8], [18], [17] are examples of shallow electron centres and are crucial for the photo-processing. The nature of the electronic-vibrational (E-V) energy transfer process between electronically excited states of a substitutional metal ion and vibrationally excited states of a molecular ion have been also intensively investigated (see [50], [52], [51] and references therein). Finally, optical properties of defect centres and their application to, for example, scintillation materials are topics of numerous experimental and theoretical studies.

In this Chapter we apply our embedded cluster method to study two typical defect centres in the bulk of ionic crystals. In section 3.1 the embedded cluster method is used to determine structural, electronic, and vibrational properties of the $[FeCl_{5-n}(CN)_n]^{3-}$ and $[FeCl_{5-n}(CN)_n]^{4-}$ ions incorporated into the NaCl host lattice. Configurations corresponding to $n = 0$, 1, and 6 have been considered. In section 3.2 we consider a typical scintillation material formed by doping of small concentrations of Ce^{3+} into $LiBaF_3$ and discuss the effect of the model of the host lattice environment on the calculated values of optical transition energies for this material. It is shown that in order to achieve quantitative agreement between the calculated and experimental excitation and luminescence energies, one should properly take into account the lattice polarisation.

3.1 Properties of the iron cyanide ions trapped in NaCl host lattice

3.1.1 Introduction

Metal complex impurities play an important role in photo-processing [73], [74]. In fcc lattices, such as alkali halides, they substitute for the host lattice cation and a few nearest anions and may be described by a general formula $\{[ML_nA_{6-n}]^{m-}\cdot(V_{cat})_{5-m}\}^{5-}$, where M and L stand for the metal ion and its ligands, A is the lattice anion and V_{cat} is cation vacancy, respectively. Cation vacancies are normally present in these systems to compensate an excessive charge of the impurity. Typical examples of these impurity defects are $Co(CN)_6^{3-}$ in NaCl [103] or $[OsCl_5(NO)]^{3-}$ in AgCl [57]. Depending on the preparation, the metal ion may be coordinated by a different number of ligands and charge compensating cation vacancies. The molecular ligands, such as CN^- or NO^-, can have two average orientations. There can be also a significant number of different configurations of the compensating cation vacancies. Therefore the total number of possible structural configurations of a metal complex impurity centre in some cases can reach several hundred. Optical, infrared and Raman spectroscopies as well as magnetic resonance based methods are often used to determine the structure and properties of these systems. However, the interpretation of experimental spectra is not always straightforward and requires the knowledge of defect structural configurations which are likely to be present in significant concentrations. These configurations can be determined theoretically, together with the general trends in optical absorption energies and vibrational frequencies as a function of the defect structural parameters. However, the huge number of possible configurations makes this an immense task for quantum-mechanical methods. How to establish reliable defect models? A way forward could be to use the classical, Mott-Littleton (ML) based methods to determine the relative energies of different structural configurations and then to study their spectroscopic properties. However, can we trust classical calculations in the case of such complex defects? To address this question one needs to have a more accurate, quantum-mechanical method capable of predicting not only the relative stability of different defect structures but also spectroscopic properties.

To address some of these issues, in this paper we discuss the results of our calculations of the $\{[FeCl_{6-n}(CN)_n]^{m-}\cdot (V_{Na^+})_{5-m}\}^{5-}$ impurity complex incorporated into the NaCl crystal lattice. This defect has a range of features characteristic of complex defects mentioned above: molecular ligands, an open d-shell of the 3d metal ion, many configurations of the charge compensating cation vacancies, different charge states. Our approach is to calculate a number of characteristic defect configurations quantum-mechanically using a recently developed embedded cluster method, and to compare the predicted relative energies with the results of the Mott-Littleton (ML) calculations of the same configurations. Then we investigate the dependence of a number of subtle defect properties, such as the orientation of CN^- ligands, and the dependence of vibrational frequencies of the CN stretching mode on this orientation, charge of the impurity, and the relative position of the ligand and the charge compensating vacancies, and compare them with the experimental data. The analysis of these results demonstrates the ability of ML calculations to predict the relative stability of different configurations of this particular family of defects, and gives a more general perspective on this approach. Comparison of the ML and embedded cluster calculations reveals the important contributions to the defect energy and stability. We formulate the criteria of applicability of this approach to similar defects.

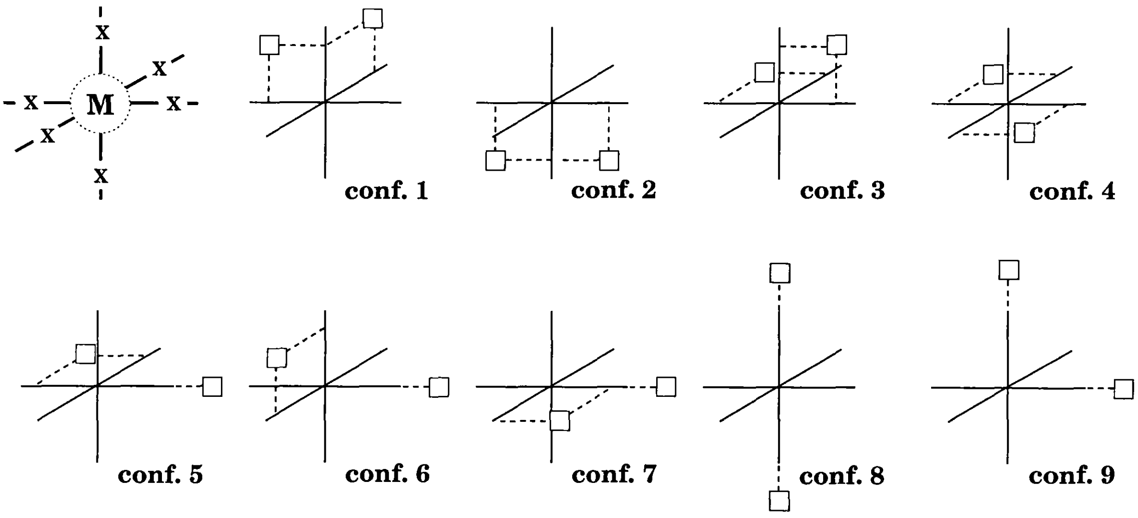

Figure 7: Possible configurations of the two cation vacancies in the vicinity of a $[FeCl_n(CN)_{6-n}]^{3-}$ complex in bulk NaCl.

3.1.2 Experimental and theoretical background

As discussed above, dependent on preparation conditions and temperature, a Fe^{3+} ion substituting for Na^+ ion in the NaCl lattice can be surrounded by different number of CN^- ligands and cation vacancies. The $Fe(CN)_6^{3-}$ ion in NaCl, for example, occupies seven lattice sites with six CN- ions replacing six Cl- ions, so that the octahedral $Fe(CN)_6^{3-}$ ion replaces the $NaCl_6^{5-}$ group in the host lattice. To keep the crystal electrically neutral, the defect is associated with two cation vacancies. The electrostatic considerations suggest that most of the vacancies occupy the nearest (n) or next- nearest (nn) positions to the impurity ion centres. An alternative mechanism of charge compensation could be by Cl^- interstitial ions in the vicinity of the complex. However, as the formation energy of Schottky defects in NaCl is lower than that of Frenkel defects (see [173] or [181]), the charge compensation by the interstitial anions is less probable. Nine possible configuration of the two cation vacancies at the (n) and (nn) sites are shown in Fig. 7.

The $Fe(CN)_6^{3-}$ ion is a typical covalent complex with a d^5 electronic configurations. It has a very large octahedral splitting (about 35000 cm^{-1} [106]) due to the CN^- ligand field. Consequently, it is a low-spin t_{2g}^5 complex (see in Fig. 8). The fact that iron cyanides are diamagnetic in the case of an even number of electrons, as in $Fe(CN)_6^{4-}$ ion and have the magnetic susceptibilities of the order of magnitude corresponding to one free spin, i.e. S=1, as in the case of $Fe(CN)_6^{3-}$ ion, has long been recognised and discussed by Pauling [155] and Van Vleck [215]. The three low-lying t_{2g} orbitals are split by the low symmetry field due to different possible configurations of the charge compensating vacancies. The perturbing influence brought by the vacancies depends on their relative position with respect to the complex.

The paramagnetic $Fe(CN)_6^{3-}$ ion in NaCl and KCl has been studied by Wang *et al.* [218] using EPR and ENDOR at 4.2 K. Another extensive set of experiments was under-

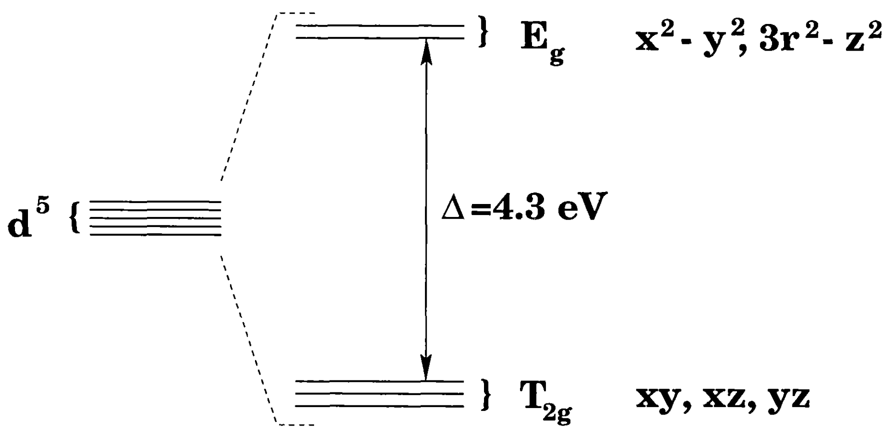

Figure 8: The T_{2g}-E_g splitting of the central Fe^{3+} ion *d*-levels in the octahedral field of its ligands.

taken by Jain *et al.* [103], [104] who have studied the electronic and vibrational spectra of hexacyanides in NaCl and KCl at liquid air temperature (113K). These studies, however, arrived to contradictory conclusions regarding the local atomic structure of the defect centre in NaCl. According to [218] and [217], the most populated centre has the configuration 4 in Fig. 7, and the two other less populated configurations resolved by paramagnetic resonance were assigned to the configurations 3 and 6. On the contrary, the analysis of electronic and vibrational spectra of ferricyanide ions in NaCl reported in [104] suggested that the most probable structure corresponds to the configuration 5. It should be noted that different temperature in these experiments is unlikely to cause such a disagreement in the results. A recent attempt to resolve this contradiction theoretically [8] has been only partly successful. In this embedded cluster study the configurations 4 and 3 were found to have the lowest and the second lowest total energies, while the third lowest defect centre structure corresponded to the configuration 2. Even more surprisingly, it appeared that the apparently unfavourable configuration 1 has a much lower energy than both configurations 5 and 6.

An important conclusion concerning the influence of cation vacancies on the energy of *d*-orbitals was made in ref. [218]. To analyse this effect, the authors classified the positions of the vacancies with respect to the *d*-orbitals. The vacancy at the nearest cation site (the [110] site with respect to the iron ion) occupies either a position in the orbital plane along a lobe direction or a position that is 45° off the orbital plane. If the former position is denoted as a subscript $E_{\bullet}$ and the latter by a superscript $E^{\bullet}$ then the energies of the d_{xy} and d_{xz} orbitals for configuration 4 may be denoted as $E_{\bullet\bullet}$ and $E^{\bullet\bullet}$, respectively. It has been observed that the relations $2(E^{\bullet}_{\bullet}-E_{\bullet\bullet}) = 2(E^{\bullet\bullet}-E^{\bullet}_{\bullet}) = E^{\bullet\bullet}-E_{\bullet\bullet}$ are nearly exactly obeyed in both NaCl and KCl. The deviation is less than 2.5% for NaCl and 0.5% for KCl. These relations demonstrate that the perturbations due to the vacancies are additive. A second interesting feature is that all three values $E^{\bullet\bullet}-E_{\bullet\bullet}$, $E^{\bullet\bullet}-E^{\bullet}_{\bullet}$, $E^{\bullet}_{\bullet}-E_{\bullet\bullet}$ in KCl are between 92% and 94% of those in NaCl. These two percentage values are close to the ratio of the two lattice constants, which is 0.90. Such a good correlation indicates that the

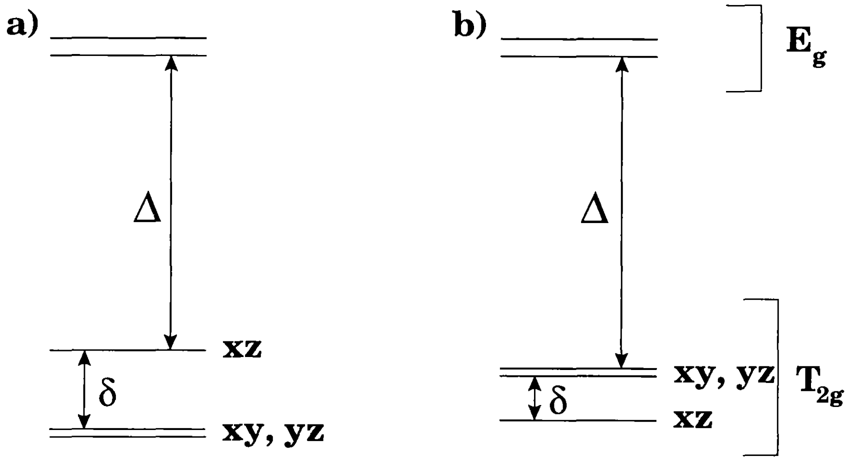

Figure 9: Qualitative splitting of the Fe^{3+} d-levels in the field of ligands and cation vacancies. a) splitting for configuration 3 (see Fig. 7); b) splitting for configuration 6 (see Fig. 7). Δ indicates the T_{2g}-E_g splitting due to the octahedral ligand field; δ indicates the splitting due to low symmetry field of the cation vacancies. Levels corresponding to bonding (alpha) orbitals are considered here. Ordering of the anti-bonding (beta) orbitals of the T_{2g} subspace is the reverse; for example for the configuration 6, the d_{xz} level will be the highest and the corresponding orbital will be unoccupied.

interaction between the Fe^{3+} and the vacancy has predominantly Coulombic character.

The effect of x irradiation on the NaCl and KCl crystal doped with $Fe(CN)_6^{3-}$ ions has also been investigated in [104]. On the basis of the changes in the vibrational spectrum (splitting of the CN stretching mode) with the time of irradiation, it has been suggested that electrons, released by the crystal anions are preferentially captured by Fe^{3+} and Fe^{2+} ions, which are converted to Fe^{2+} and Fe^{+} respectively. The change in the valence state of Fe^{3+} to Fe^{2+} and Fe^{+} results in the formation of $Fe(CN)_6^{4-}$ and $Fe(CN)_6^{5-}$ respectively. For longer irradiation times, additional lines appeared, which were due to some unidentified species.

We are aiming to calculate the relative stability of different defect configurations and to investigate the nature of the interactions within the defect complex.

3.1.3 Details of calculations

The cubic nano-cluster, used to model the bulk of the NaCl included 25×25×25 ionic centres. Formal ionic charges have been used for all fully coordinated ions; charges of ions at the surface, edge and corner sites of the nano-cluster have been chosen as $\frac{1}{2}$, $\frac{1}{4}$, and $\frac{1}{8}$ of their formal values respectively. A spherical region I of the radius of 16.7 Å, containing more than 900 atoms, was situated at the centre of the nano-cluster. Most of the calculations were performed using the QM cluster which is equivalent to the $Na_{19}Cl_6$ cluster of the host crystal (see Fig. 10(a)). One or several anions of this cluster have then been replaced by CN ligands (Fig. 10(b)). Due to technical limitations we consider defects with only 0, 1, and 6 CN^- ligands. In all cases, a full electron basis set was used for the central cation and its six ligands, while other cations have been described

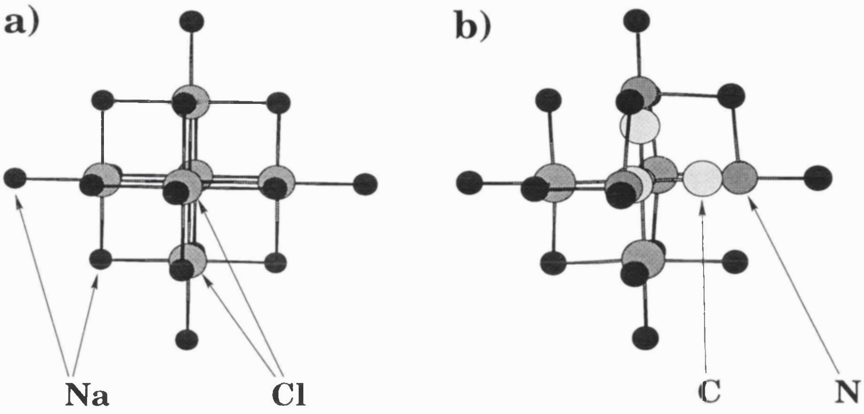

Figure 10: Clusters used in the study of iron cyanides.
a) the cluster used to represent a fragments of defect free bulk NaCl; b) a cluster representing $[FeCl_3(CN)_3]^{3-}$ centre corresponding to configuration 4 in Fig. 7.

using an Effective Core Pseudo-potential [216] and one s-type basis function. To check the dependence of the results on the quality of the basis set, in several cases we have employed several full electron basis sets listed in Table 6. The B3LYP density functional has been employed in all calculations. The electronic structure of ions with closed electronic shells, for example $[FeCl_6]^{4-}$ in NaCl, with T_{2g} orbitals of the Fe^{2+} ion completely filled and E_g orbitals - empty, can, in principle, be studied using the HF method. However, in the present study, HF calculations of the $[FeCl_6]^{4-}$ complex in NaCl resulted in an incorrect electronic structure, in which E_g orbitals rather than T_{2g} orbitals were populated. We do not therefore discuss the HF results in any detail.

It is important to emphasise the difference between the present calculations and an earlier study [8]. Both calculations have been performed using similar embedded cluster approaches and comparable clusters and basis sets. The methods differ in the calculation of the total energy and the geometry optimisation procedure. In [8] a two step calculation of the total energy is used: i) atoms of only the QM cluster are relaxed quantum mechanically and then fixed, ii) atoms of the classical environment are relaxed classically and the corresponding polarisation correction is added to the total energy. This approach effectively divides the space of all atomic coordinates into two sub-spaces and therefore hampers the complete geometry relaxations and also does not account for the effect of the host lattice relaxation on the electronic structure of the QM cluster. These shortcomings are removed in the present scheme, where we calculated the total force acting on each atom and the atoms of the QM cluster and of the environment are relaxed simultaneously.

3.1.4 Results of calculations

Relative energies of defect configurations. Fe^{3+} ions in NaCl can trap electrons creating stable closed shell centres, such as $Fe(CN)_6^{4-}$, which require only one cation

Table 6: Basis sets used in the present study of iron cyanides.

Basis	Fe	C, N	Cl
A	6-31G	6-31G	6-31G
B	6-311G	6-311G	6-311G
C	6-311G	6-311G*	6-311G
D	6-311G	6-311G*	6-311G

vacancy for the charge compensation. Study of these simpler centres allows us to get some initial insight into the interplay between the metal, ligand and vacancy interactions in the crystalline matrix. The results of the calculations of the $[FeCl_6]^{4-}$, $[FeCl_5(CN)]^{4-}$, and $[Fe(CN)_6]^{4-}$ ions compensated by one cation vacancy are summarised in Tables 7 and 8. They present the relative energies of different configurations of the complex with vacancies at the nearest (n) and next-nearest (nn) neighbour sites. These results allow us to make the following conclusions. i) If there is no CN^- ligand present, the vacancy occupies a (nn) site. Even though the electrostatic interaction of the negative vacancy with the positive ion is larger if the vacancy is at the (n) site, this is compensated by a larger repulsive interaction of the vacancy at the (n) site with electrons of the t_{2g} orbitals and a larger lattice polarisation energy for the vacancy at the (nn) site. ii) If the CN^- ligand is present, its size plays an important role in the local structure of the complex. In the case when the ligand is between the Fe^{2+} ion and the vacancy, a negatively charged N atom is closer to the vacancy site than the Cl^- ion in the case of $[FeCl_6]^{4-}$, consequently, the repulsive vacancy-ligand interaction is much stronger. In addition, the Fe-CN distance is smaller than the Fe-Cl distance in $[FeCl_6]^{4-}$, which leads to an additional energy increase according to the Pauli repulsion. iii) For the case where all six Cl^- ions are replaced by CN^- ligands, the relative energy for the vacancy to occupy (n) site becomes only slightly larger than in the case of one ligand. iv) Flipping of the CN^- ligand so that its "N end" is oriented towards the central Fe ion has no effect on the (n) vs (nn) relative stability. v) Finally, the relative energies are almost independent of the basis set although the total energies (not reported here) change significantly.

It is well established that the CN^- ligand is oriented by its "C end" towards the metal ion. However, one cannot exclude a possibility that the ligand may flip due to thermal fluctuations or the interaction of the crystal with light. One may draw an analogy with the OH^- molecular ion in alkali halides, which has a large reorientation rate even at low (10 K) temperatures [85], [118]. Two factors regulate the ability of the ligand to flip: i) the character of the metal-ligand bond, and ii) the size of the ligand as compared to the lattice constant. It is common for the ligand to be bonded to the rest of the complex via π-bonds. The energy, required to break these bonds, is relatively small. Moreover, the CN^- molecular ion is small (the C-N distance varies in our calculations in the range 1.16-1.18 Å) as compared to the inter-ionic distance in the NaCl lattice (about 2.8 Å). The calculated relative energies of the Fe-CN and Fe-NC configurations are given in Table 8.

Table 7: Relative energies (eV) of local structures with the cation vacancy at the $\langle 200\rangle$ site with respect to that at the $\langle 110\rangle$ site for several metal complexes.
Negative sign corresponds to the configuration with the cation vacancy at the $\langle 200\rangle$ site being more stable than that at the $\langle 110\rangle$ site.

Basis	$[FeCl_6]^{4-}$		$^{a)}[FeCl_5(CN)]^{4-}$		$[Fe(CN)_6]^{4-}$	
	HF	DFT	Fe-CN	Fe-NC	Fe-CN	Fe-NC
A	2.93	-1.02	0.37	0.37	0.55	0.56
B	3.15	-1.22	0.33	0.29	0.52	0.47
C			0.26	0.24		
D			0.27	0.25		

$^{a)}$ In this configuration the CN^- ligand occupied the $\langle 100\rangle$ lattice site, which corresponds to the smallest possible distance between the ligand and the vacancy. It is expected that for configurations with larger ligand-vacancy distances, e.g. with the vacancy at the $\langle \bar{2}00\rangle$ site and $\langle \bar{1}\bar{1}0\rangle$ site respectively, the vacancy is more likely to occupy the (nn) site rather than (n) site.

Table 8: Relative energies (eV) of configurations corresponding to different orientations of the CN^- ligand.
X corresponds to the CN^- ligand at $\langle 100\rangle$ site to be in Fe-CN or Fe-NC orientations. The Fe-CN orientation is energetically more favourable.

Basis set	$[FeCl_5(X)]^{4-}$		$[Fe(CN)_5(X)]^{4-}$	
	Vac_{Na^+} at $\langle 110\rangle$	Vac_{Na^+} at $\langle 200\rangle$	Vac_{Na^+} at $\langle 110\rangle$	Vac_{Na^+} at $\langle 200\rangle$
A	0.56	0.57	0.60	0.61
B	0.53	0.49	0.58	0.52
C	0.60	0.57		
D	0.60	0.58		

The results of our calculations confirm that the Fe-CN orientation of the ligands is more favourable independent on the position of the vacancy and the basis set.

Finally, we present the relative energies of the nine non-equivalent configurations of the $[Fe(CN\ )_6]^{3-}$ ion compensated by two cation vacancies. This issue has been previously addressed by us in reference [206]. The results of our new calculations are summarised in Table 9. The first column in Table 9 refers to the number of configuration shown in Fig. 7. The relative energies in the second and third columns were calculated using the embedded cluster approach. These energies can be directly compared to the results of previous embedded cluster calculations [8]. The difference between these two approaches was discussed above. The energies presented in the fourth column were calculated using the Mott-Littleton approach using the parameters from ref. [8]. The meaning of the values presented in the fifth column is explained later. Finally, the two last columns present the results of experimental studies which were discussed in section 3.1.2.

Comparison of the different theoretical and experimental results allows us to make the following observations: i) all theoretical calculations produce the same ordering of the stability, with the exception only of the Mott-Littleton calculation which found configuration 3 to be more stable than configuration 4; ii) the relative energies calculated using basis

Table 9: Relative energies (eV) of the nine non-equivalent configurations of the $[\mathrm{Fe(CN)_6}]^{3-}$ in NaCl.
See Fig. 7 for keys for configurations. The energies are calculated with respect to the most stable configuration 4.

Config.	This work Basis A	Basis B	Mott-Littleton	$^{a)}$Estimate	Other calc. [8]	Experiment [104]	[218]
1	0.323	0.326	0.236	1.833	0.339		
2	0.185	0.180	0.148	0.759	0.298		
3	0.051	0.052	-0.024	0.284	0.061		II
4	0.000	0.000	0.000	0.000	0.000		I
5	0.644	0.621	0.253	3.028	0.370	*	
6	0.728	0.710	0.302	3.505	0.438		III
7	0.973		0.486	5.054	0.640		
8	1.284		0.568	5.905	0.750		
9	1.362		0.581	6.442	0.790		

$^{a)}$ The energies have been calculated for the Coulomb interaction of the two vacancies with the Fe^{3+} ion and with each other. See text for more details.

sets A and B are almost identical. iii) the embedded cluster calculations with the complete account of the lattice polarisation and the reaction field performed in this study and the earlier less accurate calculation [8] predict very close values for the relative energies of defect configurations. In other words, the details of the defect electronic structure missed in the Mott-Littleton calculation, and the effect of the reaction field on the wave function missed in ref. [8], are not essential for identifying the most stable configuration.

The present calculation supports the conclusion made in [218] that the most stable atomic structure of the $\mathrm{Fe(CN)_6^{3-}}$ corresponds to configuration 4 and the second most stable to configuration 3. The same conclusion has been reached in [8]. The local atomic structure of the most stable configuration obtained in reference [8] and in the present study agrees with that obtained using the ENDOR [218]. It is somewhat unexpected that configuration 1, which was ruled out in both experimental studies, is more stable than the predicted configurations 5 and 6. To understand this finding, we estimated the energies of the configurations taking into account only electrostatic interaction of the vacancies and the Fe^{3+} ion. The vacancies were represented by negative point charges $Q_{vac} = -1$; the Fe^{3+} ion was represented by a positive point charge $Q_{Fe} = +3$. All charges were fixed at the corresponding ideal lattice sites. The calculated energies (all energies have been shifted to obtain the relative values) are presented in the fifth column in Table 9. It may be seen that the relative energy of configuration 1 is smaller than those of configurations 5 or 6 and, therefore, it should have been considered in the interpretation of the experimental results. The second factor, which could mislead the interpretation of the EPR experiments made in [218] is the assumption that the complex with vacancies remains octahedral, while deviation from this symmetry has been observed in the calculation.

Finally, the choice between centres of the D_{2h} and C_s symmetries, i.e. between con-

Table 10: Comparison of the calculated and experimental values of the splitting of the t_{2g} orbitals due to cation vacancies.
See section 3.1.2 for the key to the energies.

Centre [218]	Config. Fig. 7	Splitted t_{2g} states	Splitting, cm^{-1} [218]	 This work	Relation (see text)
I	4	d_{xy} - d_{yz},d_{zx}	403.2	4401.3	$E^{\bullet\bullet} - E_{\bullet\bullet}$
II	3	d_{xy},d_{yz} - d_{zx}	194.4	1494.5	$E^{\bullet}_{\bullet} - E_{\bullet\bullet}$
III	6	d_{xy} - d_{yz},d_{zx}	63.0	609.8	

figurations 4 and 5 respectively, was made [104] on the basis of i) the relatively small magnitude of the splitting of the CN stretching mode (ν_6) and ii) the presence of the additional Raman active modes (ν_1 and ν_3), which are inactive in the case of D_{2h} but become active in the case of lower symmetry. In fact, both of these observations may be interpreted in a different way. Indeed, if the cation vacancy is at the (nn) site, i.e. along the Fe-CN axis, its negative charge "pushes" the CN^- ligand towards the Fe^{3+} ion, which is likely to affect the vibrational energy of the stretching mode more than if the vacancy was at (n) site. Therefore, the relatively small magnitude of the stretching mode splitting should support the view that D_{2h} symmetry of the complex is more favourable. The presence of the modes ν_1 and ν_3, which are much less intense than the CN stretching mode, could be due to other configurations present in small concentrations. For example, these modes become Raman active if the symmetry of the complex is C_2, which corresponds to configuration 3. We should note that apart from ENDOR, experimental techniques used in [104] and [218] do not provide direct structural information and have to be confirmed by other studies.

Perturbation of the $\mathbf{T}_{2g}$ states due to cation vacancies. In their EPR study Wang *et al.* [218] have obtained valuable information regarding the splitting of the t_{2g} states due to the low-symmetry field of the cation vacancies (see the diagram in Fig. 9). The results of their analysis are compared with the splitting of t_{2g} states calculated using the NPA procedure in Table 10. We note that the calculated values of the splitting are about order of magnitude larger than those obtained from the experiment. This is partly due to underestimated lattice constant and partly due to intrinsic features of the NPA analysis. It is, however, encouraging that the calculated values show the same trend as those obtained from the experiment. This suggests that the relative effect of the cation vacancies on the electronic structure of the iron ion is correctly reproduced. We also note that the relations $2(E^{\bullet}_{\bullet} - E_{\bullet\bullet}) = E^{\bullet\bullet} - E_{\bullet\bullet}$ for the centres I and II (configurations 4 and 3 respectively) are obeyed with less accuracy than it was found in the experimental study. In our calculations the deviation is more than 30%.

Table 11: Electron affinities of the iron cyanides.

	Electron affinity, eV	Comments
$Fe(CN)_6^{3-}$	4.7	config. 4
$Fe(CN)_6^{3-}$	4.1	config. 4; frozen environment
$Fe(CN)_6^{3-}$	4.6	config. 3
$Fe(CN)_6^{4-}$	0.5	vacancy at ⟨110⟩

Electron affinities of the defect centres. $Fe(CN)_6^{3-}$ and $Fe(CN)_6^{4-}$ centres are often considered as prototypes for more complex systems having a potential value for photographic industry. One of the major characteristics of these systems is their ability to trap photo-electrons.[5] In this paragraph we report the calculation of electron affinities of the iron cyanides (see Table 11).

The results of our calculations suggest that the ferricyanide ion has a very large electron affinity (EA). This is due to its empty state which appears in the band gap of NaCl. The EA calculated with the frozen cluster environment is underestimated by more than 0.5 eV. This is consistent with our previous results (see Chapter 4) that neglect of the polarisation of the host lattice leads to underestimated electron affinities. The ferrocyanide ion ($Fe(CN)_6^{4-}$) has all its T_{2g} orbitals occupied and its E_g orbitals, although still in the band gap, lie close to the bottom of the conduction band. This makes the EA of the $Fe(CN)_6^{4-}$ centre relatively small, and in our study it is only 0.5 eV. We should note that neglect of the host lattice polarisation may result in a negative EA for the $Fe(CN)_6^{4-}$ centre. Overall, the calculated electron affinities are consistent with experimentally observed trapping of electrons by the $Fe(CN)_6^{3-}$ and $Fe(CN)_6^{4-}$ impurities in NaCl under x irradiation. It is, however, important to stress that neither conduction band nor valence band states were present in our calculations, which introduces some uncertainty in the positions of the *d*-levels in the band gap and, consequently, in values on the electron affinities.

Effect of the atomic structure on the C-N stretching mode. The experimental studies show that the C-N stretching mode is very sensitive to the atomic and electronic structures of its local environment. We have already mentioned the study of the vibrational spectra of NaCl and KCl crystals doped with iron hexacyanides reported by Jain *et al.* in references [103] and [104]. Before that, an extensive study of the C-N stretching fundamentals for $[Fe(CN)_6]^{3-}$ and $[Fe(CN)_6]^{4-}$ complexes in several alkali halide hosts has been made by Duncan and Percival [56]. Their study revealed that i) the C-N stretching in alkali halides has a multiplet structure, and ii) the C-N stretching frequencies for the $[Fe(CN)_6]^{3-}$ ion in NaCl are about 70 cm^{-1} larger that those for the $[Fe(CN)_6]^{4-}$ ion. In the present study we checked whether our calculations can reproduce the shift of the vibrational frequencies with increase of the iron oxidation number, and whether flipping

---

[5] We do not describe the process of image formation in this work. Relevant details may be found, e.g. in reference [200].

Table 12: Frequencies of C-N stretching vibrations for several iron cyanides.

Ion	Configuration	C-N stretching, cm^{-1}
$[Fe(CN)_6]^{4-}$	$(CN)_5$-Fe-CN	2117.3
$[Fe(CN)_6]^{4-}$	$(CN)_5$-Fe-NC	2153.1
$[Fe(CN)_6]^{3-}$	configuration 4 in Fig. 7	2178.8

of the CN^- ion affects its vibrational frequency.

The C-N stretching frequencies were calculated for three systems shown in Table 12 for one of the CN^- ions of the complex. The results of our calculations support the view that the CN stretching for the $[Fe(CN)_6]^{3-}$ ion has higher frequency than for $[Fe(CN)_6]^{4-}$ ion. This is due to the stronger electrostatic interaction of the positive central ion with its negatively charged ligands. The magnitude of the frequency shift is close to the experimentally observed value of 70 cm^{-1}. However, this agreement is qualitative because the complete multiplet structure of the CN stretching mode was not calculated. It also follows from the data presented in Table 12 that the flipping of the CN^- molecular ion should be associated with appreciable frequency shift, which may well be observed using existing experimental methods. This shift is expected to be larger for the $[Fe(CN)_6]^{3-}$ ion.

3.1.5 Summary

To summarise, our calculations suggest that the order of the relative energies of different configurations of the $[Fe(CN)_6]^{3-}$ ion associated with two cation vacancies is largely determined by the electrostatic interaction of ions composing the system and the lattice polarisation. The simple Mott-Littleton approach can be used to identify the most stable configurations providing suitable parameters for the classical interatomic potentials are found. It is expected that the same approach may be used to identify the most stable configurations of other similar complexes provided that electronic structure of these complexes does not undergo drastic modifications with the change of the atomic structure of their surrounding. The most stable and the second most stable configurations of the $Fe(CN)_6^{3-}$ complex calculated in this work correspond to configurations 4 and 3 in Fig. 7. This is in agreement with results of earlier EPR experiments and previous theoretical study. Our calculations suggest that the interaction of the complex with the cation vacancies is mainly electrostatic. Electron affinities of the $Fe(CN)_6^{3-}$ and $Fe(CN)_6^{4-}$ centres were calculated to be about 4.6 eV and 0.5 eV respectively. These values are consistent with the experimentally observed conversion of the $Fe(CN)_6^{3-}$ and $Fe(CN)_6^{4-}$ ions to the $Fe(CN)_6^{4-}$ and $Fe(CN)_6^{5-}$ ions respectively under x-irradiation of the NaCl crystal doped with iron cyanides. It was shown that the dependence of the CN^- ion stretching frequency on its local environment in correctly reproduced in our calculations. We also predict that the flipping of the CN^- ligand will be associated with a shift of its stretching frequency by about 35 cm^{-1} to higher energies.

3.2 Effect of the embedded cluster model on optical properties of Ce^{3+} doped $LiBaF_3$

3.2.1 Introduction

In the present section we continue to investigate how the accuracy of the embedded cluster calculations depends on the model of the cluster environment. A strategy, which we adopt in this study, is to calculate a range of physical properties of a localised defect centre employing several models for the environment (polarisable, partly polarisable, and unpolarisable) in otherwise identical embedded cluster models. This strategy was applied to a system which represents a methodological interest for scintillator research: crystalline $LiBaF_3$ doped with small amount of Ce^{3+} ions. The optical properties of the $LiBaF_3$:Ce^{3+} system are well characterised experimentally, which provides an opportunity to compare the results of the different theoretical models against the experimental data. We demonstrate that the local atomic structure of the defect centre, its spectroscopic properties, in particular its luminescence energy, and, consequently, Stokes shift are reproduced incorrectly if the relaxation of the rest of the crystal is neglected.

The remaining sections of this part cover relevant experimental and theoretical studies of the $LiBaF_3$:Ce^{3+} system (section 3.2.2), the details of the present embedded cluster calculations (section 3.2.3), and results of these calculations and general discussion (section 3.2.4). The results of our studies are summarised in section 3.2.5.

3.2.2 Experimental and theoretical background

Combes *et al.* [37] have recently undertaken an experimental study of the spectroscopic properties of $LiBaF_3$ doped with Ce^{3+}. They found that after doping the crystal with the Ce^{3+} ions, the absorption and luminescence spectra exhibit additional features as compared to spectra of the original crystal. i) Four distinctive bands at 204 nm, 218 nm, 240 nm and 250 nm appear in the optical absorption spectrum.[6] These bands were attributed to $4f \rightarrow 5d$ transitions of the Ce^{3+} ions. ii) A broad luminescence band appears between 300 and 400 nm (4.14 and 3.10 eV respectively). These experimental results reveal two remarkable features of the doped crystal. Firstly, the set of Ce^{3+} $4f \rightarrow 5d$ transitions is fourfold, which is noteworthy because the cubic structure of $LiBaF_3$ should result in a twofold splitting. Secondly, $LiBaF_3$:Ce^{3+} shows a Stokes shift of approximately 9000 cm^{-1} (about 1.09 eV) between the absorption band at 250 nm and the maximum of emission band at 320 nm, which is unusually large compared, for example, to the 2000 cm^{-1} Stokes shift in the BaF_2:Ce^{3+} system. The results of recent theoretical studies [6], [136], which aimed to understand these properties of $LiBaF_3$ doped with Ce^{3+} are briefly discussed below.

When Ce^{3+} is incorporated in the $LiBaF_3$ ($LiBaF_3$ unit cell is shown in Fig. 3 on page 46), it may occupy either the Ba or Li site. In any case, the excessive positive charge, +1 or

---

[6] These energies are converted to electron volts in Table 18 on page 76.

+2 respectively, has to be compensated. As with the case of the $Fe(CN)_6^{3-}$ impurity in the bulk NaCl, a variety of charge compensating mechanisms is available including vacancies or substitutional defects of the host lattice ions. In a recent study by Andriessen *et al.* [6], an embedded cluster approach at the Hartree-Fock level was used to investigate possible local defect structures. These authors assumed that the Ce^{3+} occupies a Ba lattice site and considered several associated charge compensating defects: i) substitutional O^{2-} ion at the nearest F site, ii) interstitial F^- ion, iii) vacancy at a nearest Li site, iv) substitutional Li^+ at a nearest Ba site. The two other investigated structures were: v) a Ba vacancy compensating for two Ce^{3+} substitutions at Ba sites and vi) Ce^{3+} on a Li site compensated by a vacancy at a Ba site. The splitting of the $5d$ levels for all the structures studied was calculated using one-electron energies and then analysed and compared with experimental data. The results of this analysis led Andriessen *et al.* to conclude that the most likely structure of the $LiBaF_3$:Ce^{3+} luminescence centre consists of the Ce^{3+} ion at a Ba site and the Li^+ substitutional ion at the nearest Ba site. This conclusion, however, was equivocal since the reliability of methods used in [6] was considered to be unsatisfactory. The Stokes shift calculated in [6] was underestimated by a factor of five.

Another study by Marsman *et al.* [136] attempted to make a more accurate calculation of the lattice relaxation, absorption spectra and the Stokes shift for several structures of the $LiBaF_3$:Ce^{3+} luminescence centre. These authors have employed an embedded cluster and periodic calculations using HF and plane-wave DFT methods respectively. A super-cell consisting of 3×3×3 $LiBaF_3$ unit cells and containing a single Ce^{3+} ion and an associated charge compensating defect, which was used in the periodic calculations, allowed the authors to account for the lattice relaxation more accurately than in [6]. Comparison of the calculated splitting of the $5d$ levels and the experimental absorption energies supported the view that the luminescence centre consists of the Ce^{3+} at a Ba site compensated by a substitutional Li^+ at a neighbouring Ba site. The calculated value of the Stokes shift of 0.61 eV was much closer to the experimental result but still almost two times smaller than observed. Marsman *et al.* suggested that the inaccuracy of their calculations is due to the small size of the super-cell. In particular they noted that: i) the relaxation of the defect atomic structure was constrained within the super-cell; ii) the defect centre has a large dipole moment and therefore it interacts strongly with its images in other super-cells; iii) the polarisation of the host lattice is included only within the super-cell. In the present study we repeat the calculation of the lattice relaxation and of the optical properties for the $LiBaF_3$:Ce^{3+} luminescence centre using our embedded cluster approach, which is free of the above drawbacks.

3.2.3 Details of calculations

Model for defect calculations. The calculations were carried out using our embedded cluster approach (Chapter 2) and a finite nano-cluster model. A methodology for generation of the nano-cluster for $LiBaF_3$ crystal was discussed above (see Chapter 2, section

Table 13: Basis sets used in the study of $LiBaF_3$:Ce^{3+} optical properties.

Ion	Basis functions				ECP$^{a)}$	Reference
	S	P	D	F		
Ba	3,4,1	3,2,1			[Kr]d^{10} (46)	[92]
Ce	3,1,1,1	3,1,1,1	2,1	7	[Kr]d^{10} (46)	[199], [40]
F	4,3	4,1,1			-	[96]
Li	6,1,1				-	[96]
Ba$^{b)}$	3				[Xe] (54)	[216]

$^{a)}$Core size and the number of core electrons replaced by an ECP are shown.
$^{b)}$Basis for Ba ions at the QM cluster boundary.

2.1). To preserve the symmetry of the crystal, we have used a cubic nano-cluster with the cube edge close to 52 Å and with its centre at the Ba site. A spherical region I with a radius of 14.0 Å was centred at the same Ba site and included 843 ions. The calculations were based on a QM cluster shown in Fig. 5 on page 51. The cluster has a sphere-like shape and includes several shells of ions: i) the central Ba ion; ii) twelve F ions at the distance ≈2.8 Å from the centre; iii) eight Li ions at ≈3.5 Å from the centre; and iv) two shells of boundary Ba ions at ≈4.0 Å and ≈5.6 Å from the centre. In the defect calculations, the central Ba ion was replaced by the Ce^{3+} ion. Consequently, the boundary Ba ion in the $\langle 001 \rangle$ direction was substituted by Li^+ ion to satisfy the condition of charge neutrality.

In order to investigate the effect of polarisation of cluster surrounding on local atomic structure of the defect centre, we consider the magnitude of the atomic displacements as a function of the size of region I, i.e. of the region, in which both quantum mechanical and classical ions are allowed to relax. Three models for region I were considered. The first, denoted as A, corresponds to a completely polarisable lattice, the region that has been described in section 3.2.3. In model C, all classical ions of the environment were fixed at their ideal sites and their electronic polarisation has been neglected. In addition, all boundary Ba ions of the QM cluster were fixed. This corresponds to a commonly used model for an embedded cluster calculations in which all centres of the environment and all boundary atoms of a QM cluster are kept fixed and only inner part of the cluster is relaxed [67], [100], [140]. Model B is an intermediate between models A and C. In this model all atoms of the QM cluster, including boundary Ba ions, are relaxed but ionic and electronic contributions to the polarisation of the environment are neglected in a similar way to model C. It should be stressed that although the Li^+ ion at the $\langle 001 \rangle$ Ba site formally belongs to the shell of boundary Ba ions, it was relaxed in the model C. Relaxation of this ion is so large that fixing it at the ideal crystalline position of the replaced Ba ion would obviously result in an incorrect atomic structure.

Following our previous discussion regarding the choice of the basis set, we employ an all-electron basis set for F and Li ions inside the QM cluster and use only one s basis function contracted from three primitive s function at the boundary Ba ions. Only valence electrons of the central Ba and Ce ions were included in the calculations; their core electrons were replaced by an effective core pseudo-potential. Other relevant details are summarised in Table 13. All quantum mechanical calculations were performed at the HF level. Interatomic potentials developed by Jackson *et al.* in [102] were used for classical calculations.

It is a well known problem that large core pseudopotentials may not be suitable for describing the interaction of atoms in molecules. If there are no nd or $(n+1)s$ electrons formally present, e.g. K^+ in KF or Ca^{2+} in CaO, the electrons and nucleus of the other atom begin to penetrate the charge cloud of the ns and np shell and, consequently, interaction of atomic cores can no longer be described by simple expression $V_{core-core} = Z_A^{eff} Z_B^{eff} / R_{AB}$ [92]. Boundary Ba ions in our QM cluster are examples of atoms for which the above expression for the core-core interaction with nearby QM fluoride ions does not work. We have introduced the correction to the Ba-F interaction in the form of a Born-Mayer potential $W = A \exp^{-r/r_0}$ as discussed in Chapter 2, section 2.2.5. The parameters A and r_0 of this correction term have been fitted using a smaller cluster (see Fig 5 on page 51) as described in section 2.4.1 on page 49. This correction term has been present in all our calculations for all pairs of boundary Ba and quantum mechanical F ions.

The energies of the $4d \rightarrow 5d$ optical transitions were calculated using a ΔSCF approach, in which the energy of an excited state was calculated using an approximation of a single determinant wave function constructed from a ground state determinant by substitution of the occupied $4f$ orbital by one of the unoccupied $5d$ orbitals and subsequent relaxation of the electronic structure.

3.2.4 Results and discussion

Perfect lattice test. The total displacements of the ions from their ideal positions corresponding to the lattice constant $a_0 = 3.988$ Å [141] are given in Table 14. In this Table we indicate the absolute magnitudes of the displacements and their magnitudes relative to the lattice constant for each type of symmetry equivalent ions. The number of equivalent ions and their site position with respect to the central Ba ion are also shown. All ions displace symmetrically with respect to the centre of the cluster. The adiabatic potential (not reported here) calculated for small displacements of a boundary Ba ions in and out of the QM cluster along the $\langle 110 \rangle$ axis is almost symmetrical. The small magnitude of the displacements, the negligible deviation of the displacements for equivalent ions, and the symmetrical potential well for the boundary ions suggest that the quantum mechanically and classically treated regions of the system are well balanced.

Relaxation of the defect ground state ($4f$). Local atomic structures of the Ce^{3+} defect centre were calculated for the three models of the polarisable region I. Differences in the atomic coordinates of atoms for the relaxed systems are summarised in Table 15. The largest difference between fully polarisable environment (model A) and partially po-

Table 14: Perfect lattice test for $LiBaF_3$ crystal. Displacements of QM ions from their ideal positions.

Type and number equivalent ions		Site	Displacements Å	% of a_0
F	12	$\langle \frac{1}{2}\frac{1}{2}0 \rangle$	0.018 - 0.019	0.5
Li	8	$\langle \frac{1}{2}\frac{1}{2}\frac{1}{2} \rangle$	0.014 - 0.015	0.4
Ba	6	$\langle 100 \rangle$	0.004	0.1
Ba	12	$\langle 110 \rangle$	0.000 - 0.001	0.0

Table 15: Difference in local atomic structures of the Ce^{3+} dopant in the defect ground state ($4f$).

Type and number of equivalent ions		Site	Differences in atomic coordinates,Å Models A-B	 Models A-C	 Models B-C
Ce	1	$\langle 000 \rangle$	0.008	0.020	0.012
Li	4	$\langle \frac{1}{2}\frac{1}{2}\frac{1}{2} \rangle$	0.057	0.094	0.037
Li	4	$\left\langle \frac{1}{2}\frac{1}{2}\overline{\frac{1}{2}} \right\rangle$	0.024	0.028	0.008
F	4	$\langle \frac{1}{2}0\frac{1}{2} \rangle$	0.016	0.021	0.005
F	4	$\langle \frac{1}{2}\frac{1}{2}0 \rangle$	0.020	0.024	0.010
F	4	$\left\langle \frac{1}{2}0\overline{\frac{1}{2}} \right\rangle$	0.023	0.033	0.010
Li	1	$\langle 001 \rangle$	0.261	0.258	0.003

larisable environment (models B and C) appears for the Li^+ ion substituting Ba^+ host lattice ion. Relaxed position of this ion is substantially different from the position of the Ba^+ in the perfect crystal. Therefore, it is essential to use larger region I in order to allow such relaxation. Differences in atomic coordinates for other ions is noticeable but less significant.

Relaxation of the defect excited state ($5d^1_{z^2}$). The large value of the Stokes shift observed for the Ce^{3+} doped $LiBaF_3$ crystals suggests that the Ce^{3+} $5d^1_{z^2}$ excited state is strongly coupled with the host lattice. In other words, relaxation of the electronically excited $[Xe]5d^1_{z^2}$ configuration of the Ce^{3+} ion is associated with large displacements of nearby ions. The local atomic structures of the defect centre in its relaxed ground ($[Xe]5f^1$ configuration) and excited ($[Xe]5d^1_{z^2}$ configuration) states are shown in Fig. 11. Each fragment in Fig. 11 contains four unit cells: Ce^{3+} occupies the centre of the lower left unit cell; the associated with it charge compensating Li^+ ion substitutes the Ba^{2+} ion in the upper left unit cell; two unit cells on the right are structurally unchanged. It is immediately clear that in the relaxed excited state, the Ce^{3+} ion is substantially displaced towards the substitutional Li^+ ion and that the surrounding fluoride ions are noticeably distorted.

The calculated displacements of ions due to relaxation of the $5d_{z^2}$ excited state for all three models are summarised in Table 16. The first three columns in Table 16 show type of

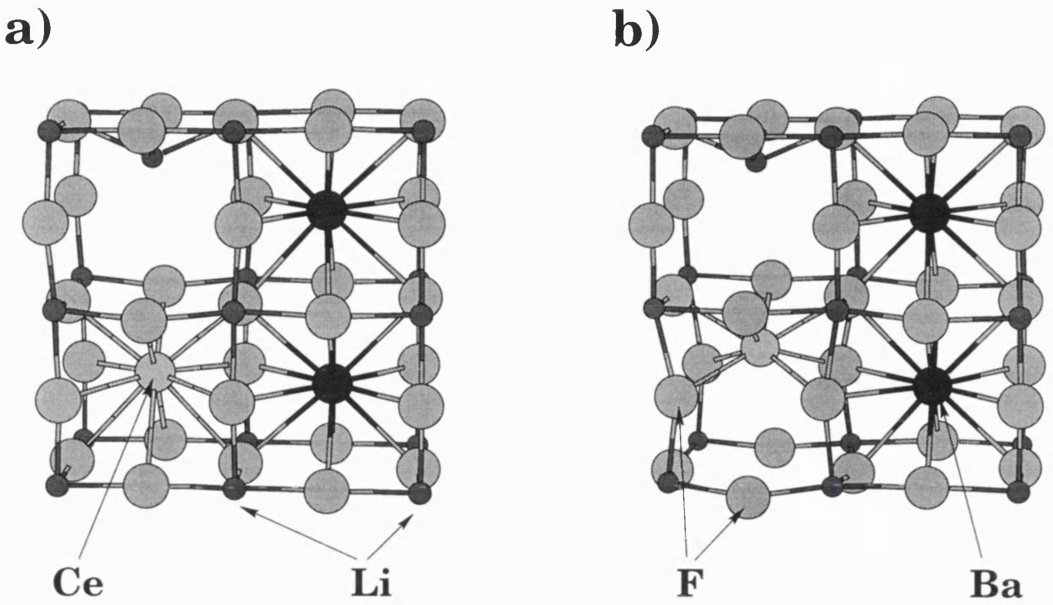

Figure 11: Local atomic structure of the Ce^{3+} ion in $LiBaF_3$.
a) relaxed ground state in $[Xe]5f^1$ configuration; b) relaxed excited state in $[Xe]5d^1_{z^2}$ configuration.

an ion, number of symmetry equivalent ions of this type, and its site position with respect to the centre of the cluster. The symmetry of the defect site is C_4 with the symmetry axis parallel to the z axis; therefore only ions which are in the same xy plane remain equivalent. Consequently, each row in Table 16 refers to ions with the same z coordinate. Comparison of the data in Table 16 shows that the displacements of ions in model A are about 0.1 Å larger than those in models B and C. This suggests that relaxation of atoms only inside the QM cluster is insufficient to achieve a fully optimised atomic structure for the defect centre. We expect that the approximation of the unpolarised environment may result in an incorrect prediction of other defect properties. It is important to note that the displacements of ions in models B and C are not very different, which means that relaxation of a just few additional atoms, as compared to the model C, in the vicinity of the QM cluster has insignificant effect on the local geometry of the system. Therefore, to achieve the correct atomic structure of the defect centre in both ground and excited states, relaxation of many atoms beyond the QM cluster, should be considered.

Optical transition energies. Both the excitation energies corresponding to the four $4f^1 \rightarrow 5d^1$ transitions and the luminescence energy of the defect centre depend on its local atomic structure. Therefore, it could be expected that models A, B, and C described above for the embedded cluster environment will result in different values of the optical transition energies. Results of our calculations are given in Tables 17 and 18.

It may be immediately noticed that the excitation energies only slightly depend on the accuracy with which the host lattice is treated. This corresponds to the relatively small

Table 16: Displacements of host lattice ions near the Ce^{3+} dopant in the defect excited state ($5d_{z^2}$).

Type and number of equivalent ions		Site	Displacements,Å Model A	Model B	Model C
Ce	1	$\langle 000 \rangle$	0.621	0.500	0.487
Li	4	$\langle \frac{1}{2}\frac{1}{2}\frac{1}{2} \rangle$	0.185	0.116	0.105
Li	4	$\langle \frac{1}{2}\frac{1}{2}\overline{\frac{1}{2}} \rangle$	0.113	0.112	0.108
F	4	$\langle \frac{1}{2}0\frac{1}{2} \rangle$	0.230	0.176	0.187
F	4	$\langle \frac{1}{2}\frac{1}{2}0 \rangle$	0.333	0.242	0.241
F	4	$\langle \frac{1}{2}0\overline{\frac{1}{2}} \rangle$	0.328	0.225	0.196
Li	1	$\langle 001 \rangle$	0.027	0.020	0.025
Ba	4	$\langle 100 \rangle$	0.054	0.057	
Ba	1	$\langle 00\bar{1} \rangle$	0.018	0.047	
Ba	4	$\langle 101 \rangle$	0.051	0.026	
Ba	4	$\langle 110 \rangle$	0.047	0.032	
Ba	4	$\langle 10\bar{1} \rangle$	0.062	0.023	

differences in defect local atomic structures for the ground state calculated using models A, B, and C. On the contrary, the calculated value of the luminescence energy gradually increases as the size of the polarisable region I decreases. In the limit of the unpolarisable environment (model C) the luminescence energy is by more than 0.3 eV larger than for the case of the fully polarisable environment (model A). As expected, the model of the partly polarisable environment (model B) results in an intermediate value of the luminescence energy. Similarly, the magnitude of the Stokes shift decreases as the size of the polarisable region decreases.

It is worthwhile emphasising that the luminescence energy does not show fast convergence with respect to the size of the polarisable region. For example, relaxation of 17 more atoms in model B, as compared to the model C, results in the decrease of the luminescence energy by only 0.06 eV. Furthermore, our analysis shows, that relaxation of the excited state causes appreciable displacements of ions far from the defect site. For instance, ions at the boundary of the large region I (model A) are relaxed by as much as 0.002 Å, even though they are almost 14 Å away from the defect centre.

Following the work of Marsman *et al.* [136], we introduce a correction to the calculated optical transition energies. The correction arises from the fact that a finite Gaussian type basis set was used in the calculation. To calculate this correction, the authors have compared the $^2F_{7/2} \rightarrow ^2D_{5/2}$ transition energy for the free Ce^{3+} ion calculated using a fully relativistic Multi-Configurational Dirac-Fock (MCDF) code with a numerical representation of the wave function [46] and that calculated using the Gaussian94 [78], both at the Hartree-Fock level. The transition energy calculated using the Gaussian94 was about 0.8 eV larger than that calculated using the MCDF code and therefore the correction due to the finite basis set was taken to be -0.8 eV. We should mention that this correction does

Table 17: Optical transition energies for different models of the embedded cluster environment.

		Transition energies, eV		
	Assignment	Model A	Model B	Model C
Excitation	$4f \rightarrow 5d_{z^2}$	5.751	5.706	5.687
	$4f \rightarrow 5d_{x^2-y^2}$	6.000	6.044	6.051
	$4f \rightarrow 5d_{xy}$	6.512	6.452	6.448
	$4f \rightarrow 5d_{xz}, 5d_{yz}$	6.572	6.576	6.550
Luminescence	$5d_{z^2} \rightarrow 4f$	4.547	4.815	4.875
Stokes shift		1.204	0.891	0.812

Table 18: Comparison of the calculated optical transition energies with results of earlier studies and experiment.
All calculated values are corrected for the effect of a finite Gaussian type basis set. See text for more details.

		Transition energies, eV		
	Assignment	This work	Theory [136]	Experiment [37]
Excitation	$4f \rightarrow 5d_{z^2}$	4.949	4.886	4.960
	$4f \rightarrow 5d_{x^2-y^2}$	5.198	5.241	5.166
	$4f \rightarrow 5d_{xy}$	5.710	5.493	5.688
	$4f \rightarrow 5d_{xz}, 5d_{yz}$	5.770	5.879	6.078
Luminescence	$5d_{z^2} \rightarrow 4f$	3.745	4.279	3.875
Stokes shift		1.204	0.607	1.085

not depend on the host material and, therefore, does not take into account the dependence of the Ce^{3+} electronic structure on the host crystal and on the relaxation of the local crystal environment. We did not consider a separate correction for a correlation energy due to the fact that its effect on the transition energies seems to be compensated, accidentally, by the effect of the host crystal. See reference [136] for a more extensive discussion in this matter.

The corrected energies for model A are compared with those calculated in [136] and with experimental data in Table 18. The comparison suggests that the excitation energies obtained in the present study are, generally, in better agreement with the experiment than those calculated in [136]. A much greater improvement is achieved for the luminescence energy and the Stokes shift.

3.2.5 Summary

We have undertaken an embedded cluster study of the local atomic structure and optical properties of a luminescence centre formed by doping Ce^{3+} ions into $LiBaF_3$. In this study we considered different models of the cluster environment which correspond to polarisable, partly polarisable and unpolarisable crystal lattice and investigated effect of these models on the properties of the defect centre. It was found that the distortions of the host lattice near the defect in its ground state are very localised and that its atomic structure is similar for all three models of the environment. On the contrary, the relaxed atomic structure of the defect in its excited state differs for different models of the environment. In particular, the model of the unpolarisable lattice results in underestimation of the displacements of ions in the QM cluster. We have noticed that ions which are as far as 14 Å away from the defect centre were displaced by 0.002 Å, which suggests that relaxation of a large number of ions surrounding the defect site should be considered. The calculated values of the excitation and luminescence energies correlate with the geometry of the defect centre: excitation energies show almost no dependence on the relaxation of the cluster environment while the luminescence energy differs by more than 0.3 eV. Finally, we compared the results of our calculations with those of earlier theoretical [136] and experimental [37] studies of the optical properties of the $LiBaF_3$:Ce^{3+} system. This comparison demonstrated that the present embedded cluster calculations provided a better agreement with the experimental data than a combined embedded cluster and periodical plane wave calculations reported in [136]. We, therefore, conclude that proper modelling of the polarisable host lattice is a vital part of embedded cluster studies. Neglect of the lattice polarisation may result in incorrect values of optical transition energies and Stokes shift for defect centres in which the electronic excitation is strongly coupled with the lattice displacements.

4 Defects at the surface of MgO

The MgO (001) surface has been extensively studied both experimentally and theoretically primarily due to its importance for technological applications in catalysis and as a substrate for growing many different systems. The latter include metal layers, superconductors and ferroelectrics. The simple crystal structure and ionic character of the interatomic bonding enable theoretical studies using relatively simple models. The (001) surface of MgO is often considered as a model system and used to examine new experimental or theoretical techniques. Although the MgO (001) surface has been well characterised, little attempt has been made to address the issue of the position of the surface valence band and defect states relative to a common reference level. This is one of the key issues important for both the interpretation of experimental spectra and studies of surface processes involving point defects.

In this Chapter we present the results of our studies of the properties of the ideal MgO (001) surface and point defects on its terraces and at low-coordinated surface sites [205], [204], [192]. We aim to calculate the energy levels of the defect states and surface excitons with respect to the top of the surface valence band and the vacuum level. In section 4.1, the electronic properties of the ideal surface and surface defects are considered. The value of the ionisation potential which sets the position of the top of the valence band with respect to the vacuum is discussed in sub-section 4.1.4. The calculation of the surface electron affinity and of the position of the conduction band of the surface are discussed in 4.1.5. The electronic properties of the oxygen corner, and those of the oxygen vacancies and surface peroxide species are calculated in sub-sections 4.1.6, 4.1.7, and 4.1.8, respectively. Section 4.2 deals with the calculations of optically excited states at the low-coordinated MgO sites.

4.1 Electronic properties of the ideal and defective surface

4.1.1 Experimental background

To bring energy levels of the ideal surface and surface defects to a single energy scheme, one has to determine their positions with respect to a common reference level. Usually the vacuum level is used for this purpose. We are aware of two experiments which aim to determine the position of the top of the surface valence band with respect to the vacuum level. The results reported by Tjeng *et al.* [209] were obtained using the angle-resolved ultraviolet photoelectron spectroscopy (ARUPS). In this experiment the surface is irradiated by a beam of photons (21.2 eV and 40.8 eV photons have been used) and the distribution of kinetic energies of emitted electrons provides insight into the electronic structure of the material. Analysis of the experimental data led the authors to conclude that the ionisation potential of MgO is about 9.1 eV with an uncertainty of a few tenth of an eV. Another set of experiments have been conducted by Kempter *et al.* [114] using Metastable Impact Electron Spectroscopy (MIES). In this experiment, excited He atoms (in electronic configuration $1s^1 2s^1$) are scattered from the surface with thermal velocities. When a He* atom approaches the surface, an electron from the surface valence band tunnels into the unoccupied 1s state of the atom and the 2s electron of the He* is simultaneously released carrying the difference in energy between the valence electron and the 1s He* states. The electron tunnelling is effective predominantly from the top surface layer. The distribution of kinetic energies of the emitted electrons is measured and analysed using theoretical modelling [114], [115]. MIES suggests that the surface IP is in the range of 6.7 ± 0.4 eV.

It is important to stress that the MIES technique probes predominantly the surface states [120], whereas ARUPS probes the electron states in several surface layers and is, therefore, dominated by contributions due to the sub-surface layers. These experimental observations suggest that there is a considerable (about 2.4 eV) splitting between the bulk and surface states which has neither been observed experimentally nor appeared in theoretical simulations. To the best of our knowledge there are no other experimental data we could rely on in this discussion. To clarify this issue we have performed *ab initio* calculations of the ionisation potential of the ideal surface which are described below.

F centres, also known as colour centres, are defects typical to ionic crystals. They essentially consist of electrons trapped in anion vacancies and can be generated by exposure of a crystal to radiation of suitable wavelength (known as radiative colouring) or by metal addition at high temperatures (additive colouring). Investigation of these centres has been extensive, and more than 50 years ago Wood and Joy [220] nicely expressed this interest: "This defect is one of the simplest which can occur in ionic crystals, and in the physics and chemistry of lattice defects it occupies a position of importance roughly comparable to that of the hydrogen atom in ordinary chemistry".

For many years, the study of F centres remained firmly within the domain of physics until the late 1960s when the surface counterparts (F_s) of the bulk centres were discovered and explored for the first time (see [146] and references therein). These surface centres were predominantly generated on alkaline earth metal oxides by exposure of the oxide to gamma or UV irradiation under H_2. Containing an abundance of surface stabilised electrons, the radiatively coloured materials soon attracted a great deal of interest from a wider chemical community since the formation of surface radical anions by electron transfer from centres to various adsorbates could be easily studied. Interest in both the chemical properties and magnetic features of the surface centres became intense and was actively pursued for many years. Some fundamental questions about the exact nature of the surface trapped electron centres have, however, remained unresolved (see, for example, recent extensive studies of trapped electron centres on alkali metal doped MgO by Giamello *et al.* [144], [145], [30], [143]).

Following Giamello *et al.* [30] we can outline areas of particular interest and directions for further research regarding the structure and properties of surface F centres. These concern: i) the nature, location and concentration of the surface anion vacancies capable of electron trapping; ii) the reactivity of the surface trapped electrons with adsorbed atoms and molecules; iii) the generation and exploration of not only "classical" F centres but also of new families of surface trapped electron species: these species have also been identified in zeolites [58] and [4], a surface F^+ centre which is fundamentally different from the classical surface $F^+(H)$ centre was reported in a very recent study of MgO nano-particles [198]; iv) the coupling of experimental investigations with theoretical modelling which is a fruitful approach providing a deeper insight into the nature and the variety of surface F centres.

Although the properties of F centres in the bulk of crystals have been the subject of numerous investigations over several decades, few experimental data are available for F centres at surfaces and other low-coordinated sites. Experimental studies are hampered by much smaller concentrations of surface defects as compared to the bulk. Consequently, theoretical modelling of the processes involving surface defect sites becomes a useful tool for the understanding and interpretation of the experimental data. Among the most recent publications which combine experimental and theoretical studies of electron traps at the MgO (001) surface we should mention [151], [45], [114].

4.1.2 Details of calculations

To simulate the MgO surface we used a nano-cluster in the form of parallelepiped containing 20×20×8 ions carrying formal ionic charges. The size of this nano-cluster was 40 Å in the x and y directions and 15 Å in the z direction. Region I (see Chapter 2) is also rectangular and contains 12×12×6 ions, as shown in Fig. 12(a). The calculations were made for a series of clusters of increasing surface area and number of layers (see Fig. 13(a-e)) embedded into the nano-cluster. The choice of the cluster shape was determined by the following considerations. Electronic holes favour sites with lower electrostatic potential. On the perfect surface, all anion sites are equivalent and the hole is expected to have equal probability to localise on any anion. To describe delocalised hole states, it is important to include in the cluster several equivalent sites. To study the dependence of the surface ionisation energy on the degree of the hole localisation, clusters including one, five, nine and thirteen surface oxygen ions were considered. We have also investigated the dependence of our results on the "thickness" of the QM cluster. For this purpose, the QM clusters including ions of two and three surface layers have been studied (compare clusters in Fig. 13(c) and Fig. 13(d)). The largest cluster considered in this study, included 25 oxygen and 57 magnesium ions (Fig. 13(e)).

The calculations of the surface oxygen vacancies (neutral F centre, charged F^+ centre and anion vacancies V_a) and peroxide species have been performed using the nano-cluster shown in Fig. 12(a)) and the $Mg_{29}O_{13}$ quantum cluster (Fig. 13(d)). For the studies of oxygen vacancies at the oxygen corner site the cubic 20×20×20 ion nano-cluster was used (part of it is shown in Fig. 12(b)). The shell model region I for this nano-cluster was also cubic; its size was varied from 4×4×4 to 10×10×10 to investigate the effect on the corner site relaxation. The QM clusters used in these calculations are shown in Fig. 13(f,g).

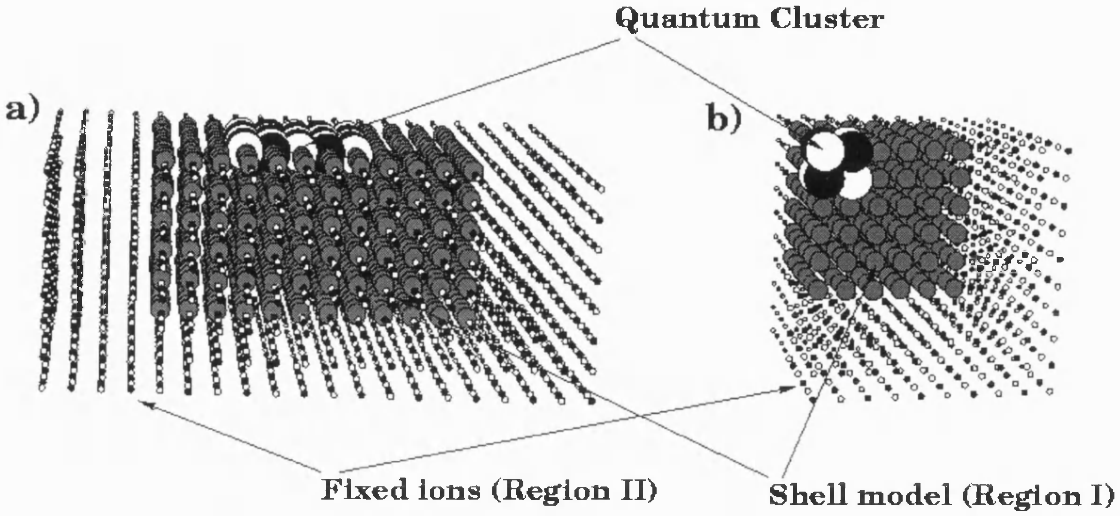

Figure 12: The models for the surface (a) and corner (b) used in the embedded cluster calculations. Large black and white spheres define a quantum cluster; grey spheres correspond to region I treated using the shell model; small points correspond to the fixed environment represented using point charges.

The quantum mechanical calculations have been made at the DFT level using the B3LYP density functional [15], [16]. Other details of the model and computational procedure have been described previously in Chapter 2.

The general shape of the QM clusters and the flexibility of the basis set on different ions have been described earlier (Chapter 2). Here we note only that most of the calculations have been made using the standard 6-31G basis set for all oxygen ions and the magnesium ions coordinated by three or more QM oxygens. All other (boundary) magnesiums have been described using an effective core pseudo-potential replacing 1s, 2s and 2p electrons [216] and a single s-type basis function contracted from two primitive s functions. In some of the calculations the basis set was extended up to a 6-311+G ((12s,6p)→(5s,4p) contraction) on oxygens and a 6-311G ((13s,9p)→(6s,5p) contraction) on magnesiums.

To investigate the role of polarisation functions on the defect properties, we have performed calculations of the formation energy of the surface F centre and its ionisation energy for different clusters (Fig. 13(a-c)) and different basis sets using the unpolarisable lattice model. The 6-31G basis set was used for the all-electron cations while the basis set for all anions was increased from a 6-31G to a 6-311G and then to a 6-311G* (the corresponding oxygen basis set was also centred on the oxygen vacancy). The formation energy of the surface F centres decreased by about 0.1 eV as the basis set was enlarged. The corresponding changes of the ionisation energy were about 0.05 eV, which led us to conclude that the polarisation functions introduce only a minor effect on the calculated properties although their effect on the total energy of the system could be large. Our other calculations (see Chapter 3) also suggest that extension of the basis set by the polarisation functions only slightly affects the calculated values but makes the calculations much more time-consuming. For this reason, d-functions have not been included in the calculations.

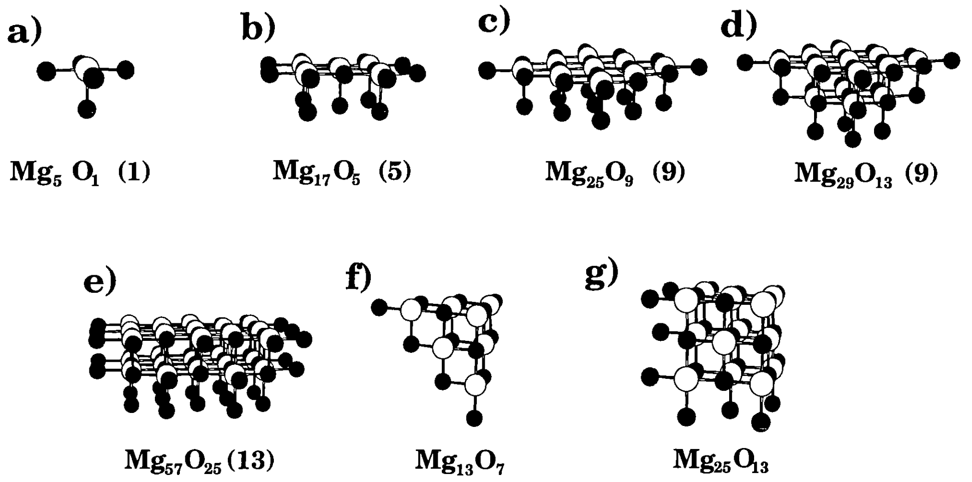

Mg_5O_1 (1) $Mg_{17}O_5$ (5) $Mg_{25}O_9$ (9) $Mg_{29}O_{13}$ (9)

$Mg_{57}O_{25}$ (13) $Mg_{13}O_7$ $Mg_{25}O_{13}$

Figure 13: The quantum mechanically treated clusters used in the embedded cluster calculations of the surface and corner states.

4.1.3 MgO (001) surface rumpling

The most stable (001) surfaces of cubic ionic crystals, such as alkali halides and alkaline earth oxides, experience a characteristic relaxation with respect to an ideal cleavage plane. Both experimental observations and theoretical calculations (see [170], [82] and references therein) suggest two features which are common for this relaxation: i) the surface plane moves as a whole towards the bulk decreasing the distance between the surface and the sub-surface layers, and ii) cations of the surface layer are displaced towards the bulk more than anions. The latter feature is known as rumpling. Although there is a considerable difference between the values of ionic displacements obtained in different studies, there seems to be a general consensus that both the relaxation and rumpling at the MgO (001) surface are small. The shift of the surface plane as a whole, quoted in many studies (see [82] and references therein), is about one percent of the anion-cation separation. The surface rumpling, defined as the difference between the mean vertical position of oxygen and magnesium ions, in most cases does not exceed four percent of the anion-cation separation. For instance, the rumpling predicted in recent periodic DFT calculations [113] was 0.04 Å, which is about two percent of the anion-cation separation.

In our modelling of the MgO surface, we first relaxed the whole system classically using the pair potentials [191]. The ionic displacements obtained from the ideal surface plane positions were 0.004 Å for anions and -0.006 Å for cations, i.e. anions moved up and cations down towards the bulk in qualitative agreement with previous results. The surface ions outside region I were then fixed in these positions. The positions of ions within the QM cluster were determined self-consistently with the relaxation of the classical ions in

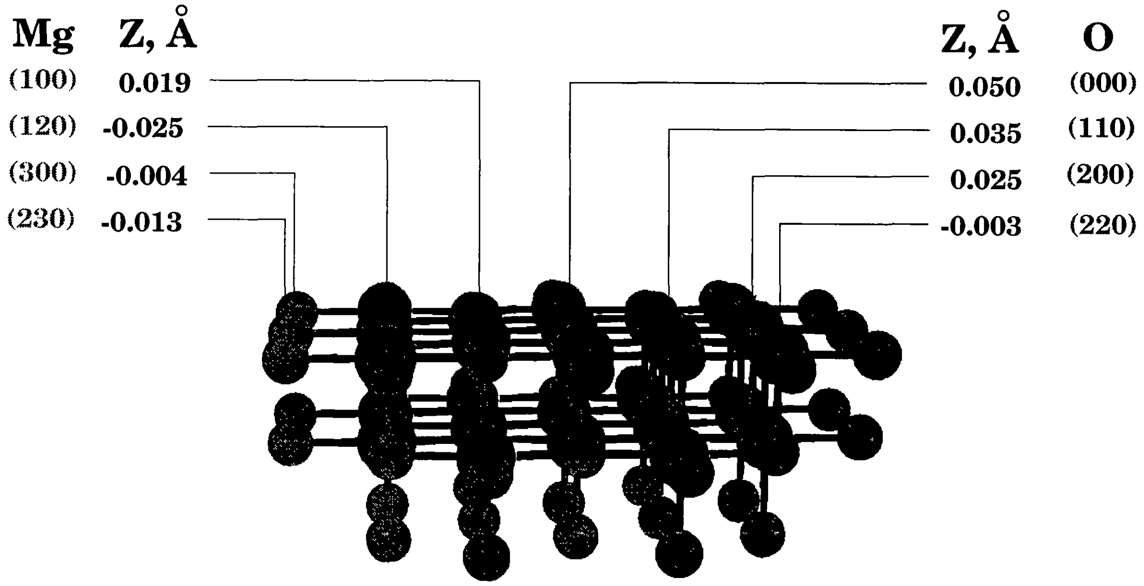

Figure 14: Rumpling for the MgO (001) surface.
Displacements of ions in the $Mg_{57}O_{25}$ cluster with respect to the ideal unrelaxed surface; positive Z corresponds to displacements up from the ideal unrelaxed surface.

region I. The displacements of ions in the direction perpendicular to the surface depend on the size of the QM cluster and on the positions of the ions relative to the centre of the cluster. The character of the rumpling is different for two- and three-layer clusters. For the two-layer clusters, all anions, apart from the case of the smallest QM cluster (Fig. 13(a)), relax to positions 0.05-0.07 Å below the level of the ideal unrelaxed surface; at the same time cations, on average, relaxed to the positions only 0.00-0.02 Å below the same level. The expected displacement of the surface layer as a whole is therefore reproduced but the relative displacements of anions and cations are opposite to those predicted by experiment and by previous calculations [170]. Further extension of the quantum mechanically treated region to include the anions of the sub-surface layer and cations of the third layer changes the calculated rumpling parameters. Good agreement with results of slab DFT calculation [113] was achieved for the cluster $Mg_{57}O_{25}$ (Fig. 13(e)). The displacements of the surface ions for this cluster with respect to the ideal unrelaxed surface are shown in Fig. 14.

4.1.4 Position of the top of the valence band: Ionisation potential of the MgO (001) surface

The results of calculations are summarised in Table 19. The meaning of the ionisation potentials IP(0) and IP(I) has been defined above in Chapter 2. The difference between them shows the effect of the electronic lattice polarisation due to the ionisation of the cluster. One can see that the lattice polarisation plays an important role both in reducing the value of the ionisation potential and in enhancing the convergence of the results with the cluster size to about 6.5 eV.

The electron is ionised from the highest occupied (HOMO) state which, in our cluster

Table 19: Ionisation potential of the (001) MgO surface calculated using different QM clusters.

QM cluster	N(oxygen)	IP(0), eV	IP(I), eV	ΔIP, eV	$W^{b)}$, eV
Mg_5O_1	1 (a)	9.75	7.64	2.11	0.68
$Mg_{17}O_5$	5 (b)	7.89	6.86	1.03	2.02
$Mg_{25}O_9$	9 (c)	7.25	6.48	0.77	2.25
$Mg_{29}O_{13}$	9 (d)	7.18	6.47	0.71	2.82
$Mg_{57}O_{25}$	13 (e)	7.03	6.52	0.51	3.13

[a)] The number of surface oxygens in the cluster and the notation of a corresponding ball-stick model in Fig. 13.

[b)] The width of the surface valence band, W, was calculated as the energy difference between the highest and lowest occupied states of the valence band.

calculations, corresponds to the top of the valence band and is localised, primarily, within the top surface layer. The ionisation energy depends on the cluster size in several ways. i) As the number of surface ions increases, the degree of delocalisation of the hole state also increases. The latter reduces the polarisation energy of the environment defined as IP(0)-IP(I). The hole is almost exclusively localised in the top surface layer and homogeneously distributed over the surface anions, which is demonstrated in Table 20 where we summarised the differential charges on the surface oxygens. The charges were calculated using the Natural Population Analysis (NPA) [167] as the difference between the ionic charges in the perfect and ionised clusters. ii) The energy of the HOMO state changes with the cluster size as the splitting of the cluster states modelling the valence band increases and the position of the middle of the band shifts to lower energies. The first of these effects is clearly seen in Table 19 where we present the valence band width for different clusters. iii) The polarisation contribution decreases with the cluster size not only due to hole delocalisation, but also due to the fact that more ions are treated quantum mechanically and that the polarisabilities of the quantum ions are much smaller with the basis sets used in this study (and indeed in much more extended basis sets [75]) than the experimental values. For the same reasons, one also expects the ionisation energy to depend on the basis set. To check this effect we increased the basis set on the oxygen ions to 6-311+G and on the all-electron magnesium ions to 6-311G, and calculated the ionisation energy for the largest cluster using the positions of QM ions and classical cores and shells as optimised using the smaller basis set. The ionisation potential obtained in this calculation was 6.75 eV, which demonstrates further convergence to the experimental value of 6.7 ± 0.4 eV. Thus the agreement between theory and experiment is within experimental error although the results do not demonstrate complete convergence. It is tempting to extrapolate the ionisation energy to the case of a larger cluster, but due to the complicated interplay of several factors, this extrapolation by four points is not justified. Nevertheless, we do not expect the calculated value of about 6.7 eV to change significantly with a further increase of the cluster size.

The localisation of the hole can be analysed by means of the spin density map or the

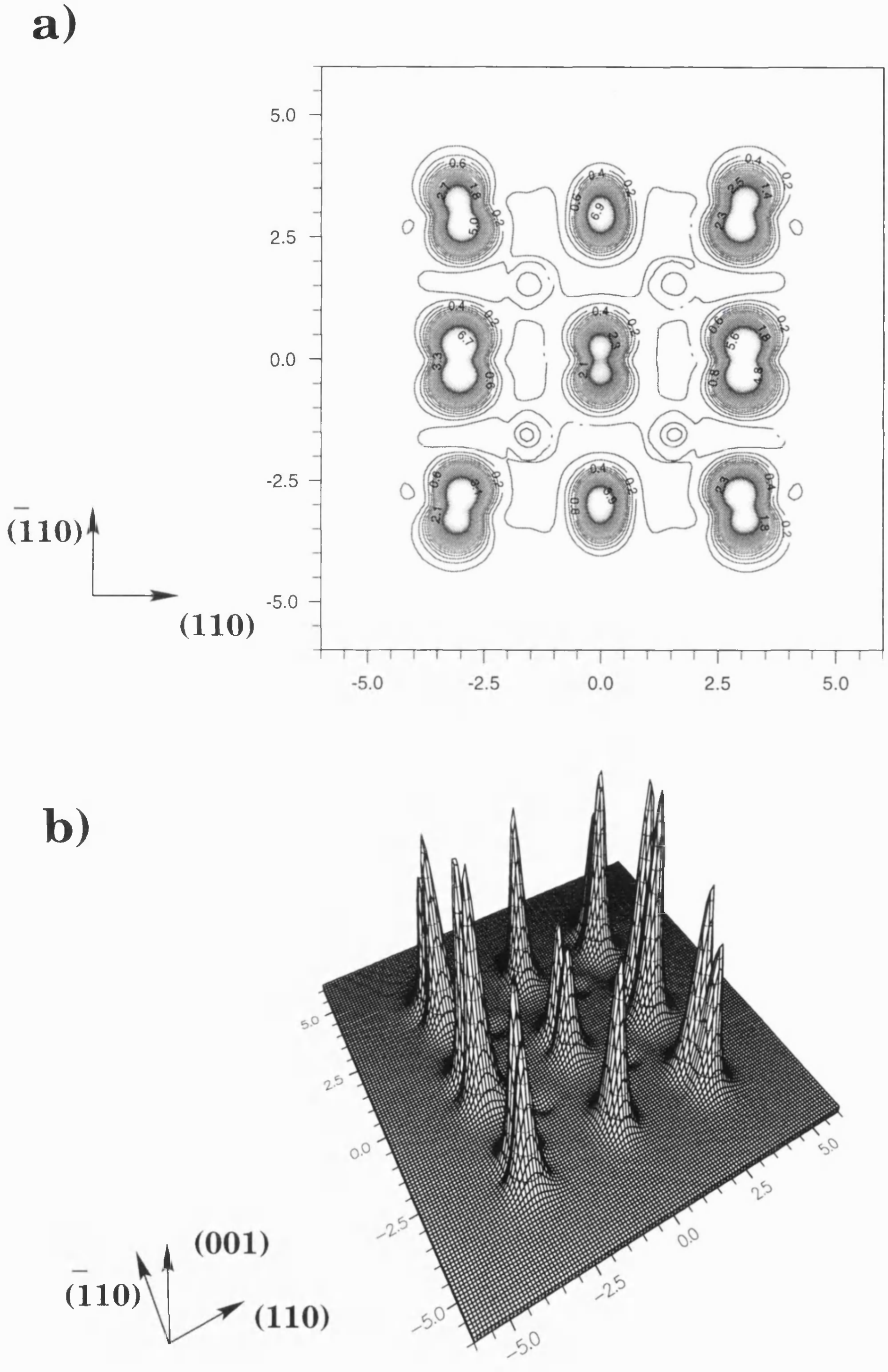

Figure 15: The spin density of the hole state at the MgO (001) surface. Both plots show top layer of the (001) surface plane: a) two-dimensional projection; b) tree-dimensional plot, similarity of peaks indicate approximately uniform distribution of the hole.

Table 20: The distribution of the electron hole in the top surface layer of MgO clusters calculated as difference between NPA charges on oxygen ions for the perfect surface and ionised states.

QM cluster	Fig. 13	[000][a)]	[110]	[200]	[220]
Mg_5O_1	(a)	0.907			
$Mg_{17}O_5$	(b)	0.146	0.0167-0.170		
$Mg_{25}O_9$	(c)	0.072	0.083-0.090	0.095-0.103	
$Mg_{29}O_{13}$	(d)	0.035	0.074-0.0110	0.083-0.086	
$Mg_{57}O_{25}$	(e)	0.032	0.018-0.018	0.058-0.066	0.041-0.046

[a)] Numbers in square brackets refer to the position of symmetry equivalent oxygen ions relative to the cluster centre (see Fig. 13).

ionic charges obtained using a population analysis. The spin density in the surface plane for the cluster $Mg_{29}O_{13}$ in its ionised state is shown in Fig. 15. The two-dimensional plot (Fig. 15(a)) of the spin density demonstrates that the hole state has primarily a p-character in accord with the 2p nature of the valence band. It can also be seen (Fig. 15(a) and (b)) that the hole is almost homogeneously delocalised over the anions of the surface layer. The NPA analysis [167] shows that ions which are equivalent with respect to the centre of the QM cluster have equal ionic charges in the ground state of the system. These charges, however, become different in the ionised state due to i) much more complex profile of the adiabatic surface and ii) the fact that the wave function of the ionised state may have symmetry lower than the symmetry of the Hamiltonian.

4.1.5 Position of the bottom of the conduction band: Electron affinity of the surface

We can now use the calculated value of the surface IP in order to predict other properties of the surface electronic structure. The consistency of our results may then be tested by direct calculation of the predicted properties. In particular, if the position of the top of the surface valence band and the surface exciton energy are known, one can estimate the position of the surface conduction band. Experimentally, the electron energy loss spectra [93] demonstrate a peak at about 6.2 eV, which is attributed to the surface exciton. Using this value and the experimentally determined position of the top of the valence band, we can position the exciton state at $-6.7 + 6.2 = -0.5$ eV with respect to the vacuum level. Assuming, by analogy with MgO bulk and other materials, that the bottom of the conduction band is located several tenth of an eV above the exciton state, the prediction for the bottom of the conduction band would be about zero.

To study the energy and the nature of the electronic states at the bottom of the surface conduction band, we performed calculations of the electron affinity (EA) of the embedded $Mg_{57}O_{25}$ cluster using several extended basis sets. An electron was added to the cluster and its electronic structure was calculated self-consistently with the displacements of shells in region I as described in Chapter 2. The electron affinity was calculated as the difference between the total energy of the system with ($E(n+1)$) and without ($E(n)$) an additional electron: EA $= E(n) - E(n+1)$. As we increased the basis set on Mg ions from 6-31G to 6-311G on cations and that on oxygen ions from 6-31G to 6-311+G, the calculated value of EA gradually increased from -0.91 to -0.56 eV. In other words, in our calculations, the bottom of the (001) surface conduction band of MgO is at about 0.5 eV in the positive energy spectrum. This result agrees well with our other theoretical prediction of the bottom of the CB based on the calculation of the excitation energy of the surface exciton (see section 4.2) but is higher than the value estimated from experimental data. The obvious contributions to this discrepancy come from the small number of cluster ions leading to a conduction band that is too narrow and an overestimate of the kinetic energy of the additional electron in the cluster confinement.

The unbound state of the additional electron does not allow us to elucidate the nature of the occupied electronic state at the bottom of the MgO conduction band. The spin density plots presented in Fig. 16 demonstrate two effects: i) the additional electron along the surface plane is localised within the QM cluster (Fig 16(a)), which shows that the embedding scheme does not allow the electron to escape the cluster due to the attraction of the positive point charges around the cluster; and ii) the additional electron occupies the most diffuse atomic orbitals which belong to Mg ions (Fig. 16(b)). Our calculations of the nature of excited states at the MgO (001) surface suggested that the bottom of the conduction band has a mixed Mg and O character. The predominantly anion character of the MgO bulk conduction band was proposed in [43]. Although in the present work we can for the first time discuss the occupied states at the bottom of the conduction band, both their nature and the position of the band edge with respect to the vacuum remain unclear.

4.1.6 Oxygen corner

We have applied the same approach to the study of the ionisation potential and electron affinity of an oxygen corner. An additional challenge of this calculation is presented by the atomic structure of the corner. The set-up used in these calculations is shown in Fig. 12(b) and the QM clusters in Fig. 13(f,g). Qualitatively, the relaxation of steps and corners tends to round them by displacing the low-coordinated ions inwards the surface. As we discovered, the actual geometry of the corner depends on the size of the region I, which is allowed to relax. In Table 21 we present the displacements of the corner oxygen ion from an ideal bulk termination (where its coordinates were (0.0, 0.0, 0.0)) as a function of the size of region I. We see that the absolute displacement of the corner ions increases with the size of region I. This results from small displacements of the many ions involved in the relaxation as region I is enlarged. It is clear from Table 21 that this process converges slowly and indeed we were unable to achieve full convergence. However, the ionisation energy of the corner, also presented in Table 21 converges much faster and reaches about 5.6 eV for our usual basis set. An additional expansion of the basis set on the corner

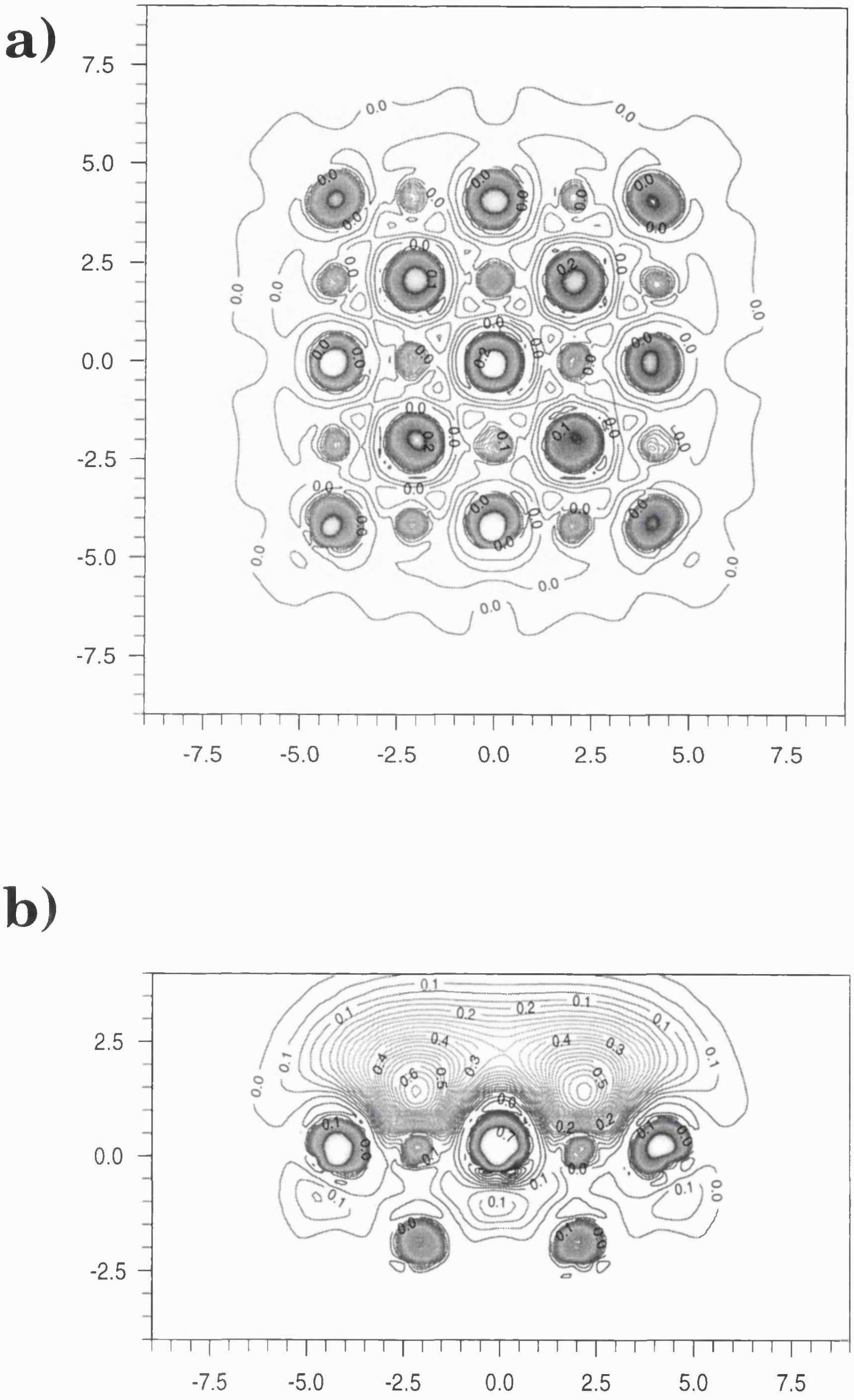

Figure 16: The spin density of the additional electron in the $Mg_{57}O_{25}$ cluster modelling the (001) MgO surface.
a) top layer of the MgO (001) surface plane (top view);
b) section perpendicular to the MgO (001) surface plane, mushroom-like "hat" of the spin density in the free space above the (001) surface plane indicates delocalisation of the additional electron just above the top layer of the QM cluster.

Table 21: The relaxation and ionisation potential of the oxygen corner site as a function of the size of region I and the basis set.
Model for the oxygen corner is shown in Fig. 12(b). The third column contains the $x = y = z$ components of the displacement of the corner oxygen along the $\langle 111 \rangle$ crystalline axis inside the cluster.

QM cluster	Region I	Δx,Å	IP(0), eV	IP(I), eV	ΔIP, eV
$Mg_{13}O_7$	4x4x4	0.284	6.11	5.81	0.30
$Mg_{13}O_7$	6x6x6	0.344	6.15	5.70	0.45
$Mg_{13}O_7$	8x8x8	0.395	6.17	5.65	0.52
$Mg_{13}O_7$	10x10x10	0.431	6.18	5.62	0.56
$Mg_{13}O_7$ $^{a)}$	6x6x6	0.342	6.20	5.75	0.45
$Mg_{25}O_{13}$	6x6x6	0.339	5.98	5.67	0.32

$^{a)}$The basis set for the corner oxygen was extended by two diffuse *sp* functions.

oxygen ion by two diffuse *sp* functions increases the ionisation potential by about 0.05 eV. The increase of the cluster size to $Mg_{25}O_{13}$ (Fig. 13(g)) also changes the ionisation potential by only 0.05 eV. The calculated electron affinity of the oxygen corner is about -1.4 eV, i.e. due to reduction of the crystalline potential it is unlikely that an electron can be trapped near this site.

The hole state formed just after the electronic relaxation is already well localised at the corner as demonstrated in Fig. 17(a). One can clearly see the main *p*-like spin density peak on the corner oxygen with additional, much smaller, peaks on other surrounding oxygen ions in the cluster. Minimisation of the total energy with respect to all coordinates leads to significant displacements of the corner oxygen and surrounding ions and is accompanied by a stronger hole localisation on the corner ion (see Fig. 17(b)). The oxygen ion is displaced along the $\langle 111 \rangle$ crystalline axis further inside the cluster by about 0.03 Å whereas the three neighbouring Mg ions are displaced inside the cluster, approximately along the corner edges, by about 0.13 Å.

The calculated ionisation potential for the anion corner allows us to estimate that the expected separation of the corner states from the top of the surface valence band is about 1 eV. The same value has been obtained in periodic DFT calculations of a corner system at the MgO surface [113].

4.1.7 Surface and corner F, F$^+$ and V$_a$ centres

The results of our calculations for the three charge states of the anion vacancy at the surface and at the anion corner are summarised in Tables 22 and 23. In Table 22, the defects are characterised by the F centre formation energy corrected for the basis set superposition error [20], the relaxation of the nearest neighbour cations, and the NPA occupations (spin density) of the 3*s* orbitals of the nearest neighbour Mg ions. To characterise the degree of electron localisation in the surface vacancy, we also use the value of the electron density integrated within a sphere of radius 1.68 Å centred on the vacancy (see Fig. 18). The

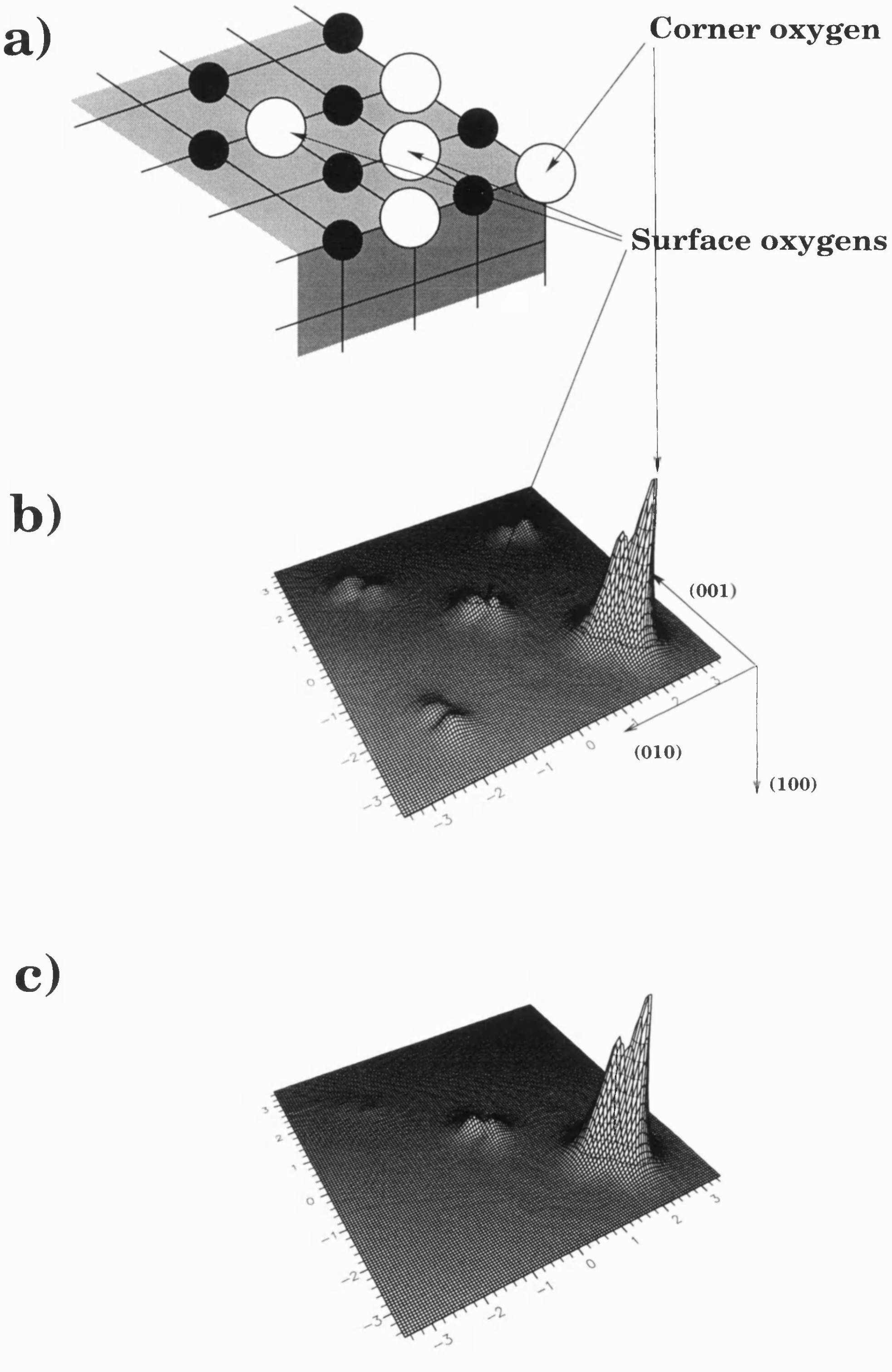

Figure 17: The spin density of the hole state at the oxygen corner of the MgO. Plots picture MgO (001) surface plane close to the terminating oxygen corner: a) schematic diagram of the oxygen corner site (white circles are oxygens, black circles are magnesiums); b) the spin density after vertical ionisation; c) the spin density after full ion relaxation. Strong peak in plots b) and c) is associated with the corner oxygen.

Table 22: Characteristics of the three charge states of the anion vacancy at the (001) surface and the anion corner of MgO.
Δx are the displacements of the nearest neighbour Mg ions along the surface axes. Mg $3s$ occ. are the NPA occupations of the Mg $3s$ orbitals and spin density in the case of the F^+ centre.

	Surface				Corner			
Defect	Δx,Å	Mg $3s$ occ.		E_{form}, eV	Δx,Å	Mg $3s$ occ.		E_{form}, eV
F	0.07	0.595		9.07	0.08	0.752		7.24
F^+	0.16	0.455	0.117 $^{a)}$		0.17	0.525	0.207 $^{a)}$	
V_a	0.25	0.347			0.28	0.336		

$^{a)}$Spin density.

radius of the sphere was chosen so that the total electron charge of a regular surface oxygen ion integrated within this sphere was ten electrons. Note that the density, integrated within the vacancy, and the NPA populations of cations (Table 22) complement each other only qualitatively.

The relaxation of the cations surrounding the vacancy essentially reflects the electron localisation which, for the case of vacancies at the surface, is shown in Fig. 18. For the neutral F centre, about $1.5e$ are localised within the vacancy and the displacements of the surrounding cations are relatively small; the displacements become much bigger for the F^+ centre and the bare anion vacancy. The value of the displacements obtained in our calculations are close to those reported in recent publications [65], [182], [68]. The formation energy of the surface F centre which was calculated as the energy required to remove a surface oxygen atom to infinity, was close to the value of 9.35 eV obtained in [182] using a different embedding procedure, and to that of 9.02 eV obtained in a recent periodic DFT calculation [188].

The calculated values of the ionisation energies and electron affinities are presented in Table 23. Their physical meaning is illustrated in Fig. 19. A "vertical" ionisation of a defect, which requires energy $E_{ion}(v)$, is followed by a lattice relaxation, which gives the energy gain $E_{rel}(i)$. The electron affinity was calculated for completely relaxed defect states: a "vertical" affinity, $E_{aff}(v)$, was calculated for the fixed positions of the nuclei of the quantum ions and classical cores; the electron affinity corresponding to complete lattice relaxation is denoted $E_{aff}(r)$. As one can see in Table 23, the values of ionisation energies and electron affinities depend significantly on the lattice polarisation. The typical difference between the two values is about 0.6 eV.

An anion vacancy at the corner is significantly different from one at the surface. Based on the much reduced Madelung potential at the corner site, one might assume that the electron in the oxygen vacancy would be much less tightly bound and, therefore, the ionisation potentials of the corner F and F^+ centres would be smaller than those for their surface counterparts. However, with three Mg ions exposed, the corner can be considered as three Mg corners or kinks. Due to their low co-ordination, the corner Mg ions have a higher electron affinity and attract more electron density than ions in the bulk or at the

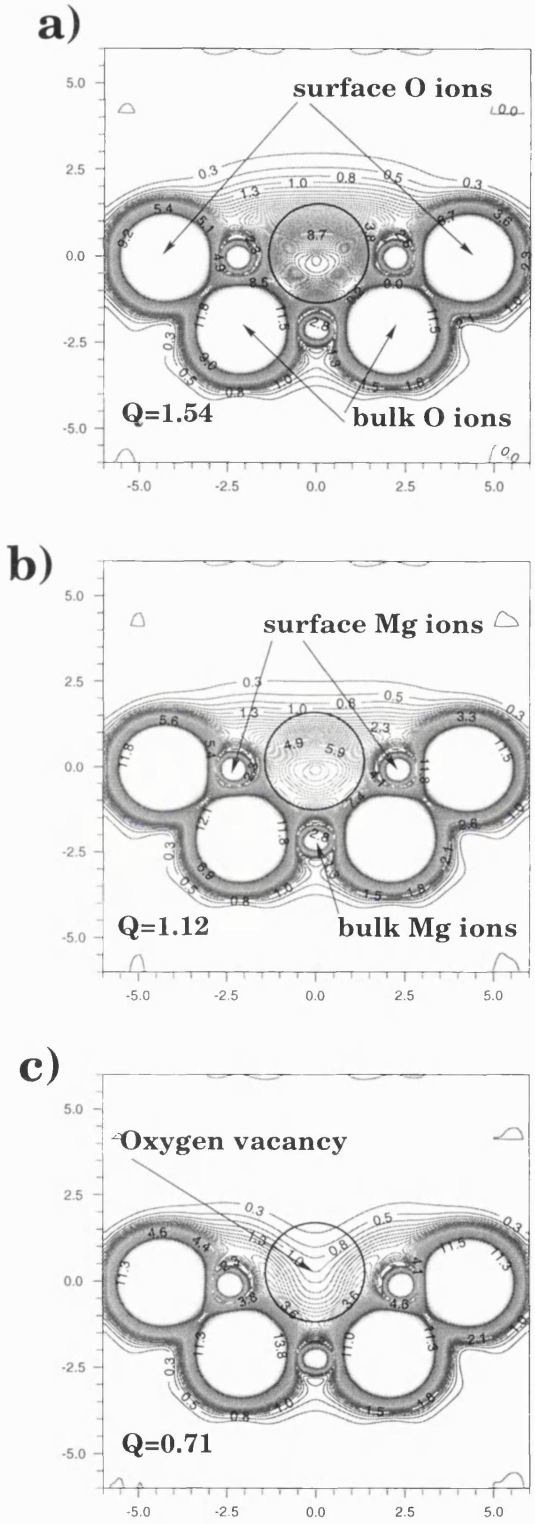

Figure 18: The electron density of oxygen vacancies at the MgO (001) surface. Plots show section through surface F centres perpendicular to the MgO (001) surface plane: a) neutral F centre; b) F^+ centre; c) anion vacancy (V_a). The circle shows the integration volume of the charge Q.

Table 23: The ionisation potentials and electron affinities of anion vacancies at the MgO (001) surface and at the anion corner of MgO.

Notation[a]	Process			Surface, eV	Corner, eV
$E_{ion}(v)$	F	$\Rightarrow$	F - e^-	3.4 (4.1)[b]	3.4 (3.7)
$E_{rel}(i)$	F - e^-	$\Rightarrow$	F^+	0.9	0.6
$E_{ion}(v)$	F^+	$\Rightarrow$	F^+ - e^-	5.6 (6.3)	6.6 (6.9)
$E_{rel}(i)$	F^+ - e^-	$\Rightarrow$	V_a	1.1	0.8
$E_{aff}(v)$	V_a	$\Rightarrow$	$V_a + e^-$	3.4 (2.8)	5.0 (4.8)
$E_{aff}(r)$	V_a	$\Rightarrow$	F^+	4.5	5.8
$E_{aff}(v)$	F^+	$\Rightarrow$	$F^+ + e^-$	1.7 (1.1)	2.3 (2.0)
$E_{aff}(r)$	F^+	$\Rightarrow$	F	2.6	2.8

[a] See Fig. 19 for notations.

[b] The energies in brackets omit the effect of the lattice polarisation.

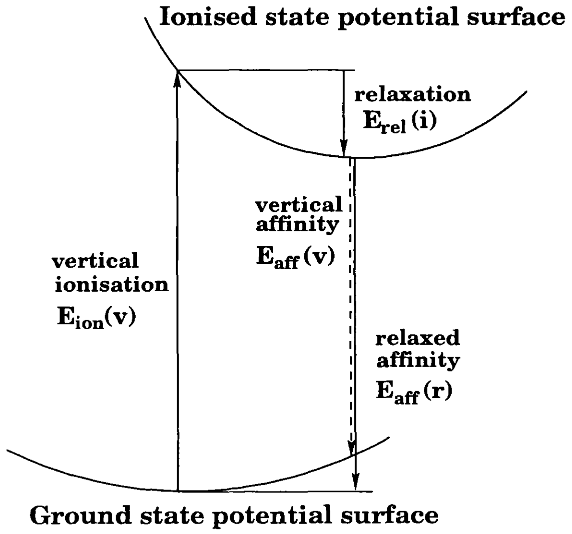

Figure 19: Schematic explanation of notations used to calculate the ionisation energies and electron affinities of different charge states of the anion vacancy at the surface and anion corner of MgO (see Table 23).

surface (see Table 22), which explains the seemingly counter-intuitive behaviour of the ionisation energy, which is almost the same for the surface and corner F centres and is larger for the corner F^+ centre.

4.1.8 Surface peroxy species

The adsorption of gas-phase oxygen at oxide surfaces plays an important part in many types of heterogeneous catalysis. Spin-resonance experiments have given firm evidence for adsorbed oxygen species such as O^- and O_2^- on some oxide surfaces [133], [198] but there is only rather weak evidence for other potentially important species such as the peroxide ion O_2^{2-}. The geometry and electronic structure calculations of the peroxide species on the surfaces and in the bulk of the oxides have been studied previously (see, for instance,

[112], [62], [161]). The questions we address here are i) what is the position of the peroxy energy level with respect to the surface valence band? and ii) where does the electron hole localise after the defect ionisation?

An oxygen atom adsorbed on the (001) MgO surface strongly interacts with the surface anion which leads to the formation of an O_2^{2-} molecule aligned approximately along the $\langle 111 \rangle$ direction (see Fig. 20(a)) with the surface anion being slightly shifted from its ideal position. The local atomic structure of the surface peroxide (see Fig. 20(a)) found in our calculations can be characterised by: i) the distance between the ions of formed O_2^{2-} molecules, which is 1.5708 Å; ii) the distance between the ad-atom and each of the two nearest cations was calculated to be 2.1013 Å; iii) the distance between the ad-atom and the next surface anion, which is 2.7285 Å and the O_1-O_2-O_3 angle (see Fig. 20(a)) of 51.01°. These geometrical parameters are in agreement with those reported in periodic DFT calculations [112].

The one-electron spectrum of the system has three states due to the bonding orbitals of the peroxy ion below the bottom of the valence band and two states due to anti-bonding orbitals just above the top of the valence band. The highest occupied orbital is approximately 0.6 eV above the top of the valence band (as calculated using one-electron energies) and is associated with the peroxy ion and a neighbouring surface anion O_3 (see Fig. 20(a)) in the $\langle 110 \rangle$ direction. There is a clear indication of charge transfer from the surface anion O_2 to the ad-atom: results of the NPA analysis suggest that about $0.75e$ is associated with the ad-atom. A similar value of the charge has been obtained by fitting the electrostatic potential of the QM cluster at the ions of the environment. This charge distribution agrees well with previous calculations [112].

The calculated values of the ionisation potentials with (IP(I)) and without (IP(0)) contribution of the electronic polarisation of the environment are 6.3 eV and 7.0 eV respectively. As in the case of oxygen vacancies, a large difference between the IP(0) and IP(I) suggests that polarisation of the host lattice can not be neglected if processes involving change in the defect charge state are considered. Comparison of the IP(I) with the ionisation potential of the ideal surface (see 4.1) shows that the defect energy level is only 0.2-0.4 eV above the top of the valence band. Such a small separation between the defect level and the surface valence band implies that the valence band states may be mixed with the defect states and, therefore, modelling of this defect on its own, without valence band states included, may be unreliable.

Plots of the spin density of the system after "vertical" ionisation (see Fig. 20(b,c)) demonstrate that most of the hole is associated with the surface anion O_3 (see Fig. 20(a)) rather than with the peroxide ion. Indeed, the peroxide molecule is tilted towards the anion bringing an additional negative contribution to the Madelung potential at that site and destabilising its electronic states. The plots also demonstrate that the hole is partly delocalised over other surface anions.

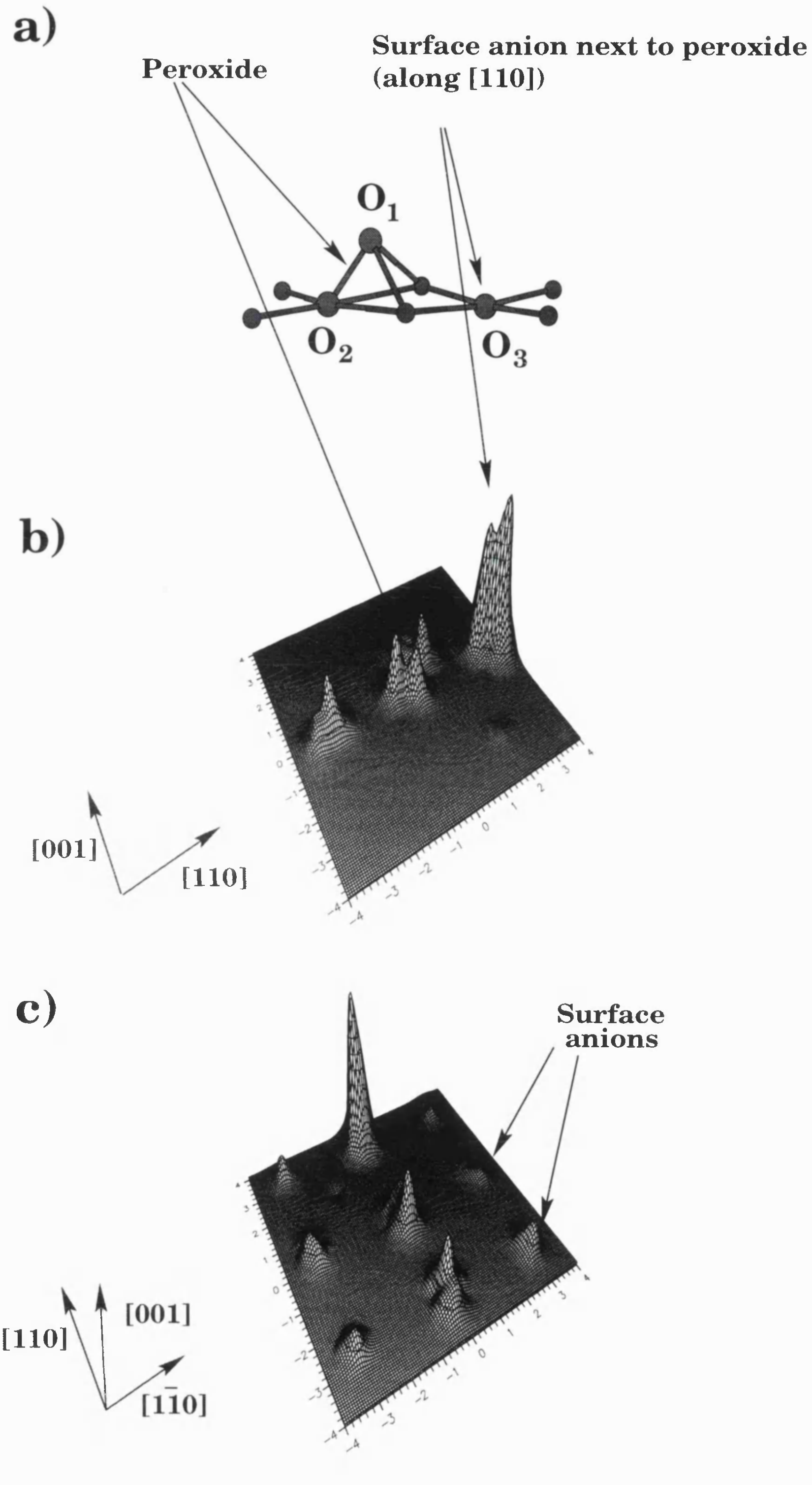

Figure 20: Peroxy ion at the MgO (001) surface.
a) local geometry; b) spin density after vertical ionisation (section perpendicular to the MgO (001) surface plane); c) spin density after vertical ionisation (MgO(001) surface plane, top view). The strong peak in plots b) and c) is associated with surface anion marked O_3 in plot a).

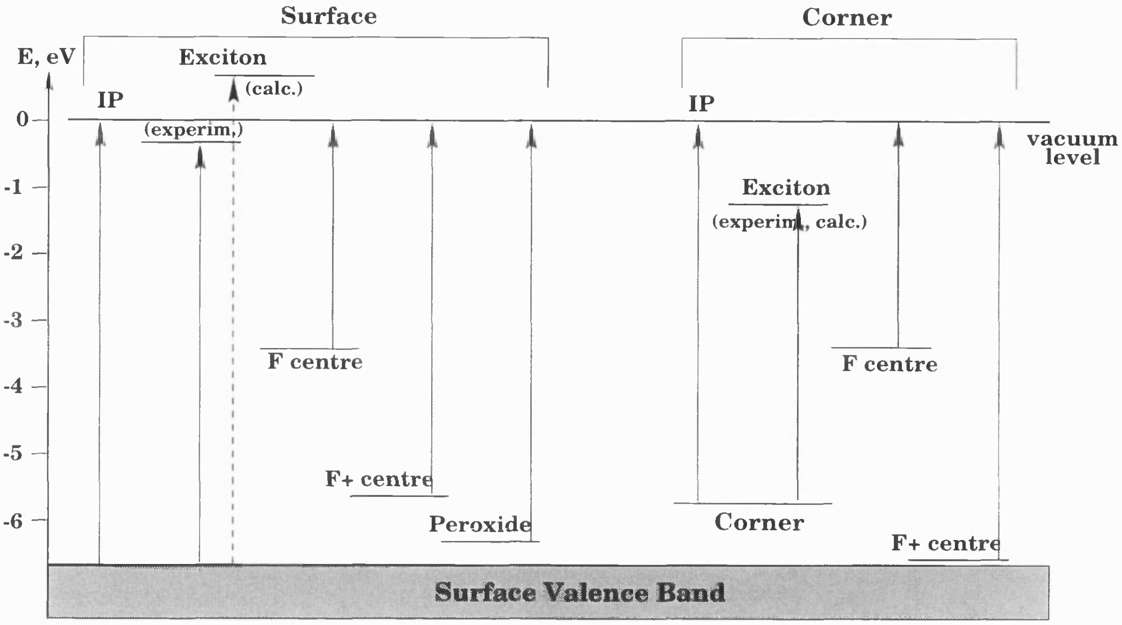

Figure 21: Positions of the defect and excited states with respect to the vacuum level and to the top of the surface valence band.

4.1.9 Discussion

The result of this section are summarised in Fig. 21. The calculated position of the surface valence band with respect to the vacuum level at about 6.7 eV is in good agreement with the MIES [114] predicting 6.7 ± 0.4 eV. Analysing the results of the UPS measurements on MgO crystals Tjeng *et al.* [209] obtained the value 9.1 eV for the position of the top of the valence band with respect to the vacuum level (see 4.1.1). Although the issue is still controversial, we consider that the value 9.1 eV suggested in [209] for the position of the top of the valence band is too large.

The results presented in Fig. 21 suggest that the energy of the neutral F centre at the top surface layer should be about 3 eV above the top of the valence band, which is in fair agreement with the results of periodic DFT calculations [113] which predict 2.3 eV for this value. Our results also predict ionisation of the surface and corner F centres if the irradiation energy exceeds 4.0 eV. These centres represent two extreme cases with many other possibilities in between, such as F centres at surface steps and kinks, which can be expected to have similar properties, which can also be useful to bear in mind when analysing the results of laser induced processes at MgO surfaces. In particular, surface irradiation with 266 nm or 248 nm laser light can ionise these states leading to photoemission and the formation of charged F^+ centres. The predicted electron affinities are useful, for example, when analysing the results for thin MgO films on metal substrates, especially with an applied voltage. With the Fermi level of many metals at about 4-5 eV, some of these states can be filled in by metal electrons.

Finally, we stress the importance of having the right balance between the ionisation potential of adsorbed species and the surface or defect electron affinity. Many calculations of adsorption are based on a cluster model of a surface. In this case, the adsorbing species is always better described than the surface since the basis set, pseudopotentials and functionals are optimised to reproduce the ionisation potentials of atoms and molecules with respect to the vacuum (see, e.g. [15], [16]). However, if the crystalline potential and polarisation effects within the surface are not taken into account properly, this can lead to inaccurate surface ionisation potential and, hence, to unrealistic charge transfer between the two. The results of this section demonstrate one of the possible ways of achieving an accurate balance. They also provide quantitative parameters for the electronic structure of the perfect and defective MgO (001) surface, which can be useful in further studies of adsorption and photo-induced processes.

4.2 Electronic structure of excited states at low-coordinated MgO surface sites

In recent years, there have been many studies aimed at determining more precisely the nature and properties of oxide surfaces. There is growing evidence that chemical and spectroscopic properties of surface sites depend on their coordination. In particular, spectroscopic studies ([35], [80], [221]) demonstrated that highly dispersed alkaline earth oxides have optical absorption bands (5.7 - 2.6 eV) which are not present in the pure single crystals. Different bands in the spectrum of each oxide have been associated with ions having different coordination at the surface. In this section we present the results of our studies of the electronic structure of optically excited states at low-coordinated sites of the MgO nano-cluster: oxygen corner, cluster edge and terrace, which confirm this assignment.

4.2.1 Experimental background

Coluccia *et al.* [34], [36], [33], [35] have studied optical properties of two MgO materials in which the relative proportion of ions having low coordination should be different. In particular, thermal decomposition of an hydroxide (or carbonate) yields MgO crystallites of a plate-like relic structure, which contains a number of high index planes and MgO smoke, formed by burning of Mg in the air, which contains nearly perfect small cubes. They have measured the reflectance and photoluminescence spectra and demonstrated a clear correlation between these spectra and abundance of particular surface features. The main feature of the photo-luminescent spectra relevant to the current discussion is the ratio between the intensities measured at the maxima of the emission spectra excited at 4.52 eV and 5.40 eV: $I_{4.52}/I_{5.40}$. In the MgO prepared by thermal decomposition, values of $I_{4.52}/I_{5.40}$ close to 1.6 were observed. In contrast, for MgO smoke in its original condition, the ratio was typically 0.3. After MgO smoke has been in contact with water and then out-gassed, the ratio $I_{4.52}/I_{5.40}$ changed to 1.3, i.e. much nearer to the value found for MgO-ex carbonate. The reflectance spectrum of the MgO smoke after water treatment shows a broad shoulder at 275 nm (4.50 eV) which was absent in the spectrum of the original smoke but was present in the original spectrum of MgO-ex carbonate. Micrographs taken at different prolongations of water attack on MgO smoke reveal that the eroded regions of the particles show a terraced structure with steps down to the size of 2-3 unit cells. Based on these observations, Coluccia *et al.* concluded that the changes in optical behaviour of MgO smoke are due to the appearance of a larger number of ions of three- and four-fold coordination on the surface and assigned absorption bands at 5.75 eV to the step edges and at 4.62 eV to the kink and corner sites. Similar features have been observed in the excitation and emission spectra of other cubic oxides: CaO, SrO and BaO. Similar experiments have been performed by Zecchina *et al.* [80], [221]. These authors have studied the ultraviolet reflectance spectra of the micro-crystalline MgO and observed additional bands at 5.7 eV and 4.6 eV which have been attributed to the low-coordinated sites: step edges, kinks and corners.

4.2.2 Details of calculations

We applied the embedded cluster method described above to study the optical properties of low-coordinated surface sites [192], [204]. This modelling is an example of a problem where the finite nano-cluster approach finds a straightforward application.

The characteristic size of the small MgO smoke cubes used in [36] was about 10-100 nm. At the time we could not afford direct modelling of such large systems. Instead, we used a stoichiometric cubic nano-cluster of 6×6×6 ions (216 ions in total) with an edge length of about 1 nm. The geometry of the nano-cluster was calculated using the atomistic simulation technique and the GULP [79] code and then kept fixed in all calculations of this series. We employ a simple embedded cluster approach in which the QM cluster is embedded into a distribution of point charges representing ions of the finite nano-cluster. As usual, the interaction of the point charges with the QM cluster was included using the standard procedure [71] in which the matrix of potential energy, including both diagonal and non-diagonal elements, is added to the Fock matrix. Different QM clusters (Fig. 22) have been used to simulate MgO terrace, step edge and corner sites as well as to check the dependence of the results on the size and form of the QM cluster. In order to prevent artificial delocalisation of the diffuse electronic states, the nearest and next-nearest cations surrounding the QM cluster carried the Effective Core Pseudo-potential of Wadt and Hay [216]. Two Gaussian type basis sets, defined as A and B, have been used. Basis A is a standard 6-311+G basis set from the Gaussian98 library. It includes 14s and 10p primitive functions contracted into 7s and 6p basis functions for Mg ions and with similar (12s,7p)⇒(5s,4p) contraction for O ions. Basis B was developed by Bagus *et al.* in [95] and [22] and used in calculations of the excited states of bulk MgO [9]. This, more contracted, basis consists of (10s,6p)⇒(6s,4p) and (9s,5p)⇒(4s,3p) functions for Mg and O ions respectively. The latter oxygen basis set was optimised for the O^- ion which might be beneficial for the calculation of the excited states.

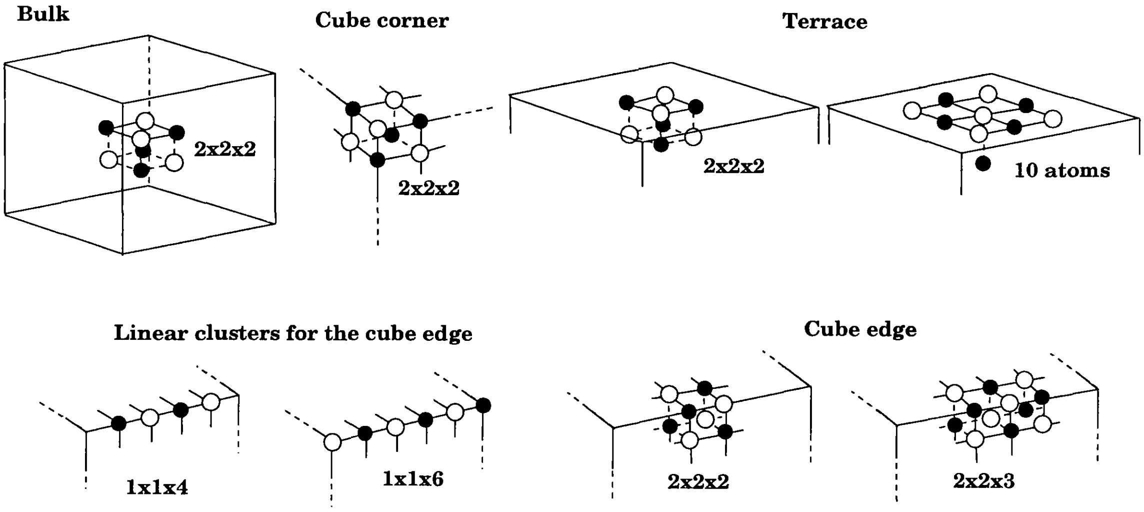

Figure 22: Schematic illustration of quantum mechanical clusters used in calculations of excitation energies of low-coordinated sites.
The clusters are embedded into a 6×6×6 (256 ions) nano-cluster; open circles are oxygen ions, filled circles are magnesium ions.

The energies of the ground states have been calculated using the Hartree-Fock method. The excitation energies have been calculated using two techniques: i) the configuration interaction method with single electron excitations (CIS) and ii) as a difference between the total energies of the singlet and the triplet states of the system calculated using the configuration interaction method with single and double electronic excitations (CISD) from the reference HF wave function.

4.2.3 Results and Discussion

The shape of the relaxed nano-cluster is slightly rounded with respect to the ideal one. The interatomic distances are smallest at the corner sites and largest in the middle of the nano-cluster. For comparison, the anion-cation distance is 1.91 Å at the anion corner and 2.05 Å in the middle of the cluster. For the same shell model, the anion-cation separation in the bulk of the ideal crystal is 2.105 Å.

The calculated excitation energies are summarised in Table 24. The CIS technique provides the whole spectrum of excitation energies, both for singlet to singlet (S→S) and singlet to triplet (S→T) transitions. The S→S transitions in Table 24 have the largest oscillator strength. Corresponding S→T transitions and splitting between the S→S and S→T transitions are also given. The CISD technique provides only S→T transitions from the ground singlet state to the lowest triplet state. The spin density distributions in these states are similar to those obtained for the CIS S→T transitions quoted in Table 24, which justifies further comparison of these transition energies.

We can immediately see a trend: irrespective of the basis set, the excitation energies into the singlet and triplet states gradually decrease as the coordination of the oxygen ion decreases. At high coordinations, the excitation energies calculated using the basis

Table 24: The excitation energies (eV) for different sites in the cubic $(MgO)_{108}$ nano-cluster calculated using CIS and CISD techniques.

	QM cluster	Number of	Basis[b]	CIS			CISD	
N[a]	position	atoms (Fig. 22)	set	S → S	S → T	Δ_{ST}	S → S	S → T
6	bulk	8	A	8.9	8.9	0.0	7.5	7.5
5	terrace	8	A	7.1	7.8	0.7	6.4	7.1
4	edge	8	A	6.1	6.8	0.7	5.0	5.7
		12	A	6.1	6.9	0.8		
		6	A	5.6	6.1	0.5		
		4	A	5.6	6.5	0.9		
3	corner	8	A	5.3	5.8	0.5	4.0	4.5
6	bulk	8	B	11.3	12.3	1.0	10.7	11.7
5	terrace	8	B	7.9	8.7	0.8	7.1	7.9
4	edge	8	B	7.3	7.9	0.6		
3	corner	8	B	5.5	6.1	0.6	4.3	4.9

[a] N - is the lowest oxygen atom coordination number.
[b] See text for description of basis sets.

set B are much larger than those obtained using the basis A. The difference between the two basis sets becomes much smaller for the edge and corner, where the anion electronic configuration is closer to the O^- ion configuration used to optimise the basis set B. We can see that the singlet-triplet splitting for the excited states also depends on the basis set, coordination and the size of the cluster. Finally, the excitation energies of S→T transitions calculated using the CISD method are much lower then their CIS counterparts revealing the importance of electron correlation.

In four cases, the QM cluster was a cubic Mg_4O_4 cluster embedded at different positions inside the nano-cluster. The disadvantage of this cluster is that its ions are treated differently when the position of the cluster changes from the lowest to the highest coordination sites. For example, at the corner site the oxygen corner anion is coordinated by quantum-mechanically treated all-electron cations; while at the surface site, each of the two surface anions is surrounded by three all-electron cations and two bare pseudopotentials without basis functions. To check whether this factor can significantly affect the results we have considered two larger clusters, one at a terrace and the other at a step edge, in which each anion was coordinated with five and four full electron cations respectively. Excitation energies calculated for these clusters differ from those calculated for cubic QM clusters by only 0.1 eV. At the edge we have also considered two linear clusters comprising four and six ions. These produced excitation energies as much as 0.5 eV different from those for cubic cluster.

To understand the character of the electron distribution after the vertical excitations, we analysed the total density and spin density maps calculated using different methods. It is important to note that the density maps obtained with UHF, CIS and CISD techniques are very similar. The sections of the spin density for the corner and edge are shown in Fig. 23. We see that in both cases, the unpaired electrons are mostly localised in the vicinity of the low-coordinated anion and in the free space outside the QM cluster. To provide a quantitative insight into the nature of the spin density distribution, these pictures should be supported by an additional analysis, which has been undertaken by means of integrating the spin density within spheres centred at different sites inside QM clusters. The accumulated charge as a function of radius for spheres centred on the corner and edge oxygens is shown in Fig. 24. Combined with similar curves for integration spheres centred at other QM atoms, it proves that for the corner, the hole is strongly localised on the corner oxygen and the excited electron is spread out of the corner around the hole. For the edge, again, the hole is mostly localised at the oxygen ion which has the lowest coordination whereas the excited electron is spread around the hole outside the cluster. To check how the localisation of the hole at the edge depends on the number of anions at the edge we calculated the spin density for the linear cluster Mg_2O_2 representing a "longer" edge. In this cluster both oxygen ions are equally coordinated and almost equivalent. Accordingly, there are two almost degenerate transitions and the spin density for each of them is close to that shown in Fig. 23(b). The fact that the two excited states are almost degenerate indicates that for a longer edge the hole and electron components of the exciton are expected to be delocalised over several oxygen ions. This is indeed the case for the terrace: the two oxygen ions in the quantum cluster are equivalent and the excited state is delocalised and equally associated with both of them. As for the cases of lower coordination, the excited electron extends perpendicular to the surface plane into free space. We should note that in all cases our analysis demonstrates no significant spin density near magnesium ions.

Finally, we should discuss the issue of the relative values of the total energies of the excited states at different low coordinated surface sites. These could be used as an indicator of whether the exciton, created for instance in the bulk or at the surface, would transfer to the less coordinated edge or corner. Calculation of these relative energies for different clusters requires a certain reference energy level to be determined. We take the vacuum level as the reference, and energy levels of quantum clusters at different surface sites with respect to the vacuum level are defined as their ionisation potentials. There is not much difference between the ionisation energies calculated for different clusters at the same location. For example, the ionisation potential of the eight atom cubic cluster at the edge site was found to be 8.06 eV whereas the IP for the 12 ion edge cluster was 8.07 eV. However, we note that these ionisation energies are overestimated by 2.0-2.5 eV because the electron polarisation of the nano-cluster was not accounted for in the ionised state. The positions of the exciton levels with respect to the top of the valence band (see 4.1.4) are shown in Fig. 21.

Assuming that the vacuum level is common for all the systems considered, we place the ground state of each system at -IP, as shown in Fig. 25. Then the position of the

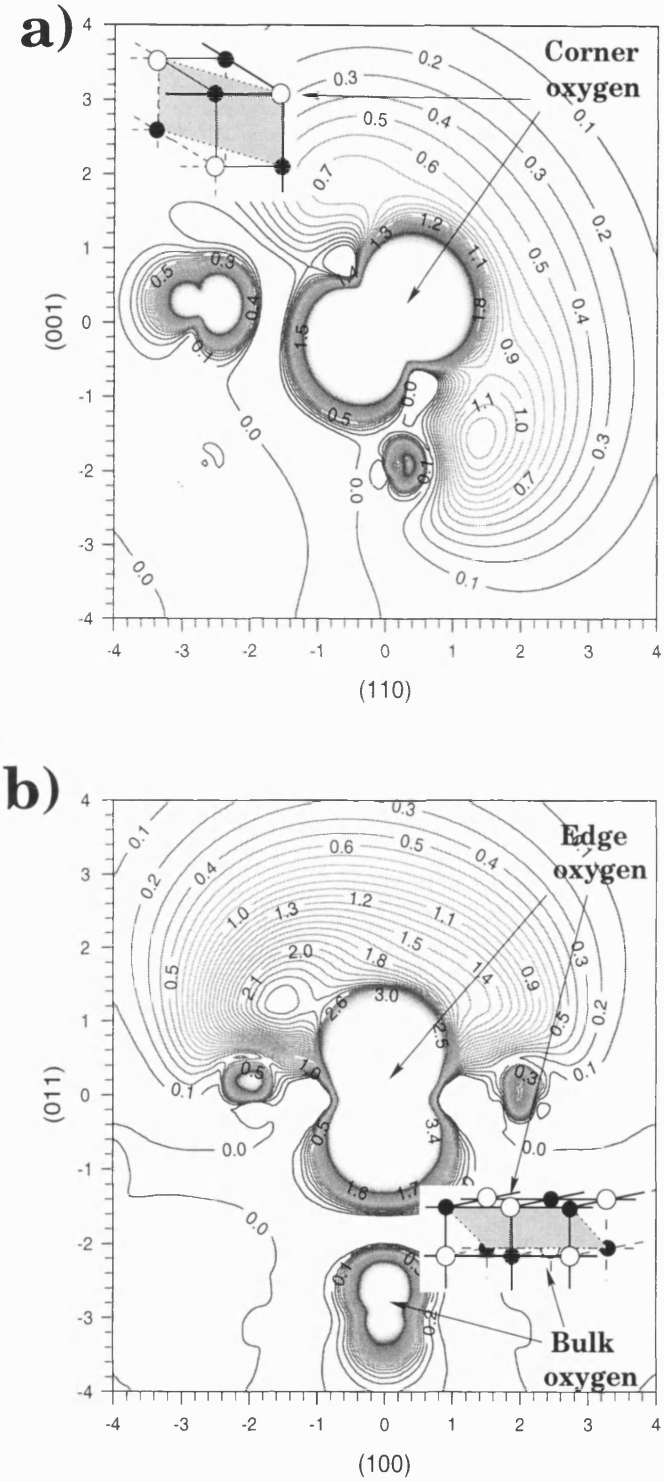

Figure 23: The spin density of excited triplet state of 3- and 4-coordinated anion sites at MgO (001) surface.
a) section of the spin density at the corner site (see Fig. 22); b) section of the spin density at the edge site (see Fig. 22).

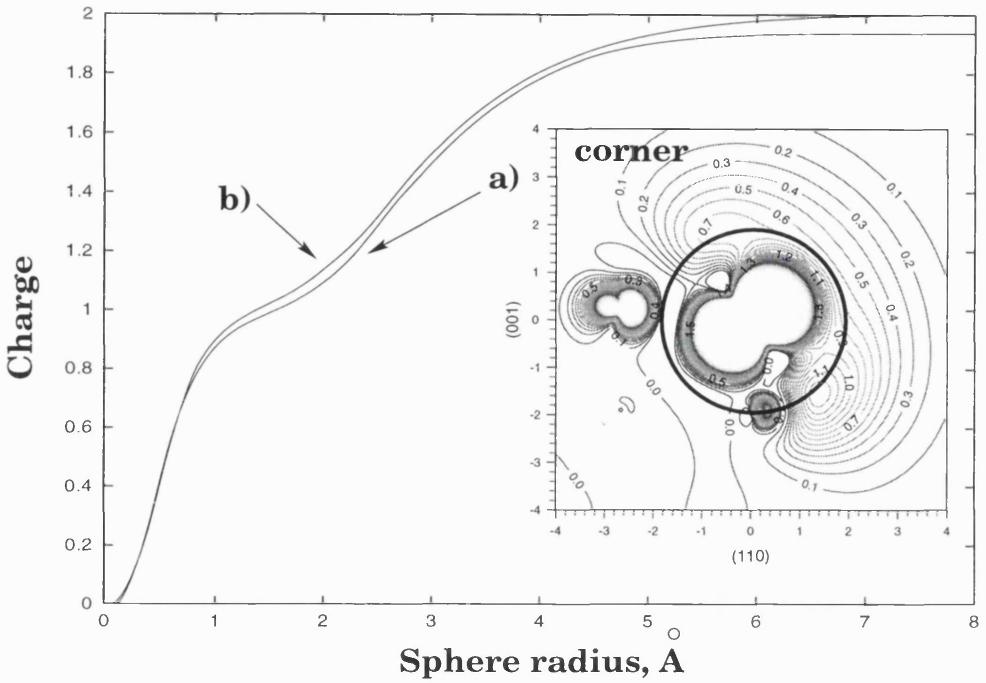

Figure 24: The spin density of the excited triplet state integrated inside a sphere. a) for the corner oxygen ion; b) for the edge oxygen ion. Note that one unpaired electron is located inside the sphere with radius ≈1.5 Å, which approximately corresponds to the oxygen radius, whereas the second electron is spread over a much larger region.

energy level of a system in its excited state was defined with respect to the ground state energy level for each system. As one can see, the excited state in the bulk has much higher energy than that at the surface and the latter is higher than at the edge. The energy levels of the excited states at the edge and at the corner appear to be very close. These energy levels (shown with solid lines in Fig. 25) are too low because the polarisation response of the nano-cluster was not taken into account for both the ionised and excited states. Using the results of the previous section we can correct these energies for the polarisation of the environment for the terrace and the corner states. Ionisation potentials for the terrace and for the oxygen corner calculated including polarisation effects are 6.7 eV and 5.6 eV respectively. Corresponding excited state levels are shown with dashed lines in Fig. 25.

The strong dependence of the excitation energies on ion coordination is due to the combination of several interrelated factors. These include the reduction of the Madelung potential at low-coordinated sites and the consequent substantial atomic relaxation of the low-coordinated sites with respect to their ideal geometry and reduced ionicity. Moreover, as is partly demonstrated by our calculations, the excitation energy, degree of localisation and the nature of the excited state depend on the site location and details of its local environment.

We can now summarise the results of our calculations. First, irrespective of the basis set used, a consistent dependence of the excitation energies on the oxygen coordination, n

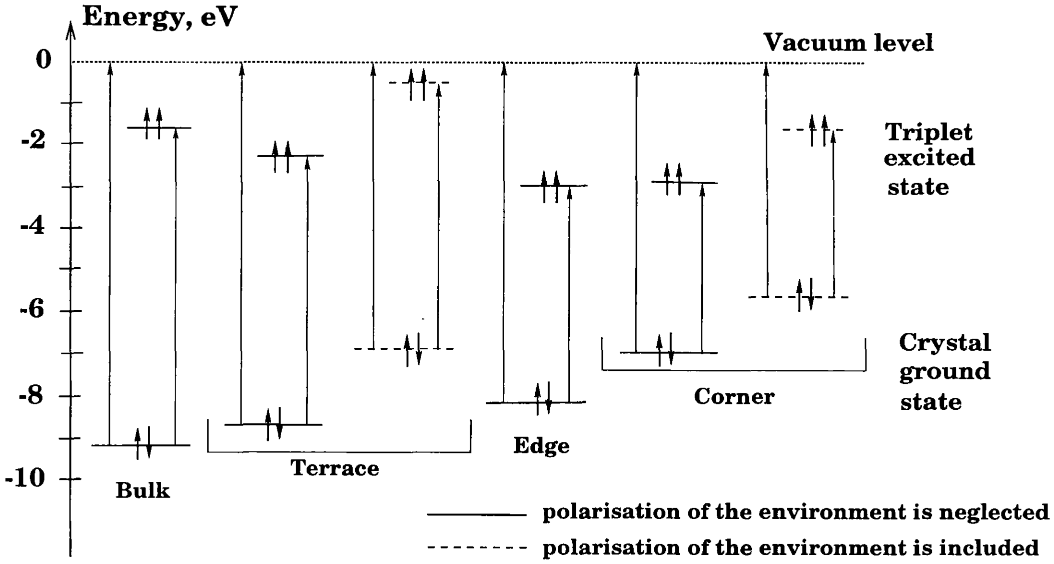

Figure 25: The relative energies of the ground and excited states at different positions in the nano-cluster. The energies are calculated using the CISD method.

= 3, ...6, was demonstrated. The excitation energies differ by ca. 1 eV for the sites with Δn = 1, which is close to the experimental results [80]. If we assume that the singlet-triplet splitting is little affected by electron correlation, we can roughly estimate the energies of the correlated singlet-singlet transitions For this purpose we use the S-T splitting calculated using the CIS method and S→T excitation energies calculated using the CISD method. Estimated energies of S→S transitions are then $E(S \rightarrow S) = E_{CISD}(S \rightarrow T) + \Delta_{ST}$. The excitation energies obtained in this way are in agreement with the experimental data for the bulk [171] and for the surface [38], and also support the assignment of the peaks at about 5.7 and 4.6 eV to the four- and three-coordinated oxygen surface sites respectively [80]. Second, the analysis of the total and spin density distributions in the excited states demonstrates the strong contribution of the oxygen states to the excited state and the almost negligible contribution of magnesium states, which does not agree with the traditional point of view that the bottom of the conduction band in ionic insulators is mainly determined by cation states. This result, however, is supported by earlier calculations by Pandey *et al.* [152] who found a complete exciton localisation on the oxygen ion in the bulk of MgO (see also discussion at the end of 4.1.5). Third, the excited state appears to be more localised at the terminating three-coordinated oxygen sites than within the edge or at the terrace. The relative energies of the excited states corresponding to oxygen sites of different coordination suggest the possibility of the excitation to transfer from, for example, the surface to the terminating site with the lower energy. The reduction of the ion coordination in ionic materials leads to significant changes in the crystalline potential which has been related to the chemical and spectroscopic properties of the low-coordinated surface sites.

5 Processes at the surfaces of ionic crystals

So far, we have considered defects at surfaces and in the bulk of MgO and NaCl crystals and have attempted to characterise these defects by studying their physical properties. The present Chapter is concerned with modelling of mechanisms of processes involving several of such defects.

Two types of processes have been studied. The first is directly related to the extensively explored field of laser induced desorption of ions and molecules from surfaces. We will describe recent experiments, which have stimulated the present work, together with existing theoretical models as well as the results of our modelling. The second type of a process is related to scanning force microscopy (SFM) experiments. Interpretation of SFM images often relies on intuitive ideas about the structure of the probe tip and the surface. In fact, depending on the details of the experimental procedure, modification of both tip and the surface can occur, which affects the interaction and resulting image. We investigate the possibility of the tip contamination by the surface material with an example of the interaction of a silicon tip with the NaCl (001) surface. The question of charging of both tip and the surface as a result of the interaction is also considered.

5.1 Laser induced desorption of Mg^+ ions from the (001) MgO surface

Laser induced ion desorption from insulators with excitation photon energies less than the band gap and fluences below the damage threshold is frequently observed [178], [49], [61]. Studies of laser induced ion emission from ionic materials demonstrate that the photon fluence dependence of the ion yield is a nonlinear function, which is often described by a power law, and that multiple photon processes as well as defects are involved in the excitation step [61], [48]. The mechanism of ion emission and the energy distribution of emitted ions are still subjects of debate and further investigation even for ionic crystals such as alkali halides or alkali earth oxides. In section 5.1.1 we outline the idea of the laser-induced ion desorption experiments and the experimental set up. Then we describe specific results of an experiment relevant to the present work (section 5.1.2) and a simple electrostatic model which was suggested to rationalise those results (section 5.1.3). Other theoretical models will be also outlined in that section. Details and results of our embedded cluster calculations, aiming to check whether assumptions made in the electrostatic model are correct, are described in sections 5.1.4 and 5.1.5 respectively, followed by the discussion and conclusions in 5.1.6.

5.1.1 The process of induced desorption and general experiment

The process of laser induced ion desorption is schematically shown on Fig. 26. A specially prepared sample of MgO or LiF is irradiated by the laser beam at the energies lower than the band gap: usually standard 5 eV (248 nm) laser is used. Masses and velocities of desorbed ions are monitored using a mass spectrometer. A standard qualitative explanation

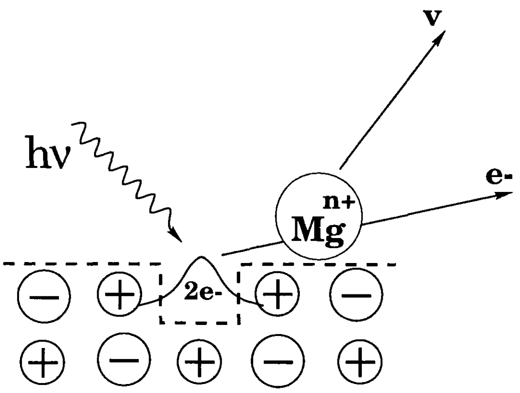

Figure 26: Process of laser-induced desorption of Mg ion from a surface containing a neutral F_s centre (schematic representation).
Ionisation of the centre F_s "turns on" repulsive electrostatic interaction and causes desorption of the cation.

of the ion emission is the following. If the sample contains large number of defects at the surface or in its vicinity, the 5 eV photons can ionise these defect centres. The emission of electrons leads to an increase of the Coulomb repulsion energy in the sample which, in turn, leads to desorption of positive surface ions. Measurements of the kinetic energies of the desorbed ions and their mass distribution or time of flight (TOF) can provide information about the structure and morphology of the surface and the mechanisms of the desorption process. Simultaneous analysis of the kinetic energies of the emitted electrons also gives additional information concerning the nature of the surface defects, in particular their ionisation energies.

The details of the experimental setup can vary. For this reason we mention only its most general features. Experiments are conducted in a UHV chamber. The electron emission is detected by an electron multiplier. Emitted electrons reach the multiplier in about 20 ns after the laser pulse and start to develop a characteristic peak. The area under the resulting electron peak is taken as the photoelectron yield from the surface. Ion TOF measurements are done using a quadrupole mass spectrometer (QMS). The region between the sample and entrance to the QMS (of the order of 15-20 cm) is kept field free so as to eliminate perturbation to the direct flight of ions to the QMS detector. The angular distributions of the desorbed ions can be determined by fitting the patterns on the phosphor screen with the ion trajectories. To prevent charging of the sample, its substrate is irradiated by electrons; to avoid the effects of modification of the sample surface, observations should be made within short period of time; then the laser beam should be moved to another spot of the sample's surface.

5.1.2 Experimental and theoretical background

A recent series of experiments performed by Dickinson *et al.* [49] aimed to study photodesorption of positive ions from the surfaces of ionic crystals. Due to its relative simplicity, the MgO (001) surface has been extensively studied in those experiments. It was noted that different ions are desorbed depending on the surface pre-treatment. In particular, in addition to Mg^{+} desorption, weaker contributions of Mg^{2+} and MgO^{+} and $\mathrm{Mg_2O}^{+}$ have been observed from the polished MgO (001), whereas only Mg^{+} were desorbed from the cleaved surface. The TOF distributions for both Mg^{+} and Mg^{2+} ions, desorbed from the polished surface, have a characteristic double peak shape suggesting that the emitted ions have two most probable energies for each ion type. To facilitate numerical analysis, the TOF curves were fitted assuming that the energy distribution could be empirically expressed as a sum of two Gaussian type functions. The TOF distribution has, therefore, the form:

$$I(t) = \frac{md^2}{t^3}\left\{N_1 exp\left(\frac{-(E_1-E)^2}{2\sigma_1^2}\right) + N_2 exp\left(\frac{-(E_2-E)^2}{\sigma_2^2}\right)\right\},$$

where N_1, N_2, E_1, E_2, σ_1 and σ_2 are model parameters and $E(t)$ is the ion kinetic energy ($= mv^2/2 = md^2/2t^2$) corresponding to the time of arrival t and flight path distance d. This empirical form provides very good representation of the experimental data. The most probable energies E_1 and E_2 were 2 and 7.9 eV for Mg^{+} and 6.7 and 18 eV for Mg^{2+} with the error bars on these numbers being ±1 eV. Within this uncertainty, the energy distributions displayed no shift with laser fluence over a range of 0.1 to 2 $\mathrm{J/cm}^2$.

5.1.3 Electrostatic model

On the basis of the relatively high kinetic energies and the substantial shift to higher energies for Mg^{2+} vs Mg^{+}, an electrostatic ejection mechanism triggered by the incident 5 eV photons was suggested [49]. The proposed model was based on the assumption that the emission of Mg ions occurs from the positions above surface F_s and $\mathrm{F}_s{}^{+}$ centres after ionisation of the latter. The two positively charged defects, $\mathrm{F}_s{}^{+}$ and $\mathrm{F}_s{}^{2+}$, serving as repulsive centres combined with the two ionic charges (Mg^{+} and Mg^{2+}) could produce the four observed kinetic energy peaks. Simple electrostatic energy calculations of the binding energies for all four ad-ion/F_s centre combinations assuming bulk interionic distances have been performed in [134]. These calculations accounted for the additional negative image charge resulting from the polarisation of the MgO due to the charged defects. The calculated final kinetic energies were as follows: $\mathrm{Mg}^{+}/\mathrm{F}_s{}^{+}=$ 4.4 eV, $\mathrm{Mg}^{+}/\mathrm{F}_s{}^{2+} =$ 11.2 eV, $\mathrm{Mg}^{2+}/\mathrm{F}_s{}^{+} =$ 6.0 eV and $\mathrm{Mg}^{2+}/\mathrm{F}_s{}^{2+} =$ 19.6 eV. It was also suggested that the ionisation of the initial $\mathrm{Mg}^{2+}/\mathrm{F}_s$ system might not occur directly but via one or several intermediate steps. The photo-induced charge exchange transition of the form $F_s + Mg^{2+}(ad-ion) + \hbar\nu \Longrightarrow F_s^{+} + Mg^{+}$ may serve as an example of one of these steps. Ionisation from this excited state would generate the $\mathrm{F}_s{}^{2+}$ repulsive centre acting on an Mg^{+} ion.

5.1.4 Theoretical modelling

Aim of the modelling. The model proposed by Dickinson *et al.* includes a number of arguments which we summarise as follows: i) a surface defect centre formed by an Mg^{2+} ad-ion positioned above a neutral surface F_s with both electrons localised in the oxygen vacancy is stable; the distance between the vacancy and the Mg^{2+} ion sited above is close to the interionic distances in bulk MgO; ii) 5 eV photons can either ionise this centre from its ground state or excite and then ionise the centre from its excited state; iii) the resulting kinetic energy of the Mg^+ ion electrostatically repelled by the surface ${F_s}^{2+}$centre is as large as 11 eV. In this work we aim to check these assumptions. For this purpose we employ the embedding cluster approach and consider a three stage process: i) adsorption of a neutral Mg atom at the anion vacancy at the MgO (001) surface with the formation of a specific model centre, ii) ionisation of the centre, and iii) subsequent desorption of the Mg^+ ion from the surface. The issues we address are: i) what is the electronic structure of the surface centre formed? ii) what is the value of the ionisation energy of this centre and are one- or two-photon absorption processes required to remove the electron from the system? iii) is the energy acquired by the desorbed ion comparable with the experimental value? The results in this section should be considered as preliminary. The necessary future studies are outlined at the end of the section.

The generally low yield of the desorbed ions (about 100 ions per 10^{15} photons even for high concentrations of surface or near surface defects) suggests that multi-step and/or low probability processes, like ionisation from excited states, are involved in the desorption mechanisms. This issue has been left out of the scope of the present work.

Details of the calculation. We employ a finite nano-cluster model (see Chapter 2) for the (001) MgO surface. The total size of the nano-cluster and the size of the shell model region have been 8×8×4 and 6×6×3 ionic centres respectively. The QM cluster was embedded at the centre of the surface. We used close to the smallest possible QM cluster, which included an anion vacancy surrounded by five cations treated using a full electron basis set and twenty cations with a bare Effective Core Potential (ECP). To increase the quality of the calculation, floating basis functions have been added to the anion vacancy. No charge compensating cation vacancy has been included in the present model. In total, the basis set included 7sp uncontracted basis functions for the anion vacancy, a standard 6-311G basis set for the Mg ad-atom, a 6-31G basis set for the surface cations nearest to the vacancy and an ECP developed by Wadt and Hay [216] for the other cations in the QM cluster.

5.1.5 Results of calculations

As mentioned above, there are three stages into which the process of adsorption and desorption can be separated. Each stage corresponds to one of the assumptions which we aim to check. We consider all these steps separately.

I) Adsorption of the Mg atom on the surface anion vacancy. We have calculated the adiabatic potential of the Mg atom as it approaches the vacancy along the direction perpendicular to the surface. All ions of the inner region have been relaxed at every position of the ad-atom. The adiabatic potential has a minimum at 2.7 Å from the ideal surface plane which is *ca.* 0.6 Å larger than the anion-cation separation in the bulk MgO. The binding energy corresponding to this distance is 2.74 eV. It is an important and, perhaps, crucial fact that the structure of the centre formed is far from an intuitive picture of an Mg^{2+} ion being on the top of the neutral F_s centre. In fact, according to Natural Population Analysis, only $0.1e$ can be associated with the anion vacancy. At the same time the charge of the Mg ad-atom is close to +0.15. This suggests that the two valence electrons of the Mg ad-atom are only polarised towards the anion vacancy, but there is no clearly manifested charge transfer from the ad-atom. These results are confirmed by periodic DFT calculations [114] in which the adsorption of the neutral Mg atom on the (001) MgO surface in the vicinity of the anion vacancy was studied. It was found that: i) the most stable configuration of the Mg atom is not on top of the anion vacancy but closer to a surface anion in $\langle 110\rangle$ direction from the vacancy: the x, y, and z coordinates of the ad-atom with respect to the anion vacancy are 1.4 Å, 1.4 Å, 2.4 Å respectively; ii) valence electrons of the adsorbed atom are only polarised towards the vacancy. We can conclude that the first assumption of the model (section 5.1.3) was not confirmed by either embedded cluster or periodic calculations: i) the adsorbed atom occupies a site that is not on top of the vacancy but is displaced towards the surface anion; ii) the optimal ad-atom - vacancy distance for the atop site was found to be 2.7 Å which is 0.6 Å larger than the distance assumed in the model; iii) the defect formed is not F_s/Mg^{2+} but rather ${F_s}^{2+}/Mg$, i.e. there is no significant charge transfer between the adsorbed Mg atom and the anion vacancy.

II) Ionisation of the defect centre. The ionisation potential of the ad-atom - vacancy system was calculated as described in Chapter 2. NPA analysis of the electron density of the ionised state clearly indicates that the charge state of the ad-atom becomes Mg^{+} while the anion vacancy remains unoccupied. The value of the ionisation potential was found to be 11.4 eV. In a view of our previous results concerning position of the top of the valence band with respect to the vacuum level (Chapter 4), this value for the IP is unexpectedly large and requires additional discussion. First, let us note that the ionisation potential of the free Mg atom is close to 7.6 eV. When the atom approaches the surface above the anion vacancy site, its IP should increase due to stabilisation of the electron states in the positive electrostatic potential of the vacancy. Consequently, one-electron states due to the ad-atom valence electrons are expected to be close to the top of the MgO valence band or appear as resonances. In the latter case, laser induced emission of an electron should be associated with the states of the surface valence band rather than with defect states and should not exceed 6.5 eV. It is a drawback of our model that the valence band states were completely absent and it was the defect state from which an electron has been removed; these defect states have been strongly stabilised by the potential of anion vacancy which explains why so large value is calculated for the IP. Regarding the experiments described above, we believe that one 5 eV photon could, in principle, cause emission of an electron from either defect states lying in the band gap or even from the top of the valence band if the latter is strongly perturbed by thermal vibrations. However, due to limitations of the present model, we cannot support this view. We are planning to improve our model so that the valence band would be properly represented and to consider adsorption-desorption processes at both charged and neutral surface vacancy defects.

III) Emission of the Mg^+ ion. After ionisation, the repulsive interaction between the ad-atom and the surface causes the ad-atom to escape. As the Mg^+ ion moves away from the surface, the total energy of the system decreases monotonically. The energy gain reaches 1.5 eV at the distance of 8.0 Å between the Mg^+ ion and the surface. At this distance the interaction of the surface and the Mg^+ ion can be considered as a Coulomb interaction of two point charges; the energy of this interaction is 3.6 eV. The overall energy gain in this model of the desorption process was found to be *ca.* 5.1 eV, which suggests that once the defect centre is ionised, the ad-ion acquires relatively large kinetic energy, comparable with those observed from the experimental data.

5.1.6 Discussion and summary

The kinetic energy of the desorbed ad-ion obtained from the experimental data (7.9 eV) is quite close to that obtained in our calculation (5.1 eV). The difference may arise from several factors. First, the "on top" position for the ad-atom is not optimal and was considered only as a model; second, the mechanism of desorption may include more than one step. For example, as suggested in [49], ionisation of the defect centre formed by the Mg ad-atom and anion vacancy may occur after the centre is excited by the 5 eV light with formation of a ${F_s}^+/Mg^+$ defect centre. Ionisation of the defect from its excited state might lead to higher kinetic energies of the desorbed ions. We should note here that irrespective of the initial state, before the excitation, of the defect - F_s/Mg^{2+}, as suggested in [49], or ${F_s}^{2+}/Mg$, according to our calculations, - excitation accompanied by charge transfer would create the ${F_s}^+/Mg^+$ defect centre.

To summarise, we have undertaken preliminary modelling of induced desorption of an Mg^+ ion from the (001) MgO surface containing anion vacancy aiming to check, from detailed calculations, the assumptions made in the previous studies. Our modelling suggests that the adsorption of Mg atom on top of the anion vacancy is not accompanied by charge transfer of the type $Mg + F_s^{2+} \Longrightarrow Mg^{2+} + F_s$ as assumed previously. Once the $Mg/{F_s}^{2+}$ centre is ionised, the Mg^+ ion desorbs with a kinetic energy close to 5 eV leaving an $F_s{}^{2+}$ centre behind. This energy is close to the experimentally obtained kinetic energies of desorbed Mg^+ ions from the polished (001) MgO surface (7.9 eV).

To clarify the model for the desorption of the Mg^+ ions we still have to answer the following questions. First, what is the value of the ionisation potential of the defect centre if the surface valence band is properly represented? Second, how will it change if the excessive charge of the anion vacancy is compensated by the neighbouring cation vacancy? Third, what are the charge density distributions of the initial and ionised states of the system in this case? Fourth, how do they affect the kinetic energy of the desorbed ions species? Finally, what is the charge state of the desorbed species and what is the model for the desorption of the Mg^{2+} ions? Studies aiming to answer these questions are currently being pursued.

5.2 Interaction of a silicon tip with the (001) NaCl surface: possibility of tip contamination

Scanning force microscopy (SFM) is routinely used in many branches of science and technology. The range of applications includes phenomena from the micrometer down to the sub-nanometre scale: surface topography, control of film growth, measurements of adhesion, friction, studies of lubrication, dielectric and magnetic properties, and contact charging. In particular, both ion and electron transfer due to contact formation and breaking is responsible for contact electrification and tribocharging; using these processes one could construct nano-structures from vacancies in different charge states or extract unwanted surface impurities by a tip.

Recent advances in scanning force microscopy based on dynamic-force methods, such as the non-contact mode of SFM operation [83], make it possible to achieve "true" atomic resolution on insulators [11], [12]. In this technique (see Fig. 27), the cantilever oscillates above the surface with large (of the order of 50 Å) amplitude with a minimum tip-surface distance of a fraction of nanometre. Information regarding the surface is generated from analysis of the frequency and amplitude changes due to the tip-surface interaction [83], [84], [125]. These developments are vital for a wide range of SFM applications including studies of point surface defects, and construction and modification of nano-structures at surfaces. However, existing uncertainty of the atomistic structure of the tip hampers both our understanding of SFM images and the possibility of controlled surface modification. The problem is complicated by the fact that even in the non-contact mode of SFM operation, where the tip is supposedly not touching the surface, the tip and surface modifications are impossible to avoid completely [12], [60]. These may be caused by avalanche adhesion which takes place for many metallic and ionic tips and surfaces at tip-surface distance less than 4-5 Å [157], [195], [128], [191], [188] or by intrinsic modification of the tip due to rearrangement of tip atoms (Fig. 28(a)). Dependence of an SFM image on the tip structure is demonstrated in Fig. 28(b) for the example of the NaCl (001) surface. The image pattern changes after a few scan lines as a result of such modification. Reverse

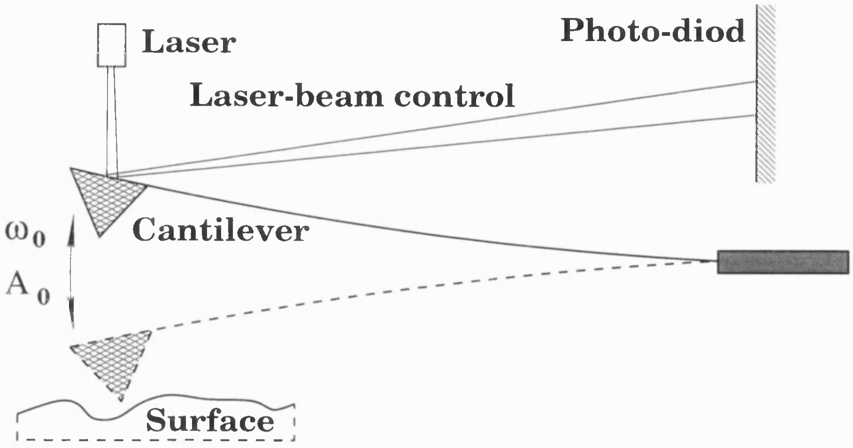

Figure 27: Non-contact SFM operation mode (schematic representation). Changes of the frequency (ω) and amplitude (A) contain information regarding the tip-surface interaction.

modification occurs after a few more scan lines and restores the original image pattern.

Details of numerous experimental and theoretical studies of the non-contact SFM operation mode can be found, for example, in recent review [190]. In the present work we focus on some of the issues related to the silicon tip structure in a typical SFM experiment: tip modification due to contact formation and breaking of ionic surfaces and possibility of charge transfer between the tip and the surface. The questions we would like to address in this section are i) what is the mechanism of contamination of the tip by the surface material? and ii) what are the charge states of the ions extracted by the tip from the ionic surfaces? We shall emphasise that it is essential to apply quantum-mechanical methods in order to reveal nature of charge transfer originating from the tip-surface interaction. These question have been raised and partly resolved in our previous work [203].

5.2.1 Embedded cluster modelling

The model of the surface and the method of calculations are the same as previously described (Chapter 2), and are discussed only briefly. The model of the tip is discussed separately as it is an essential component of these studies.

Details of calculations. We employ a finite nano-cluster model to study possible modifications of a silicon tip due to its interaction with the NaCl (001) surface. The total size of the nano-cluster and the size of the shell model region were 8×8×4 and 6×6×3 ionic centres respectively. The quantum mechanically treated part included the silicon tip modelled by a cluster of 29 atoms (Si_{29}) and a fragment of the surface modelled by one surface anion surrounded by five cations (Na_5Cl_1). The QM cluster was treated at the HF level using double zeta (lanl2dz) basis set and an Effective Core Pseudo-potential [216] replacing core electrons. When the adiabatic potential for the displacement of the

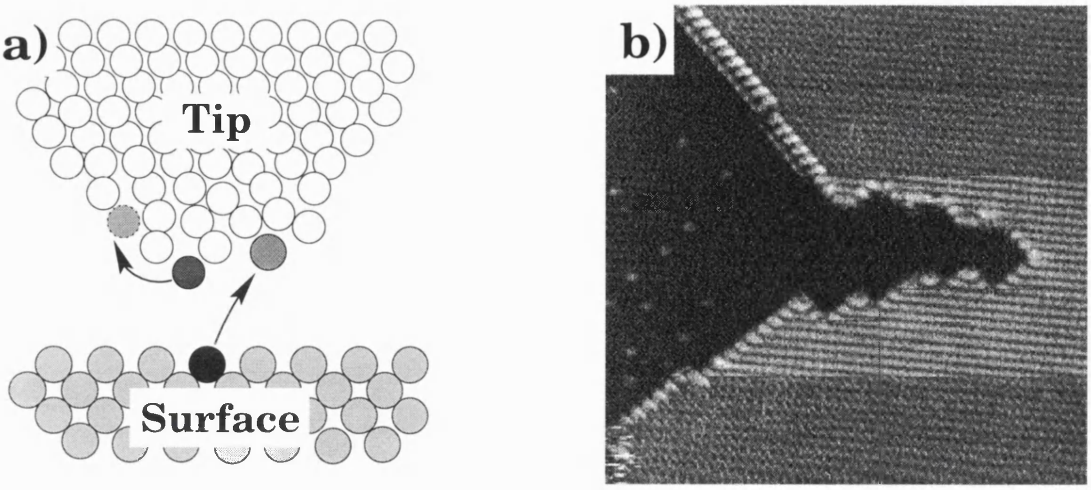

Figure 28: Tip modification during the scanning process.
a) Possible mechanisms of the tip modification;
b) SFM image of the NaCl (001) surface becomes brighter after the tip modification. Presumably reverse modification restores the original pattern. (Courtesy of Dr. R.Bennewitz and members of his group.)

chlorine ion from the surface to the tip was calculated, the Cl basis set was added to the vacancy to retain the quality of the surface description. The geometry of the Si_{29} cluster was optimised separately in a free cluster approximation and then fixed in all calculations; only the surface atoms were allowed to relax.

Model of the tip. Most of the commercial cantilevers are micro-fabricated from silicon and are covered by a native oxide layer. The surface is then cleaned by sputtering with Ar^+ ions. However, the chemical structure and geometry of the tip are almost impossible to control. The factors which dominate the tip structure in real life experiments could be summarised as follows: i) the silicon nano-tip should have the characteristic features of the most stable Si(111) (7×7) surface; ii) the tip may have some residual oxide layer or oxygen adsorbed on it; iii) it may be contaminated by hydrogen or water residual in the vacuum chamber; iv) it may also be contaminated by the surface material.

These factors are too complex to be investigated and discussed in full. We limited our model of the tip by a finite silicon cluster without any impurities. To choose the cluster, we followed earlier work (see [81], [105] and references therein) where the physical characteristics of the silicon clusters containing different number of atoms have been investigated. In particular, it was found that clusters containing 33 and 29 atoms are among the most stable silicon nano-structures. For our modelling the cluster containing 29 atoms (Fig. 29(a)) was used. It is expected that those cluster atoms with the lowest coordination number will be the most chemically active and are the most likely to be the probe species. For this reason the cluster was oriented by the most outstanding atoms towards the surface. As mentioned above, in all tip-surface interactions, the calculated geometry

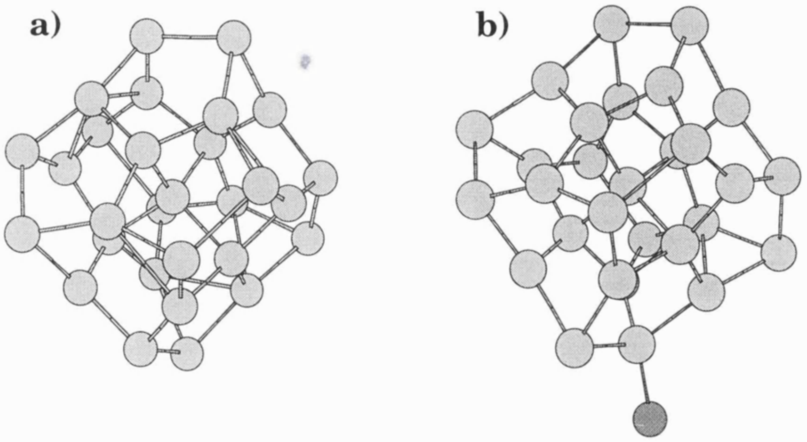

Figure 29: Silicon cluster used to model SFM tip: (a) free Si_{29}; (b) Si_{29} with adsorbed Cl^- on it.

of the cluster was fixed and only its electronic structure was relaxed. The charge density of the Si_{29} cluster tends to be polarised towards its bulk-like centre. This observation is in agreement with that of [105].

5.2.2 Results and discussion

Adiabatic potentials. We brought the quantum mechanically treated Si_{29} cluster to different distances above the chlorine ion on the NaCl (001) surface and calculated the adiabatic potential for the displacements of the ion towards the tip perpendicular to the surface. The calculated adiabatic potentials are shown in Fig. 30. When the surface-tip distance (D) is between 3.0 - 4.0 Å, the adiabatic potential exhibits only one minimum, which corresponds to the chlorine ion being between the tip and the surface at about 0.5-1.5 Å above the original surface site. As the tip-surface distance increases, the single well adiabatic potential transforms into the double well one (see Fig. 30) demonstrating an instability effect similar to that observed in [188]. The two wells of the double well potential correspond to the chlorine species being trapped at the surfaces (which appears for D larger than 4.5 Å) and at the tip (which becomes distinctively visible for D larger than 6.0 Å) respectively.

It is important to note that in these calculations the "surface end" of the calculated adiabatic potentials is represented better than the "tip end". This unbalance stems from two technical limitations: i) the surface was relaxed for every position of the tip and the surface chlorine ion, while tip geometry was fixed; ii) the adiabatic potential was calculated along one of the surface symmetry axes which guarantees the lowest total energy at the "surface end" but not necessarily so at the "tip end". Nevertheless, the transformation

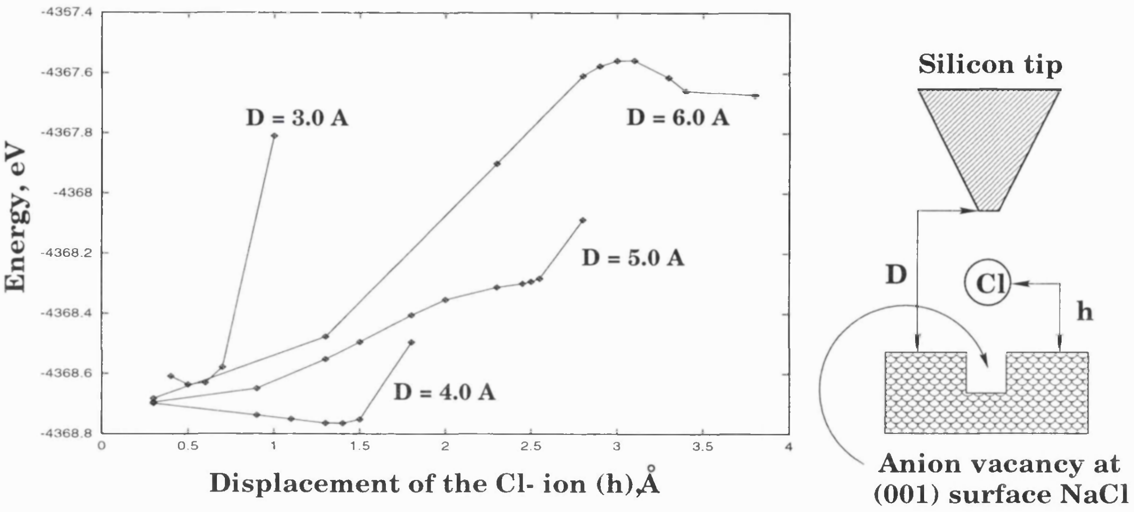

Figure 30: Adiabatic potential for Cl ion for different surface-tip distances.

of the single-well into the double-well adiabatic potential with the increase of the surface-tip distance is established. The potential well at the "tip end" is expected to be more pronounced if the tip was treated more accurately. The chlorine atom can be trapped by the tip if the potential well on the tip is formed at the tip-surface distance of about 4-5 Å. We stress that the chlorine atom can be trapped by the tip even if the potential well at the surface is deeper than the potential well at the tip provided that the barrier between the two is large enough. Details of the tip contamination mechanisms are discussed in reference [188].

Charge state of the chloride species. We can employ the advantages of the *ab initio* over the classical approach to investigate the issue of the charge state of the chloride species if adsorbed by the tip. The charge states of the extracted ion and the surface vacancy have been analysed by means of the Natural Population Analysis. The dependence of the NPA chlorine charge on the distance from the surface for several tip-surface distances (D) is shown in Fig. 31. As the chlorine species approaches the tip at a distance of 2.5 Å or less it loses from 30 to 50% of its ionic charge which transfers to silicon cluster and delocalises over the peripheral atoms. If the chlorine ion is trapped by the tip and removed to an infinite distance from the surface it loses 60% of its formal ionic charge. For tip-chlorine distances larger than 4.0 Å the tip potential well is not strong enough at the chlorine site and the Cl atom keeps the additional electron. It is important to note that the electron affinity of the Cl atom is seriously underestimated in these calculations. Its calculated value of 1.9 eV is only half of the experimental value of 3.62 eV.

The NPA charge of the ghost centre associated with surface vacancy was negligible in all our calculations which means that if the surface anion is adsorbed by the tip, it leaves the surface in its ionic rather than atomic charged state. This correlates with our previous observations that surface vacancies have relatively small electron affinities (Chapter 4).

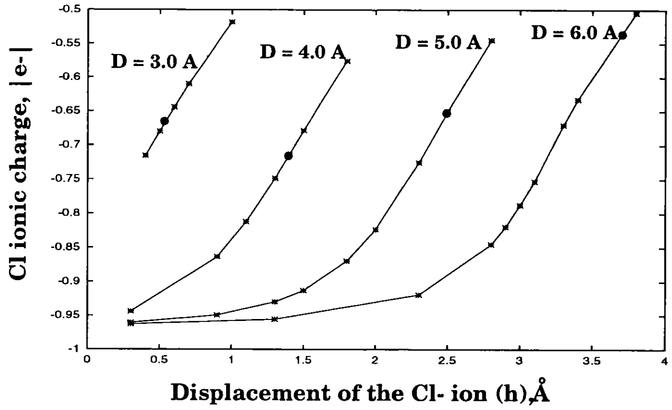

Figure 31: Dependence of the chlorine charge (NPA) on the distance from the surface for several tip-surface distances.
Bold dots indicate approximate position of the well associated with the tip.

Table 25: Possible processes for the tip contamination and corresponding affinities.

Initial state	Final state	Energy gain, eV
Si_{29}	Si_{29} + e^-	3.63
Si_{29} + e^-	Si_{29} + e^- + Cl	2.40
Si_{29}	Si_{29} + Cl	4.50
Si_{29} + Cl	Si_{29} + Cl + e^-	1.52
Si_{29}	Si_{29} + Cl + e^-	4.14

For, example, the singly charged surface oxygen vacancy (F_s^+ centre) on a (001) MgO surface has an electron affinity calculated at the HF level of only 1.7 eV. In the case of the (001) NaCl surface this value is expected to be even smaller.

Reactivity of the silicon tip. The possibility of contamination is higher for a more reactive tip. One can characterise the reactivity of the tip in terms of its affinity for electrons or atomic/ionic species. We have examined the affinity of the free Si_{29} cluster for an electron, atomic chlorine and negative chlorine ion. An electron transfer from the surface to the tip and contamination of the tip with atoms or ions can occur on very different time scales (depending on a number of inter-related factors). It is, therefore, convenient to distinguish the following different processes for tip contamination (see Table 25): i) electron transfer followed by atomic Cl adsorption, ii) adsorption of atomic Cl followed by an electron transfer, and iii) adsorption of a negative chlorine ion. Due to its structure, the Si_{29} cluster may have several sites with positive affinity for Cl or Cl^- species. We have studied only one of these sites located near the Si atom closest to the surface (see Fig. 29(b)).

In all of these processes the final state always has a lower energy than the initial one, which indicates that the free tip is reactive enough to provide a potential well for the adsorbed species. The depth of the potential well and its location can be affected by the presence of the surface.

5.2.3 Summary

Under-coordinated atoms of the silicon cluster demonstrate relatively high affinities for ionic and atomic species, which opens up the possibility of trapping some of the surface species by the tip to "saturate" its dangling bonds. The calculated adiabatic potentials for adsorption of a surface anion at the tip, support such a possibility. Chlorine species, if trapped by the tip, leave the surface with the ionic charge state Cl^-. In the resulting $(tip+Cl)^-$ system, about 40% of the negative charge is associated with chlorine, another 40% - with its nearest two Si neighbours and the other 20% are delocalised over the rest of the cluster. We can, therefore, speculate that initial stages of the surface scanning may be relatively destructive for the surface and be accompanied by the generation of charged anion vacancies.

A number of limitations of the present modelling, which have been mentioned above, are not expected to affect our conclusions qualitatively. Nevertheless, to clarify them quantitatively, one has to investigate how a better representation of the surface and geometry relaxation of all centres affects the results; what are the formation energies of the neutral surface F centre and the charged anion vacancy and how these change in the presence of the silicon tip. Severe underestimation of the electron affinity for the Cl atom is inherent for the HF method and is expected to take place for the tip as well. However, it is difficult to make any statement regarding to the accuracy of the calculated EA of the tip. Our experience gained with hybrid density functional methods, such as B3LYP, suggests that this method, though more time consuming, is more reliable in modelling such complex systems.

Summary and Conclusions

The results of the present Thesis can be divided into two major parts. In the first part, we summarise the results concerning the method, and the computer implementation of the embedded cluster approach. In the second part, we outline the results obtained using the method and the code developed in the present Thesis.

Embedded cluster approach: method and computer implementation

Method. The effective scheme for calculation of point defect properties in the bulk and at surfaces of ionic materials was developed and implemented in the computer code. The code is able to undertake calculation of the following defect properties: i) *local atomic structures* of defects; ii) optical properties of defects including *excitation* and *luminescence* energies, *ionisation potentials* and *electron affinities*; iii) local *vibrational properties* of defects.

Accuracy. The accuracy of calculations depends on a number of factors, which originate from the assumptions inherited in the embedded cluster approach and from quantum mechanical method used to study defect properties. We highlight these factors below:

- **crystal models**: point ion and shell model ion description of the crystal lattice is a central approximation used in the present method. It follows from the results presented in this Thesis and from previous experience that this model works well and produces consistent results for MgO, NaCl, $LiBaF_3$ crystals. It is expected that the model will be not less accurate for other ionic crystals.

- **defect space localisation**: the present method is developed for localised defects, i.e. defects, which are confined within the quantum mechanically treated cluster; accuracy of this approximation is controlled by the size of the quantum cluster.

- **defect state localisation**: the method works well if defect electronic sates are localised within the cluster; consequently, the accuracy of calculations for *a priory* delocalised states, e.g. band to band transitions, is uncontrolled.

- **methods**: accuracy of an embedded cluster calculation significantly depends on the accuracy and applicability of an *ab initio* method which is used to study the problem; the Gaussian98 package for quantum chemical calculations provides a range of methods which allows an investigator to undertake a comparative study using several *ab initio* techniques. We are currently working on implementation of this method with the GAMESS code.

Applicability. The applicability of the method to a particular system is defined by the accuracy required. The method works well and produces consistent results for highly ionic crystals such as alkali-halides, alkali earth oxides and perovskites (subject to limitations discussed in the previous paragraph). It may also be applied to ionic systems with molecular anion, such as Mg_2SiO_4. Application of the method to systems which cannot be divided into ionic fragments, for example SiO_2, will lead to less accurate results. However, even in this case the accuracy may be controlled by the size, shape, and composition of the quantum-mechanically treated region. The embedded cluster studies of SiO_2 polymorphs are currently in progress.

Further developments. The method was developed for highly ionic crystals. However, its extension to polar crystals can be achieved on the basis of the present code with some modifications, which would allow us to treat directed bonds. To achieve this we employ two approaches: i) the separable potential technique, outlined in section 1.2.5, and ii) development of the Group Function formalism reported in reference [111].

Results

The method and the computer code were applied to three types of problems. The first, the calculation of properties of point defects in the bulk of ionic crystals, is a traditional problem of solid state modelling. Most of the experimental techniques are developed for investigating this kind of defects, which allowed us to compare the results of our calculations with the experimental observations. The second type of problems is concerned with surface defect properties. Experimental observations of surface defect sites are hampered by their low concentrations. Therefore, only few defect characteristics can be measured directly and used as reference points for theoretical calculations. The third type of problems addressed in this Thesis concerns the mechanisms of processes at interfaces and photo-induced desorption. This area is even more difficult for direct experimental studies not only because of relatively small concentration of defect sites involved in these processes but also because some of these processes occur on a very short time scale. These three types of problems cover a wide range of systems and processes, which can be studied using the methodology and computer code developed in this Thesis.

- **Properties of point defects in the bulk of ionic crystals.** Two complex defects were considered: i) the $[Fe(CN)_6]^{3-,4-}$ defects incorporated into NaCl crystal matrix, and ii) the Ce^{3+} impurity defect in $LiBaF_3$. Several atomic configurations of iron cyanides were studied and the most stable configurations were identified. The influence of the local environment on the electronic structure of the iron ion and on vibrational properties of cyanide ligands were discussed. The electron affinities for several complexes were calculated. The dependence of the local atomic structure and of the excitation and luminescence energies of the $LiBaF_3$:Ce^{3+} centre on the model of host lattice environment was studied. It was demonstrated that the accurate account for the lattice polarisation is crucial for quantitative agreement of the optical absorption and luminescence energies with the experimentally observed properties of the Ce^{3+} centres in $LiBaF_3$.

- **Properties of point defects at surfaces of ionic crystals.** The electronic and spectroscopic properties of perfect and defective low-coordinated sites of MgO surface were studied. The ionisation potential of the ideal MgO (001) surface, which fixes position of the top of the surface valence band with respect to the vacuum level was calculated. The position of the bottom of the conduction band was estimated using i) the calculated electron affinity of the ideal surface, and ii) the calculated value of the surface optical absorption energy. The agreement between these two estimates shows consistency of models and methods used in these calculations. The electronic structure of the oxygen corner and oxygen vacancies (neutral F centre, charged F^+ centre and anion vacancy V_a) at the surface and at the oxygen corner have been investigated. The positions of the energy levels of these defect states with respect to the vacuum level, and therefore with respect to the surface valence band, were calculated. The dependence of the optical absorption of oxygen ions on their coordination number was studied. We also discussed localisation of the electron hole and additional electron at the MgO (001) surface and at oxygen corner sites and localisation of excitons at differently coordinated oxygen sites.
- **Modelling of processes at surfaces.** Theoretical modelling of surface processes is relevant to currently developing experimental techniques of non-contact atomic force microscopy and laser-induced desorption of the surface ions. i) The interaction of the Si tip with NaCl surface and a possibility of the tip contamination by the surface material have been investigated. It was demonstrated that the Si tip is likely to adsorb surface Cl^- ion. ii) To check the validity of assumptions underlying one of the models used for interpretation of the laser-induced ion desorption experiments we have calculated the local atomic structure of the Mg atom adsorbed in the vicinity of the surface anion vacancy V_a, the possibility of the system to be ionised by a 5.0 eV photon, the energy gain due to consequent desorption of the Mg^{2+} ion from the surface. It was demonstrated that the system electronic configuration is Mg/V_a rather than the previously thought Mg^{2+}/F. It is suggested that the local atomic structure of this system is different from the simplistic model used in the previous studies.

The calculation of a larger number of physical properties would greatly assist in direct comparison of the theoretical results and experiment. The recent release of the Gaussian98 package includes features for the calculation of hyperfine anisotropic constants, which gives us an opportunity to improve our results.

References

[1] I. V. Abarenkov and I. I. Tupitsyn. unpublished.

[2] I.V. Abarenkov. In Tennyson. R. C. and A. E. Kiv, editors, *Computer Modelling of Electronic and Atomic Processes in Solids*, volume 22 of *NATO ASI Series, High Technology*, pages 159–172. Kluwer Academic Publishers, 1996.

[3] W. H. Adams. *J. Math. Chem.*, 10:1–23, (1992).

[4] P.A. Anderson and P.P. Edwards. *J. Am. Chem. Soc.*, 114(26):10608–10618, (1992).

[5] K. Andersson, M. R. A. Blomberg, M. P. Fülscher, G. Karlström, R. Lindh, P.-Å. Malmqvist, P. Neogrády, J. Olsen, B. O. Roos, A. J. Sadlej, M. Schütz, L. Seijo, L. Serrano-Andrés, P. E. M. Siegbahn, and P.-O. Widmark. *MOLCAS Version 4*. Lund University, Sweden, 1997.

[6] J. Andriessen, H. Merenga, C. M. Combes, P. Dorenbos, and C. W. E. van Eijk. In P. Dorenbos and C. W. E. van Eijk, editors, *Proceedings of the International Conference on Inorganic Scintillators and their Applications SCINT95*, page 142, Delft, 1996. Delft University, Delft University Press.

[7] N. C. Bacalis and A. B. Kunz. *Phys. Rev. B*, 32(8):4857–4865, (1985).

[8] R. C. Baetzold. *J. Phys. Chem. B*, 101(7):1130–1137, (1997).

[9] P. S. Bagus, F. Illas, and C. Sousa. *J. Chem. Phys.*, 100(4):2943–2946, (1994).

[10] D. Bakovies and W. Thiel. *J. Comput. Chem.*, 17(1):87–108, (1996).

[11] M. Bammerlin, R. Lüthi, E. Meyer, A. Baratoff, J. Lu, M. Guggisberg, C. Gerber, and H.-J. Howald, L. Güntherodt. *Probe Microsc.*, 1:3, (1997).

[12] M. Bammerlin, R. Lüthi, E. Meyer, A. Baratoff, J. Lu, M. Guggisberg, C. Loppacher, C. Gerber, and H. J. Güntherodt. *Appl. Phys. A*, 66(Pt1):S293–S294, (1998).

[13] Z. Barandiaran and L. Seijo. *J. Chem. Phys.*, 89(9):5739–5746, (1988).

[14] Z. Barandiaran and L. Seijo. In S. Fraga, editor, *Computational Chemistry: Structure, Interactions and Reactivity*, volume 77B of *Studies in Physical and Theoretical Chemistry*, pages 435–461. Elsevier, Amsterdam, 1992.

[15] A. D. Becke. *J. Chem. Phys.*, 97(12):9173–9177, (1992).

[16] A. D. Becke. *J. Chem. Phys.*, 98(2):1372–1377, (1993).

[17] M. T. Bennebroek, O. G. Poluektov, A. J. Zakrzewski, P. G. Baranov, and J. Schmidt. *Phys. Rev. Lett.*, 74(3):442–445, (1995).

[18] M. T. Bennebroek, J. Schmidt, R. S. Eachus, and M. T. Olm. *J. Phys.: Condens. Matter*, 9:3227–3240, (1997).

[19] B. H. Besler, K. M. Merz Jr., and P. A. Kollman. *J. Comput. Chem.*, 11(4):431–439, (1990).

[20] S. F. Boys and F. Bernardi. *Mol. Phys.*, 19:553, (1970).

[21] T. S. Breneman and J. D. Wiberg. *J. Comput. Chem.*, 11(3):361–373, (1990).

[22] J. Q. Broughton and P. S. Bagus. *Phys. Rev. B*, 36(5):2813–2830, (1987).

[23] T. S. Bush, J. D. Gale, C. R. A. Catlow, and P. D. Battle. *J. Mater. Chem.*, 4(6):831–837, (1994).

[24] C. R. A. Catlow, J. Corish, K. M. Diller, P. W. M. Jacobs, and M. J. Norgett. *Journal de Physique*, 37(12):C7–253–C7–259, (1976).

[25] C. R. A. Catlow, J. Corish, J. M. Quigley, and P. W. M. Jacobs. *J. Phys. Chem Solids*, 41:231–241, (1980).

[26] C. R. A. Catlow, K. M. Diller, and M. J. Norgett. *J. Phys. C: Solid State Phys.*, 10:1395, (1977).

[27] C. R. A. Catlow and W. C Macrodt. *Computer Simulation of Solids*, volume 166 of *Lecture notes in physics*. Springer, Berlin, 1982.

[28] M. Causà and F. Ricca. *Surf. Sci.*, 298(1):251–258, (1993).

[29] Y. Chen, J. L. Kolopus, and W. A. Sibley. *Phys. Rev.*, 186(3):865–870, (1969).

[30] M. Chiesa, M. C. Paganini, E. Giamello, and D. M. Murphy. *Langmuir*, 13(20):5306–5315, (1997).

[31] L. E. Chirlian and M. M. Francl. *J. Comp. Chem.*, 8(6):894–905, (1987).

[32] L. J. Clarke, I. Stich, and M. C. Payne. *Comp. Phys. Comm.*, 72:14–28, 1992.

[33] S. Coluccia, A. Barton, and A. J. Tench. *J. Chem. Soc. Faraday Trans. I*, 77(Pt9):2203–2207, (1981).

[34] S. Coluccia, A. M. Deane, and A. Tench. *J. Chem. Soc. Faraday Trans. I*, 74:2913, (1978).

[35] S. Coluccia and L. Marchese. *Active Sites and Reaction Mechanisms on the Surface of Basic Catalysts: Spectroscopic Studies.* Sapporo, Kodansha, Tokyo, Japan, 1988.

[36] S. Coluccia, A. J. Tench, and R. L. Segall. *J. Chem. Soc. Faraday Trans. I*, 75:1769, (1979).

[37] C. M. Combes, P. Dorenbos, C. W. E. van Eijk, J. Y. Gesland, and P. A. Rodnyi. *J. Lum.*, 72-74:753–755, (1997).

[38] P. A. Cox and A. A. Williams. *Surf. Sci.*, 175:L782–L786, (1986).

[39] S. R. Cox and D. E. Williams. *J. Comput. Chem.*, 2(3):304–323, (1981).

[40] T. R. Cundari and W. J. Stevens. *J. Chem Phys.*, 98(7):5555–5565, (1993).

[41] J. Datka, P. Geerlings, W. Mortier, and P. Jacobs. *J. Phys. Chem.*, 89(16):3483–3488, (1985).

[42] J. Datka, P. Geerlings, W. Mortier, and P. Jacobs. *J. Phys. Chem.*, 89(16):3488–3493, (1985).

[43] P. K. de Boer and R. A. de Groot. *J. Phys.: Condens. Matter*, 10(45):10241–10248, (1998).

[44] J. E. Dennis and R. B. Schnabel. *Numerical Methods for Unconstrained Optimisation and Nonlinear Equations.* Prentice-Hall, Englewood Cliffs, NJ, 1983.

[45] A. D'Ercole, E. Giamello, C. Pisani, and L. Ojamäe. *J. Phys. Chem. B*, 103:3872–3876, (1989).

[46] J. P. Desclaux. *Comp. Phys. Commun.*, 9:31, (1975).

[47] B. G. Dick and A. W. Overhauser. *Phys. Rev.*, 112:90, (1958).

[48] J. T. Dickinson, D. R. Ermer, and J. J. Shin. *Appl. Surf. Sci.*, 129:7–20, (1998).

[49] J. T. Dickinson, S. C. Langford, and J. J. Shin. *Phys. Rev. Lett.*, 73(19):2630–2633, (1994).

[50] V. Dierolf. *Phys. Rev. B*, 60(18):12601–12609, (1999).

[51] V. Dierolf, E. Gustin, D. Shoemaker, and F. Luty. *J. Lumin.*, 76(7):526–529, (1998).

[52] V. Dierolf, J. Hoidis, D. Samiec, and W. von der Osten. *J. Lumin.*, 76(7):581–585, (1998).

[53] V. Donnerberg, E. Többen, and D. Birkholz. *J. Phys.: Condens Matter*, 9:6359–6370, (1997).

[54] R. Dovesi, V. R. Saunders, C. Roetti, M. Causà, N. M. Harrison, R. Orlando, and E. Apra. *CRYSTAL95 User's Manual.* University of Torino, Torino, 1996.

[55] R. Dovesi, V. R. Saunders, C. Roetti, M. Causà, N. M. Harrison, R. Orlando, and C. M. Zicovich-Wilson. *CRYSTAL98 User's Manual.* University of Torino, Torino, 1998.

[56] J. B. Duncan and H. J. Percival. *Aust. J. Chem.*, 21:2175–2188, (1968).

[57] R. S. Eachus, R. C. Baetzold, Th. D. Pawlik, O. G. Poluektov, and J. Schmidt. *Phys. Reb. B*, 59(13):8560–8571, (1999).

[58] P. P. Edwards, P. A. Anderson, and J. M. Thomas. *Acc. Chem. Res.*, 29(1):23–29, (1996).

[59] U. Eichler, C. M. Kölmel, and J. Sauer. *J. Comput. Chem.*, 18(4):463–477, (1996).

[60] R. Erlandsson, L. Olsson, and P. Martensson. *Phys. Rev. B*, 54(12):R8309–R8312, (1996).

[61] D. R. Ermer, J.-J. Shin, S. C. Langford, K. W. Hipps, and J. T. Dickinson. *J. Appl. Phys.*, 80(11):6452–6466, (1996).

[62] R. A. Evarestov, P. W. Jacobs, and A. V. Leko. *Phys. Rev. B*, 54(13):8969–8972, (1996).

[63] H. M. Evjen. *Phys. Rev.*, 39:675–687, (1932).

[64] P. P. Ewald. *Ann. Physik*, 64(4):253, (1921).

[65] A. M. Ferrari and G. Pacchioni. *J. Phys. Chem.*, 99(46):17010–17018, (1995).

[66] A. M. Ferrari and G. Pacchioni. *Int. J. Quantum Chem.*, 58(3):241–250, (1996).

[67] A. M. Ferrari and G. Pacchioni. *J. Phys. Chem.*, 107(6):2066–2078, (1997).

[68] F. Finocchi, J. Goniakowski, and C. Noguera. *Phys. Rev. B*, 59(7):5178–5188, (1999).

[69] A.J. Fisher. *Reviews of Solid state Science*, 5(2-3):107–132, (1991).

[70] F. Floris and J. Tomasi. *J. Comp. Chem.*, 10(5):616–627, (1989).

[71] J. B. Foresman and A. Frisch. *Exploring Chemistry with electronic structure Methods.* Gaussian, Inc., Pittsburg, PA, 1996.

[72] J. B. Foresman, M. Head-Gordon, J. A. Pople, and M. Frisch. *J. Phys. Chem.*, 96(1):135–149, (1992).

[73] L. S. Forster. *Chemical Reviews*, 90(2):331–353, (1990).

[74] L. S. Forster. *Adv. in Photochem.*, 16:215–248, (1991).

[75] P. W. Fowler and P. Tole. *Surf. Sci.*, 197(3):457–473, (1988).

[76] P. W. Fowler and P. Tole. *Reviews of Solid State Science*, 5(2-3):149–176, (1991).

[77] M. J. Frisch, G. W. Trucks, H. B. Schlegel, G. E. Scuseria, M. A. Robb, J. R. Cheeseman, V. G. Zakrzewski, J. A. Montgomery, R. E. Stratmann, J. C. Burant, S. Dapprich, J. M. Millam, A. D. Daniels, K. N. Kudin, M. C. Strain, O. Farkas, J. Tomasi, V. Barone, M. Cossi, R. Cammi, B. Mennucci, C. Pomelli, C. Adamo, S. Clifford, J. Ochterski, G. A. Petersson, P. Y. Ayala, Q. Cui, K. Morokuma, D. K. Malick, A. D. Rabuck, K. Raghavachari, J. B. Foresman, J. Cioslowski, J. V. Ortiz, B. B. Stefanov, G. Lui, A. Liashenko, P. Piskorz, I. Komaromi, R. Gomperts, R. L. Martin, D. J. Fox, T. Keith, M. A. Al-Laham, C. Y. Peng, A. Nanayakkara, C. Gonzalez, M. Challacombe, P. M. W. Gill, B. G. Johnson, W. Chen, M. W. Wong, J. L. Andres, M. Head-Gordon, E. S. Replonge, and J. A. Pople. *GAUSSIAN 98 (Release A1).* Pittsburgh PA, 1998.

[78] M.J. Frisch, G.W. Trucks, H.B. Schlegel, P.M.W. Gill, B.G. Johnson, M.A. Robb, J.R. Cheeseman, T.A. Keith, G.A. Petersson, J.A. Montgomery, K. Raghavachari, M.A. Al-Laham, V.G. Zakrzewski, J.V. Ortiz, J.B. Foresman, J. Cioslowski, B.B. Stefanov, A. Nanayakkara, M. Challacombe, C.Y. Peng, P.Y. Ayala, W. Chen, M.W. Wong, J.L. Andres, E.S. Replonge, R. Gomperts, R.L. Martin, D.J. Fox, J.S Binkley, D.J. Defrees, J. Baker, J.P. Stewart, M. Head-Gordon, C. Gonzalez, and J.A. Pople. *GAUSSIAN 94 (Revision E.1).* Pittsburgh PA, 1995.

[79] J. D. Gale. *J. Chem. Soc., Faraday Trans.*, 93:629–637, (1997).

[80] E. Garrone, A. Zecchina, and F. S. Stone. *Philos. Mag. B*, 42:683, (1980).

[81] Matthai C.C. Gavartin J.L and Morrison I. *Thin Solid Films*, 255:39–42, (1995).

[82] A. R. Gerson and T. Bredow. *Phys. Chem. Chem. Phys.*, 1:4889–4896, (1999).

[83] F. J. Giessibl. *Science*, 267(5194):68–71, (1995).

[84] F. J. Giessibl. *Phys. Rev. B*, 56(24):16010–16015, (1997).

[85] L. Gomes and F. Luty. *Phys. Rev. B*, 52(10):7094–7101, (1995).

[86] S. P. Greatbanks, P. Sherwood, and I. H. Hillier. *J. Phys. Chem.*, 98(33):8134–8139, (1994).

[87] R. W. Grimes, C. R. A. Catlow, and A. M. Stoneham. *J. Phys.: Condens. Matter*, 1:7367–7384, (1989).

[88] O. Gropen, U. Walgren, and L. Petterson. *Chem. Phys.*, 66(3):459–464, (1982).

[89] M. F. Guest, J. H. van Lenthe, J. Kendrick, K. Schoeffel, P. Sherwood, and Harrison R. J. Computing for Science (CFS) Ltd., Daresbury Laboratory., Warrington, UK, 1994.

[90] J. H. Harding, A. H. Harher, P. B. Keegstra, R. Pandey, J. M. Vail, and C. Woodward. *Physica*, 131B:151–156, (1985).

[91] A. H. Harker. In R. C. Tennyson and A. E. Kiv, editors, *Computer Modelling of Electronic and Atomic Processes in Solids*, pages 181–192. Kluwer Academic Publishers, 1997.

[92] P. J. Hay and W. R. Wadt. *J. Chem. Phys.*, 82(1):299–310, (1985).

[93] V. E. Henrich, G. Dresselhaus, and H. J. Zeider. *Phys. Rev. B*, 22(10):4764–4775, (1980).

[94] K. Hermann. In G. Pacchioni, P. S. Bagus, and F. Parmigiani, editors, *Cluster Models for Surface and Bulk Phemomena.*, volume 283 of *NATO ASI Series*, page 209. Plenum Press, New York, 1992.

[95] K. Hermann and P. S. Bagus. *Phys. Rev. B*, 17(10):4082–4099, (1978).

[96] S. Huzinaga, Ed. J. Andzelm, M. Klobukowski, E. Radzio-Andzelm, Y. Sakai, and H. Tatewaki. *Gaussian Basis Sets for Molecular Calculations.* Elsevier, Amsterdam, 1984.

[97] S. Huzinaga and A. A. Chantu. *J. Chem. Phys.*, 55:5543, (1971).

[98] S. Huzinaga, S. Katsuki, and O. Matsuoka. *J. Math. Chem.*, 10:25–39, (1992).

[99] S. Huzinaga, D. McWilliams, and A. A. Chantu. *Adv. Quant. Chem.*, 7:187, (1973).

[100] F. Illas and G. Pacchioni. *J. Chem. Phys.*, 108(18):7835–7841, (1998).

[101] J. E. Inglesfield. *J. Phys. C: Solid State Phys.*, 14:3795–3806, (1981).

[102] R. A. Jackson, M. E. G. Valerio, and J. F. de Lima. *J. Phys.: Condens. Matter*, 8:10931–10937, (1996).

[103] S. C. Jain, A. V. R. Warrier, and H. K. Sehgal. *J. Phys. C: Solid State Phys.*, 5:1511–1518, (1972).

[104] S. C. Jain, A. V. R. Warrier, and H. K. Sehgal. *J. Phys. C: Solid State Phys.*, 6:193–200, (1973).

[105] Gavartin J.L. and Matthai C.C. *Materials Science and Engineering B*, B35:459–462, (1995).

[106] C. K. Jorgensen. *Absorption spectra and chemical bonding in complexes.* Pergamon Press, 1962.

[107] L. Kantorovich, A. Stashans, E. Kotomin, and P. W. M. Jacobs. *Int.J.Quant.Chem.*, 52:1177–1198, (1994).

[108] L. N. Kantorovich. *J. Phys. C: Solid State Phys.*, 21:5041–5056, 1988.

[109] L. N. Kantorovich. *J. Phys. C: Solid State Phys.*, 21:5057–5073, 1988.

[110] L. N. Kantorovich. *Phys. Rev. B*, 60(23):15476–15479, 1999.

[111] L. N. Kantorovich. *Int. J. Quant. Chem.*, 76:511–534, 2000.

[112] L. N. Kantorovich and M. J. Gillan. *Surf. Sci.*, 374:373–386, 1997.

[113] L. N. Kantorovich, J. M. Holender, and M. J. Gillan. *Surf. Sci.*, 343(3):221–239, 1995.

[114] L. N. Kantorovich, A. L. Shluger, P. V. Sushko, J. Günster, P. Stracke, D. W. Goodman, and V. Kempter. *Faraday Discuss.*, 114:173–194, 1999.

[115] L. N. Kantorovich, A. L. Shluger, P. V. Sushko, and A. M. Stoneham. *Surf. Sci.*, 444:31–51, (2000).

[116] L. N. Kantorovich and I. I. Tupitsyn. *J. Phys.: Condens. Matter*, 11:6159–6168, (1999).

[117] L. A. Kappers, R. L. Kroes, and E. B. Hensley. *Phys. Rev. B*, 1(10):4151–4157, 1970.

[118] S. Kapphan. *J. Phys. Chem. Solids*, 35:621–639, (1974).

[119] E. Kassab, K. Seiti, and M. Allavena. *J. Phys. Chem.*, 95(23):9425–9431, (1991).

[120] V. Kempter and M. Brause. volume 77 of *NATO Science*, pages 249–259. Kluwer Academic Publishers, Dordrecht/Boston/London, 2000.

[121] A. Klamt and G. Schüürmann. *J. Chem. Soc. Perkin Trans.*, 2:799–805, (1993).

[122] K. P. Koch, Y. Yang, and F. Luty. *Phys. Rev. B*, 29(10):5840–5848, (1984).

[123] G. Kresse and J. Furthmüller. *Comp. Mat. Sci.*, 6(6):15–50, 1996.

[124] G. Kresse and J. Furthmüller. *Phys. Rev. B*, 54(16):11169–11186, 1996.

[125] D. Kruger, B. Anczykowski, and H. Fuchs. *Ann. Phys.*, 6(5):341–363, (1997).

[126] A. B. Kunz and D. L. Klein. *Phys. Rev. B*, 17(12):4614–4619, (1978).

[127] A. B. Kunz and J. M. Vail. *Phys. Rev. B*, 38(2):1058–1063, (1988).

[128] U. Landman, W. D. Luedtke, N. A. Burnham, and R. J. Colton. *Science*, 248(4954):454–461, (1990).

[129] M. Leslie and M. J. Gillan. *J. Phys. C: Solid State Phys.*, 18(5):973–982, (1985).

[130] A. C. Lewandowski and T. M. Wilson. *J. Comput. Phys.*, 129:233–242, (1996).

[131] A. O. Litinskii. *J. Struct. Chem.*, 23(4):527–533, (1982).

[132] A. O. Litinskii and A. S. Zyubin. *J. Struct. Chem.*, 25(4):516–520, (1984).

[133] J. H. Lunsford and J. P. Jayne. *J. Chem. Phys.*, 44:1487, (1966).

[134] J. Magill, J. Bloem, and R. W. Ohse. *J. Chem. Phys.*, 76(12):6227–6242, (1982).

[135] G. Makov and M. C. Payne. *Phys. Rev. B*, 51(7):4014–4022, (1995).

[136] M. Marsman, J. Andriessen, and C. W. E. van Eijk. *J. Lumin.*, 87(9):1023–1025, (2000).

[137] R. McWeeny. *Proc. R. Soc. London Ser. A*, 253:242, (1959).

[138] R. McWeeny. *Methods of Molecular Quantum Mechanics.* Academic Press. Harcourt Brace Jovanovich, Publishers, 2 edition, 1992.

[139] E. L. Mehler. *J. Math. Chem.*, 10:57–91, (1992).

[140] J. A. Mejias, V. Staemmler, and H-J. Freund. *J. Phys.: Condens. Matter*, 11:7881–7891, (1999).

[141] C. E. Messer. *J. Sol. Stat. Chem.*, 2:144, (1970).

[142] N. F. Mott and M. J. Littleton. *Trans. Faraday Soc.*, 34:485–499, (1938).

[143] D. Murphy, R. D. Farley, I. J. Purnell, C. C. Rowlands, A. R. Yacob, M. C. Paganini, and E. Giamello. *J. Phys. Chem.*, 103:1944–1953, (1999).

[144] D. Murphy and E. Giamello. *J. Phys. Chem.*, 98(33):7929–7932, (1994).

[145] D. Murphy and E. Giamello. *J. Phys. Chem.*, 99(41):15172–15180, (1995).

[146] R. L. Nelson and J. W. Hale. *Discuss. Faraday Soc.*, 52:77, (1971).

[147] R. Orlando, R. Millini, G. Perego, and R. Dovesi. *J. Molec. Catal.*, 119(1-3):253–262, (1997).

[148] G. Pacchioni and G. Ieranò. *Phys. Rev. Lett.*, 79(4):753–756, (1997).

[149] G. Pacchioni and G. Ieranò. *Phys. Rev. B*, 56(12):7304–7312, (1997).

[150] G. Pacchioni and G. Ieranò. *Phys. Rev. B*, 57(2):818–832, (1998).

[151] M. C. Paganini, M. Chiesa, E. Giamello, S. Coluccia, G. Martra, D. M. Murphy, and G. Pacchioni. *Surf. Sci.*, 421:246–262, (1999).

[152] R. Pandey, J. Zuo, and A. B. Kunz. *Phys. Rev. B*, 39(17):12565–12567, (1989).

[153] R. G. Parr and W. Yang. *Density-functional theory of atoms and molecules.* New York: Oxford University Press; Oxford: Clarendon, 1989.

[154] J. L. Pascual and L. Seijo. *J. Chem. Phys.*, 102(13):5368–5376, (1995).

[155] L. Pauling. *J. Am. Chem. Soc.*, 53:1367, (1931).

[156] M. C. Payne. In E. M. Anastassakis and J. D. Joannopoulos, editors, *Proc. 20th Int. Conf. on Physics of Semiconductors*, volume 1-3, page 41, (1990).

[157] J. B. Pethica and A. P. Sutton. *J. Vac. Sci. Technol.*, A6(4):2490–2494, (1988).

[158] M. I. Petrashen, I. V. Abarenkov, A. A. Berezin, and R. A. Evarestov. *Phys. Stat. Sol.*, 40:9, (1970).

[159] M. I. Petrashen, I. V. Abarenkov, A. A. Berezin, and R. A. Evarestov. *Phys. Stat. Sol.*, 40:433–460, (1970).

[160] M. I. Petrashen, I. V. Abarenkov, A. A. Berezin, and R. A. Evarestov. volume I. Quantum Mechanics, pages 208–262. Leningrad University Press, Leningrad, 1973.

[161] L. G. M. Pettersson, M. Nyberg, J.-L. Pascual, and M. A. Nygren. In R. M. Lambert and G. Pacchioni, editors, *Chemisorption and Reactivity on Supported Clusters and Thin Films*, pages 425–454. Kluwer Academic Publishers, Amsterdam, 1997.

[162] C. Pisani, F. Corà, R. Nada, and R. Orlando. *Comp. Phys. Commun.*, 82:139–156, (1994).

[163] C. Pisani, R. Dovesi, R. Nada, and L. N. Kantorovich. *J. Chem. Phys.*, 92(12):7448–7460, (1990).

[164] C. Pisani, R. Dovesi, and C. Roetti. *Hartree-Fock Ab Initio Treatment of Cryslalline Systems*, volume 48 of *Lecture Notes in Chemistry.* Springer, Berlin, 1988.

[165] S. A. Pope, M. F. Guest, I. H. Hillier, E. A. Colbourn, W. C. Mackrodt, and J. Kendrick. *Phys. Rev. B*, 28(4):2191–2198, (1983).

[166] A. Redondo, W. A. Goddard, C. A. Swarts, and T. C. McGill. *J. Vac. Sci. Technol.*, 19(3):498–501, (1981).

[167] A. E. Reed, R. B. Weinstock, and F. Weinhold. *J. Chem. Phys.*, 83(2):735–746, (1985).

[168] P. Reinhardt, M. Causà, C. M. Marian, and B. A. Hess. *Phys. Rev. B*, 54(20):14812–14821, (1996).

[169] C. Ribbing, B. Gilliams, A. Ceulemans, K. Pierloot, D. Vandenbroucke, and B. Roos. *J. Chem. Phys.*, 110(14):6849–6857, (1999).

[170] O. Robach, G. Renaud, and A. Barbier. *Surf. Sci.*, 401:227–235, (1998).

[171] D. M. Roessler. *Phys. Rev.*, 159:733, (1959).

[172] G. H. Rosenblatt, M. W. Rowe, G. P. Williams Jr., R. T. Williams, and Y. Chen. *Phys. Rev. B*, 39(14):10309–10318, (1989).

[173] D. K. Rowell and M. J. L. Sangster. *J. Phys. C: Solid State Phys.*, 14(21):2909–2921, (1981).

[174] M. A. San Miguel, C. J. Calzado, and J. F. Sanz. *Int. J. Quantum Chem.*, 70:351–357, (1998).

[175] J. Sauer. *Chem. Rev.*, 89(1):199–255, (1989).

[176] J. Sauer, C. Morgeneyer, and K. P. Schroder. *J. Phys. Chem.*, 88(25):6375–6383, (1984).

[177] J. Sauer, P. Ugliengo, E. Garrone, and V. R. Saunders. *Chem. Rev.*, 94(7):2095–2160, (1994).

[178] M. A. Schildbach and A. V. Hamza. *Phys. Rev. B*, 45(11):6197–6206, (1992).

[179] M. W. Schmidt, K. K. Baldridge, J. A. Boatz, S. T. Elbert, M. S. Gordon, J. H. Jensen, S. Koseki, N. Matsunaga, K. A. Nguyen, S. J. Su, T. L. Windus, M. Dupuis, and J. A. Montgomery. *J. Comput. Chem.*, 14:1347–1363, (1993).

[180] P. A. Schultz. *Phys. Rev. B*, 60(3):1551–1554, (1999).

[181] P. D. Schulze and J. R. Hardy. *Phys. Rev. B*, 5(8):3270–3275, (1972).

[182] E. Scorza, U. Birkenheuer, and C. Pisani. *J. Chem. Phys.*, 107(22):9645–9658, (1997).

[183] L. Seijo and Z. Barandiarán. *J. Math. Chem.*, 10:41–56, (1992).

[184] R. Shepard. Ab Initio *Methods in Quantum Chemistry-II*, pages 63–200. Advances in Chemical Physics. John Wiley and Sons Ltd., 1987.

[185] A. L. Shluger and J. D. Gale. *Phys. Rev. B*, 54(2):962–969, (1996).

[186] A. L. Shluger, A. H. Harker, V. E. Puchin, N. Itoh, and C. R. A. Catlow. *Modelling Simul. Mater. Sci. Eng.*, 1(5):673–692, (1993).

[187] A. L. Shluger, N. Itoh, V. E. Puchin, and E. N. Heifets. *Phys. Rev. B*, 44(4):1499–1508, (1991).

[188] A. L. Shluger, L. N. Kantorovich, A. I. Livshits, and M. J. Gillan. *Phys. Rev. B*, 56(23):15332–15344, (1997).

[189] A. L. Shluger, E. A. Kotomin, and L. N. Kantorovich. *J. Phys. C: Solid State Phys.*, 19(22):4183–4199, (1986).

[190] A. L. Shluger, A. I. Livshits, A. S. Foster, and C. R. A. Catlow. *J. Phys.: Condens. Matter*, 11(26):R295–R322, (1999).

[191] A. L. Shluger, A. L. Rohl, D. H. Gay, and R. T. Williams. *J. Phys.: Condens. Matter*, 6(10):1825–1846, (1994).

[192] A. L. Shluger, P. V. Sushko, and L. N. Kantorovich. *Phys. Rev. B*, 59(3):2417–2430, 1999.

[193] A. L. Shluger and K. Tanimura. *Phys. Rev. B*, 61(8):5392–5402, (2000).

[194] U. C. Singh and P. A. Kollman. *J. Comput. Chem.*, 5(2):129–145, (1984).

[195] J. R. Smith, G. Bozzolo, A. Banerjea, and J. Ferrante. *Phys. Rev. Lett.*, 63(12):1269–1272, (1989).

[196] C. Sousa, G. Pacchioni, and F. Illas. *Surf. Sci.*, 429:217–228, (1999).

[197] E. V. Stefanovich and T. N. Truong. *J. Chem. Phys.*, 106(18):7700–7705, (1997).

[198] M. Sterrer, O. Diwald, and E. Knözinger. *J. Phys. Chem. B*, 104(15):3601–3607, (2000).

[199] W. J. Stevens, H. Basch, and M. Kraus. *J. Chem. Phys.*, 81(12):6026–6033, (1984).

[200] D. M. Sturmer. *Encyclopedia of Applied Physics*. VCH Publishrs, Inc., 1996.

[201] S. Sugano and R. G. Shluman. *Phys. Rev.*, 130:517, (1963).

[202] G. P. Summers, T. M. Wilson, B. T. Jeffries, H. T. Tohver, Y. Chen, and M. M. Abraham. *Phys. Rev. B*, 27(2):1283–1291, (1983).

[203] P. V. Sushko, A. S. Foster, L. N. Kantorovich, and A. L. Shluger. *Appl. Surf. Sci.*, 144-145:608–612, (1999).

[204] P. V. Sushko and A. L. Shluger. *Surf. Sci.*, 421:L157–L165, (1999).

[205] P. V. Sushko, A. L. Shluger, and C. R. A. Catlow. *Surf. Sci.*, 450:153–170, (2000).

[206] P.V. Sushko, A. L. Shluger, C. R. A. Catlow, and R. C. Baetzold. *Radiat. Eff. Defects Solids*, 151:215–221, (1999).

[207] E. H. Teunissen, A. P. J. Jansen, R. A. van Santen, R. Orlando, and R. Dovesi. *J. Chem. Phys.*, 101(7):5865–5874, (1994).

[208] V. Théry, D. Rinaldi, J.-L. Rivail, B. Maigret, and G. G. Ferenczy. *J. Comput. Chem.*, 15(3):269–282, (1994).

[209] L. H. Tjeng, A. R. Vos, and G. A. Sawatzky. *Surf. Sci.*, 235:269–279, (1990).

[210] K. B. Tolpygo. *Ukr. Fiz. Zh.*, 4:72, (1959).

[211] I. I. Tupizin and I. V. Abarenkov. *Phys. Status Solidi B*, 82:99, (1977).

[212] P. E. A. Turchi, A. Gonis, and L. Colombo, editors. *Tight-Binding Approach to Computational material Science*, volume 491 of *Materials Research Society Symposium Proceedings*. Materials Research Society, Warrendale, Pennsylvania, 1997.

[213] J. M. Vail. *J. Phys. Chem. Solids*, 51(7):589–607, (1990).

[214] J. M. Vail, R. Pandey, and A. B. Kunz. *Rev. Solid State Sci.*, 5:241, (1991).

[215] J. H. Van Vleck. *J. Chem. Phys.*, 3:807–813, (1935).

[216] W. R. Wadt and P. J. Hay. *J. Chem. Phys.*, 82(1):284–298, (1985).

[217] D. M. Wang and E. de Boer. *J. Chem. Phys.*, 92(8):4698–4707, (1990).

[218] D. M. Wang, S. M. Meijers, and E. de Boer. *Mol. Phys.*, 70(6):1135–1144, (1990).

[219] D. Wolf, P. Keblinski, S. R. Phillpot, and J. Eggebrecht. *J. Chem. Phys.*, 110(17):8254–8282, (1999).

[220] R. F. Wood and H. W. Joy. *Phys. Rev.*, 136:451A, (1946).

[221] A. Zecchina, M. G. Lofthouse, and F. S. Stone. *J. Chem. Soc. Faraday Trans. I*, 71:1476, (1975).